Title
Theory and design of tunable terahertz metamaterials for application to tunable terahertz quantum cascade lasers

Author
Curwen, Chris

Publication Date
2014

Peer reviewed|Thesis/dissertation

University of California

Los Angeles

Theory and Design of Tunable Terahertz Metamaterials for Application to Tunable Terahertz Quantum Cascade Lasers

A thesis submitted in partial satisfaction

of the requirements for the degree

Master of Science in Electrical Engineering

by

Christopher Curwen

2014

Abstract of the Thesis

Theory and Design of Tunable Terahertz Metamaterials for Application to Tunable Terahertz Quantum Cascade Lasers

by

Christopher Curwen

Master of Science in Electrical Engineering

University of California, Los Angeles, 2014

Professor Benjamin S. Williams, Chair

Terahertz quantum cascade lasers are compact, coherent sources of THz power that have drawn considerable attention in the past 10-15 years for their potential use in THz applications such as spectroscopy and imaging. One of the key developments required to further the usefulness THz QCLs is robust, broadband tunability. In this work, I suggest a new technique for tuning THz QCLs by incorporating MEMS fixed-fixed and fixed-free cantilever beams into a THz transmission line metamaterial resonant cavity. An analytic model for such THz transmission line metamaterials is demonstrated using transmission line theory and is supported by 2-D and 3-D finite element simulations. Proposed processes for fabricating tunable THz transmission line metamaterials are outlined and current progress on actual fabrication and device testing is reported.

The thesis of Christopher Curwen is approved.

Robert N. Candler

Mona Jarrahi

Benjamin S. Williams, Committee Chair

University of California, Los Angeles

2014

Table of Contents

List of Figures

Acknowledgments

I would like to thank my advisor, Professor Benjamin Williams, for his guidance on this project and for teaching me the fundamentals of good scientific and engineering research. I want to thank my former labmates Amir Tavallaee, Philip Hon, and Zhijun Liu for laying the foundational work for this project. Finally, I want to thank my parents for their love and support as I pursue graduate studies.

Vita

2010-2012	Undergraduate Researcher for Professor Srinivas Tadigadapa, Department of Electrical Engineering, Pennsylvania State University.
2011	Research Experience for Undergraduates Program, Department of Electrical Engineering, Atmospheric Electrodynamics Laboratory, Pennsylvania State University.
2012	B.S. in Electrical Engineering, Pennsylvania State University.
2012-present	Graduate Research Assistant, Electrical Engineering Department, UCLA.

CHAPTER 1

Introduction

The THz frequency range is often defined as 300 GHz - 10 THz (wavelengths 1 mm - 30 μm). It lies above the radio and microwave ranges and lies below the infrared and visible ranges, but the THz range has seen significantly less development than its neighbors due to unique engineering challenges in the THz. For example, at THz frequencies, most traditional electronic semiconductor devices are less effective due to limited electron transit times and increased losses from parasitic resistive and reactive elements [1]. On the other hand, small photon energies associated with the THz range (roughly 4-40 meV) make traditional optical and optoelectronic device design difficult. Additionally, THz radiation does not propagate well through atmosphere due to strong THz spectral features of a large number of gas-phase and solid-phase materials, though this does make THz a good candidate for many high-resolution spectroscopy applications compared to its neighboring frequency ranges. Furthermore, compared to the microwave range, the THz range offers higher spatial resolution in imaging and access to higher bandwidth for communications purposes, and compared to infrared and optical frequencies, the THz range offers advantages in that THz waves can still be guided and controlled by many traditional metallic and dielectric waveguide structures that are well established in the microwave and RF ranges. The challenges associated with the THz region has slowed progress in the development of THz sources, detectors, and applications, however, the potential for the THz range has continually driven a number of research efforts, many of which are summarized

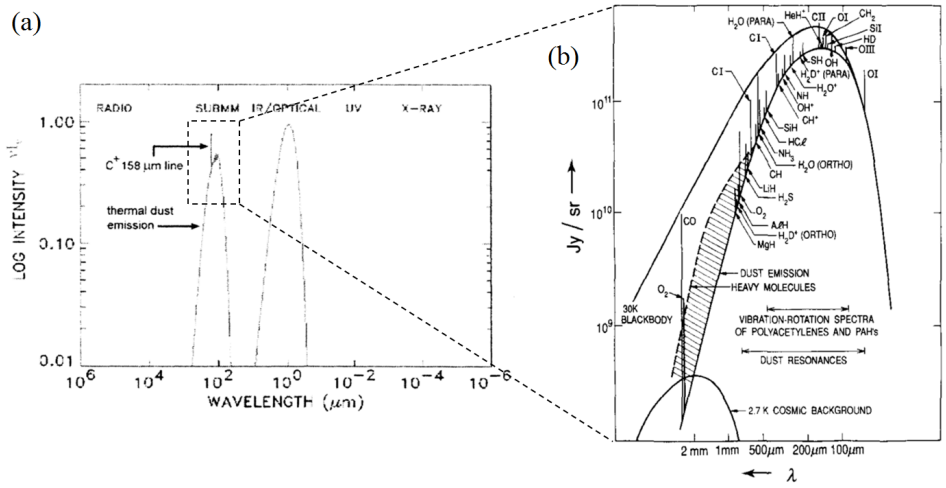

Figure 1.1: (a) Spectrum of the Milky Way taken with NASA's COBE satellite showing about half the measured luminocity in the submillimeter region and about half in the IR/optical range [12] (b) A closer look at the THz region of the spectrum compared with a 30 K blackbody and the cosmic background [7].

in review articles [1–3].

1.1 Terahertz applications

The primary application and drive for the development of THz technologies has always been and may always be high-resolution frequency-domain and time-domain spectroscopy. Many chemical species have rotational and vibrational transitions on the order of THz energies and show their strongest absorption and emission signatures in the terahertz (ex. H_2O, O_2, O_3, CO, HCl, and OH) [4]. THz spectroscopy has been demonstrated in lab based studies of gaseous species and has been implemented for plasma fusion diagnostics [5, 6], but the dominant interest and application for THz spectroscopy systems lies in atmospheric and space sciences, i.e. remote sensing using heterodyning and Fourier transform spectroscopy techniques. Measurements made by the Cosmic Background Explorer satellite

(COBE) of absolute broadband radiant energy in the universe suggests that most of this energy lies in the terahertz range and upper ends of the microwave region (see Figure 1.1) [7]. The microwave content of this measurement mostly accounts for the cosmic background radiation of a 2.7 K blackbody, while the terahertz content comes from warmer regions of interstellar space associated with processes such as star formation and galaxy evolution. THz spectroscopy offers both higher frequency and spacial resolution than microwave in these warmer regions, and THz radiation can penetrate particulate matter surrounding these regions that near-IR cannot. A set of three instruments aboard the European Space Agency's Hershel space observatory, for example, successfully collected new spectral information at wavelengths of 60-600 μm (500 GHz - 5 THz) from 2009-2013 [8]. Space-based THz observations of our own atmosphere and those of other planets and celestial bodies can also provide valuable information about their environments. Indirect observations of ozone depletion in Earth's atmosphere, for example, have been made using atmospheric limb sounding tuned to the 2.5 THz OH line [9]. Recently, some atmospheric and deep space THz observations have also been made from high altitude observatories such as the Stratospheric Terahertz Observatory (STO), a long-duration stratospheric balloon equipped for measurements at 1.46 THz and 1.9 THz [10], and SOFIA (Stratospheric Observatory for Infrared Astronomy), an observatory constructed in a Boeing 747 capable of making observations from 0.3-1600 μm [11]. Both projects are largely funded by NASA.

Ground and space based THz spectroscopy has been demonstrated using Fourier-transform interferometry, Fabry-Perot interferometry, and heterodyne mixing. In many cases, heterodyne spectroscopy is the preferred technique, which requires a stable, coherent THz local-oscillator (LO) to mix with the received signal, down-converting the THz frequency content to a lower frequency that can be amplified and sampled. Lack of compact, coherent, tunable THz sources is arguably the most significant barrier to progress in this field.

Another THz spectroscopic technique that should be mentioned is THz time-domain spectroscopy (TDS), which uses a femptosecond laser to excite and sample a THz pulse in the time domain. By passing the THz pulse through a sample and observing the change in the time dependent electric field of the pulse, important material parameters can be determined. THz-TDS has been used to study and image biomolecules, medicines, semiconductor, narcotics, cancer cells, and more [13, 14]. Early THz-TDS systems required large optical setups and typically large Ti-Sapphire lasers, but with the development of femptosecond fiber lasers, benchtop and even hand-held THz-TDS systems for imaging and spectroscopy are now available [**?**, 16, 17]. Imaging in the THz domain is appealing because THz wavelengths can provide good resolution, and many materials such as clothing and packaging are transparent in the THz, presenting potential advantages in non-invasive inspection and security applications. THz-TDS has fueled much of the recent activity in THz imaging, but femptosecond sources typically deliver low THz power, greatly limiting the penetration depth and scan speeds of such systems. The recent development of higher power continuous wave (CW) THz sources such as THz quantum cascade lasers has led to several examples of nearly real-time, CW THz imaging [18, 19].

Development of THz information and communications technologies has been limited due to severe atmospheric absorption of terahertz radiation, but the draw of large bandwidth and high speeds is appealing enough to stir-up some talk of short distance, secure THz communications and secure inter-satellite communications [20].

1.2 Terahertz sources

As suggested in section 1.1, there is a general deficiency in THz sources to meet the demands that THz applications require. An ideal THz source should be com-

pact, coherent, operate at room-temperature, and provide sufficient power and tunability for the desired application. A number of techniques for THz generation are in development, both optical and electronics based, but none meet all of the desired requirements. Figure 1.2 (taken from [3]) gives a summary of THz sources.

Upconverting microwave signals to THz signals using GaAs Schottky diode frequency multipliers may be the most relied upon method for generating narrow band, continuous-wave sub-millimeter and THz radiation below 3 THz. These frequency multipliers use the reactive and resistive nonlinearities of Schottky diodes to distort incoming GHz signals and generate higher harmonics in the THz. NASA's Jet Propulsion Laboratory, for example, has demonstrated GaAs Schottky diode multipliers ranging from 300 GHz to 2.5 THz with CW powers from thousands of microwatts for the former, down to <10 microwatts by the latter [21]. GaAs frequency multipliers seem to be the preferred choice for THz heterodyne spectroscopy and will likely maintain this status in the near future as potential competitors still have several performance and reliability issues to overcome before they are robust enough for space applications.

Coming from the optics end, one of the simplest techniques for generating THz radiation is by generating THz frequency photocurrents in a photomixer. Photomixers are materials with extremely short carrier lifetimes, such as low-temperature grown (LTG) GaAs, whose photoconductivity can be modulated at high frequencies. CW THz radiation can be provided from photomixers driven by the beat frequency of two mixed lasers signals. Photomixers are relatively simple to make and tune, but they typically produce low THz powers. Recently demonstrated ErAs:InGaAs photomixers using plasmonic contacts, for example, are tunable from 0.25-2 THz and output tens to hundreds of microwatts of power (larger power at lower frequencies) [22]. Similar to the photomixing technique, pulses of THz radiation can be produced by a photoconductive switch (also commonly made of LTG GaAs) excited by a femtosecond laser. The frequency of the

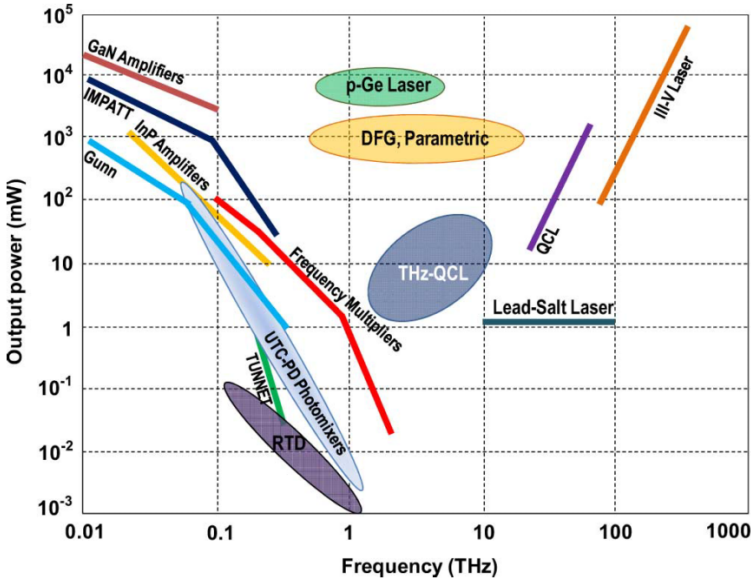

Figure 1.2: Overview of THz sources as a function of frequency and power. Electronics based CW sources are shown to roll-off in power coming from lower frequencies. At higher frequencies, THz QCLs, gas lasers, p-Ge lasers, and nonlinear optics techniques provide THz power at a variety of levels in pulsed and CW modes, they are rarely as compact or convenient as electronic sources. Figure taken from [3]

radiation produced depends on the length of the pulse. This method is particularly important for its use in THz-TDS, but the broadband, pulsed nature of photoconductive switches make them unsuitable for applications requiring a THz local oscillator.

Other optics based approaches to the generation of THz radiation use nonlinear effects such as difference frequency generation (DFG), optical rectification, and optical parametric oscillation (OPO). For example, DFG in a GaSe crystal has produced THz radiation from 0.18-5.27 THz with peak output powers from 5 ns pulses (pulsed at 10 Hz) reaching 69.4 W at 1.53 THz [23]. THz OPO systems typically use $LiNbO_3$ as a nonlinear material but have not demonstrated as much

output power or tunability as DFG techniques [24]. Both techniques operate at room temperature and offer widely tunable, watt levels of peak power, but they require large lasers and optical setups and do not produce CW power. Another recent DFG approach to THz generation that looks promising uses two different frequency mid-IR QCL devices that have been grown on top of each other. The nonlinear material is the QCL active region itself, so the entire generation scheme is contained to a room-temperature, QCL sized device that can produce a few microwatts of CW THz power and peak pulsed THz powers greater than a milliwatt [25, 26]. An external cavity diffraction grating has been used to demonstrate tuning of a pulsed mid-IR DFG source from 1.2-5.9 THz with peak powers just under 100 μW [27].

A more recent technology that has emerged is the THz QCL, which will be the focus of this work. The THz QCL is an all semiconductor based THz laser that produces THz photons using intersubband transitions in quantum wells. The first THz QCL devices were demonstrated in 2001, produced a few milliwatts of peak pulsed power in the range of 3-5 THz, and operated up to about 50 K [28–30]. Today, THz QCL devices have produced CW powers up to 138 mW at 4.4 THz [31] and pulsed output powers greater than 1 W [32]. The maximum temperature reported for CW THz QCL operation in now 129 K at about 3 THz [33], and pulsed operation has reached 200 K around 3.22 THz [34]. Demonstrated THz QCL devices have covered frequencies from 0.84 THz to 5 THz, but typically operate best above 2 THz. Subwavelength dimensions of QCL resonators make outcoupling of usable radiation difficult, however use of distributed feedback designs and THz metamaterial antenna structures has enabled improvements in beam pattern and outcoupling strength [35, 36]. Cryogenic temperatures are required for THz QCL operation because THz photon energies are comparable in strength to longitudinal-optical (LO) phonon energies in semiconductors, allowing phonon scattering to dominate radiative scattering of electrons at higher temperatures.

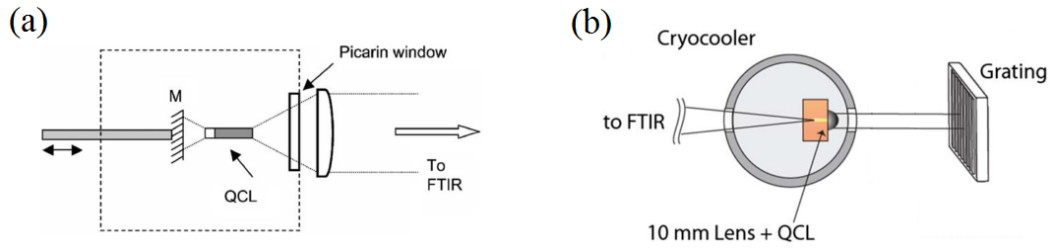

Figure 1.3: External cavity tunable THz QCL designs using (a) a movable mirror [42] and (b) a diffraction grating [43].

This is likely the largest drawback of THz QCL technology as cryogenic temperatures are typically achieved using large, unwieldy dewars cooled using liquid nitrogen or liquid helium. It should be noted, however, that advancements in cryogen-free cryocoolers, such as Stirling engine coolers, now allow for temperatures as low as 77 K in tabletop setups weighing under a kilogram and consuming $<$5 W of power, offering greatly increased flexibility in low temperature operation [37]. Achieving room temperature operation is the preferred solution and continues to be one of the major challenges for this technology. One approach to solving the phonon scattering problem is to look towards lower dimensional devices such as nanowires and quantum dots, where increased confinement of electron wavefuctions prevents interaction with LO-phonon energies [38]. Despite the challenges associated with THz QCL devices, they have been successfully demonstrated as local oscillators in THz heterodyne spectroscopy systems and as THz sources for imaging systems [39–41].

In order to further improve the usefulness of THz QCLs in heterodyne and imaging applications, broadband tunability must be available. Several sources document efforts to provide tunability to THz QCLs, but most require inconvenient external cavity configurations and/or show mode hoping rather than continuous tuning. Examples of an external cavity (EC) THz QCL devices include a simple movable mirror setup that demonstrated 90 GHz of rough tuning and

12 GHz of continuous tuning around 4.8 THz [42], and a Littrow cavity setup that used a diffraction grating to provide 165 GHz of discontinuous tuning and 9 GHz of continuous tuning around 4.4 THz [43]. These configurations are shown in Figure 1.3. EC tuning of THz QCLs is challenging due to large mode mismatch and poor outcoupling from the facets of THz QCL devices, making it difficult to strongly couple to an EC. THz EC QCL examples only show discontinuous fractional tuning ($\frac{\Delta\nu}{\nu_0}$) ratios of <3% compared to >10% continuous tuning ratios demonstrated from similar EC cavities with IR QCLs [44]. The current standard for tuning a THz QCL is set at ≈330 GHz of continuous mode tuning around 3.85 THz, which was reported using a MEMS dielectric structure to tune the transverse wavenumber of the mode [46]. This an impressive ≈8.5% tuning range that is limited by the upper limit of the gain bandwidth of the laser rather than the tuning mechanism, but the design is challenging to fabricate and requires very precise alignment of a separately fabricated MEMS flexure to the laser waveguide. This thesis will deal with the design and development of a new MEMS based tunable THz QCL using a tunable THz metamaterial waveguide. The proposed design has the potential for new levels of fractional tuning and does not require an external cavity. Furthermore, the proposed structures are fully monolithic and suitable for various integrated tuning and modulation schemes.

Other noteworthy sources of THz radiation labeled in Figure 1.2 that have not been mentioned include vacuum electronic sources (i.e. traveling wave tubes, klystrons, free electron lasers, etc.), p-type Germanium lasers, CO_2 laser pumped molecular gas lasers, and electronic oscillators and amplifiers including Gunn and IMPATT oscillators, GaN amplifiers, InP amplifiers, etc. These sources have provided important demonstrations of THz generation, but have not seen as much active research lately for varied reasons [1]. A CO_2 laser pumped molecular gas far-infrared laser, for example, has been incorporated as part of NASA's Earth Observing System-Microwave Limb Sounder (EOS-MLS) satellite experiment de-

spite being large and heavy [48].

1.3 Terahertz quantum cascade lasers

THz QCLs, like any laser, require a gain medium and a resonant cavity. The gain medium provides photonic gain to an electromagnetic mode supported by the resonant cavity, while the cavity itself adds loss to the mode via outcoupling of radiation and material free carrier losses. In order for the system to lase, the threshold condition on the mode is:

$$\Gamma_{mod} g_{QCL} = \alpha_{mod} \tag{1.1}$$

where g_{QCL} (cm^{-1}) is the bulk material gain coefficient provided by the heterostructure, Γ_{mod} is the confinement factor of the mode in question, and α_{mod} is the round-trip average loss coefficient per unit length of the mode in question. The confinement factor:

$$\Gamma_{mod} = \frac{n_g \int\int_{actv} \epsilon_{actv} \left|\vec{E_y}\right|^2 dxdy}{n \int\int_{\infty} \epsilon \left|\vec{E}\right|^2 dxdy} \tag{1.2}$$

describes the percentage of the mode that is confined to the active region and electric field polarized normal to the quantum well growth. In the numerator, n_g denotes the group index of refraction, ϵ_{actv} is the permitivity of the active region, $\vec{E_y}$ is the component of the E-field normal to the quantum well growth, and the surface integral is over the active region where gain occurs. In the denominator, the integral is over the entire mode and the appropriate n and ϵ should be applied in each region of space. In order to reach lasing threshold, it is important to have as much gain (g_{QCL}) as possible from the active region and to have a resonant cavity with high modal confinement and low losses. For detailed reviews of THz QCL theory and design, see [49, 51].

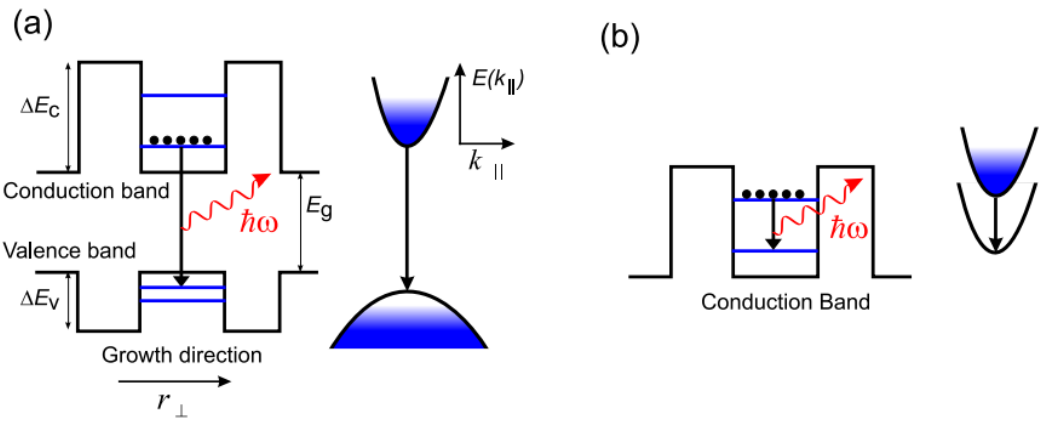

Figure 1.4: Comparison between (a) interband radiative transitions and (b) intersubband radiative transitions. Figure taken from [51]

1.3.1 Optical gain from QCL heterostructures

Traditional bipolar semiconductor lasers use radiative transitions across semiconductor bandgaps to generate photonic gain. Typical semiconductor bandgaps, however, are in the range of hundreds to thousands of meV, making them unsuitable for THz applications, which require energy separations of tens of meV. Instead, heterostructure quantum wells are used to quantize electron energies in the semiconductor growth direction while parabolic free carrier dispersions still apply to the in-plane directions. This breaks the conduction band into subbands and THz photonic gain comes from intersubband transitions that take place entirely in the conduction band. Because the in-plane dispersions are identical, the joint density of states for the transition is a delta function at the energy of the optical transition, which can be tuned with proper selection of the well width. These differences between interband and intersubband transitions are illustrated in Figure 1.4.

THz QCLs are typically made using GaAs/$Al_xGa_{1-x}As$ material systems, though there have also been demonstrations in InGaAs/InAlAs, and InGaAs/GaAsSb

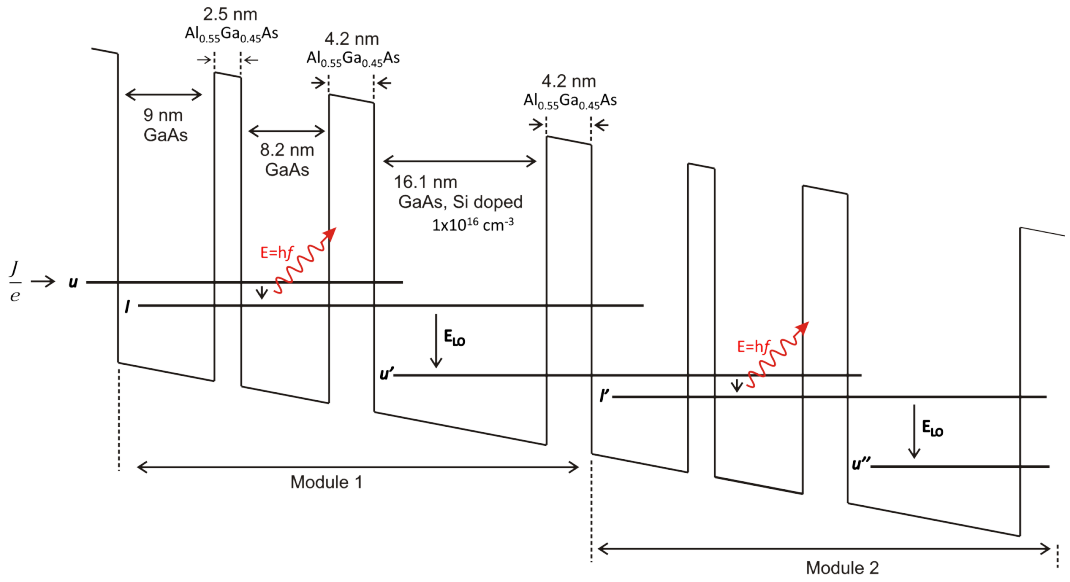

Figure 1.5: Electron transport through a biased 3-well QCL module repeated twice. The suggested scheme uses LO-phonon scattering to depopulate lower states l and l' to upper states u' and u''.

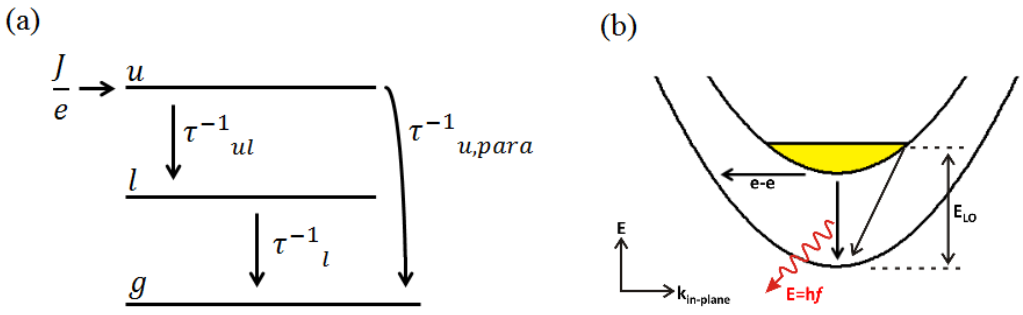

Figure 1.6: (a)General 3-level laser scheme. (b)Intersubbandband scattering mechanisms in QCLs including radiative scattering at the Γ-point, LO-phonon scattering from higher in the conduction band, and elastic electron-electron scattering.

systems [52,53]. Figure 1.5 shows a typical bandstructure diagram for a resonant-phonon depopulation design. The design consists of a three well module that would be repeated tens or hundreds of times (though only two modules are shown here). When the modules are properly biased, the subbands in the wells line up to allow electron transport via an upper radiative state u and a lower radiative state l that depopulates to the upper radiative state of the neighboring module u'.

1.3.1.1 3-level QCL laser model

Many QCL designs can be modeled by a basic 3-level laser system as shown in Figure 1.6(a). The upper level 3 is pumped by current $\frac{J}{e}$. Electrons in level 3 can either scatter to level 2 at a rate τ_{32}^{-1} by emission of a photon, or scatter parasitically out to another state at a rate $\tau_{3,para}^{-1}$, giving the total rate of depopulation of level 3 to be $\tau_3^{-1} = \tau_{32}^{-1} + \tau_{3,para}^{-1}$. Electrons collected in level 2 will depopulate to a ground level at a rate τ_2^{-1}. Writing rate equations for this system and solving for steady state conditions gives us the following expression for population inversion:

$$\Delta N = \frac{J}{e}\tau_3(1 - \frac{\tau_2}{\tau_{32}}) \tag{1.3}$$

As should be intuitive, equation (1.3) says that to obtain a large population inversion, we need to maximize τ_{32} with respect to τ_2 while minimizing $\tau_{3,para}$. Radiative scattering rates in a QCL can be determined using Fermi's golden rule, while non-radiative scattering rates are a result of longitudinal-optical (LO) phonon scattering, electron-electron scattering, and electron impurity scattering. While outside of the scope of this thesis, successful QCL design requires a detailed knowledge of these scattering mechanisms to influence the rates of each transition. The modules in Figure 1.4, for example, tune the $l \rightarrow u'$ transitions to the LO-phonon resonance, encouraging quick depopulation of the l states while the $u \rightarrow l$

transition is below the minimum quantization of LO-phonons and so can scatter radiatively with a much longer time constant. Intersubband scattering processes are illustrated in 2-dimensional k-space in Figure 1.6(b).

The gain available from the radiative $u \rightarrow l$ transition is described by:

$$g(\nu_0) \propto \frac{\Delta N f}{\Delta \nu} \tag{1.4}$$

where $\Delta\nu$ is the linewidth of the transition, and f is the oscillator strength of the transition, which is primarily an overlap integral of states u and l. The oscillator strength can be increased by increasing the overlap and symmetry of states u and l, but this is often accompanied by an increase in non-radiative scattering out of state u, decreasing population inversion. Optimization of QCL design often involves trade-offs between oscillator strength and population inversion.

1.3.2 Waveguide

In order to provide feedback and oscillation for lasing, QCL active region heterostructures are processed into so-called metal-metal (MM) waveguide resonant cavities. The basic MM waveguide structure is shown in Figure 1.7(a). It consists of a rectangular slab of QCL gain material sandwiched between an infinite ground plane and a top metal contact. The waveguide is made into a resonator simply by cleaving facets at the ends of the waveguide. In order for the active region to provide gain to modes in the resonator, the modes must be electric field polarized normal to the quantum well growth, so only TM modes need be considered. Furthermore, only TM_{0X} modes need be considered because higher order modes normal to the quantum wells are forbidden by the subwavelength confinement. Normalized E-field mode profiles for the lower order TM_{00} and TM_{01} modes are shown in Figure 1.7(b). THz QCLs made by the author are typically 50-100μm in width and THz wavelengths in a GaAs/AlGaAs system are on the order of 30-40

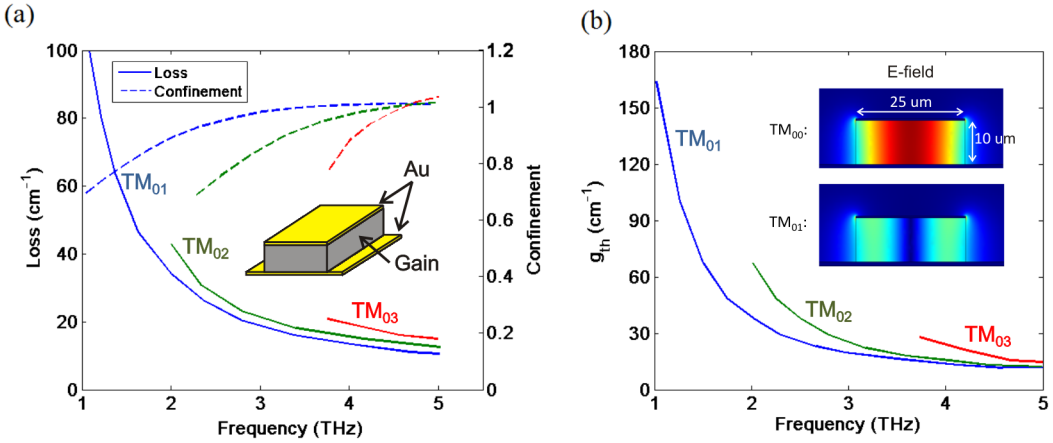

Figure 1.7: (a) Loss and confinement of the first three modes of a 25 μm wide, 5 μm thick metal-metal waveguide. (b) Threshold gain values for the three modes and cross-section electric field profiles.

μm, so lasing typically occurs in these lower order TM modes. To evaluate the performance of MM waveguides as THz QCL resonators, we must consider the mode loss α_{mod} and confinement Γ_{mod}, as noted from equation 1.1.

The loss parameter α_{mod} is a combined result of radiative outcoupling through the cleaved facets and free carrier losses in the material. Due to the subwavelength confinement of THz MM waveguides, MM waveguide facets have large reflectivities (>0.7) and outcoupling of radiation is usually weak [54]. Material free carrier losses are estimated using the Drude model. The Drude model treats conduction electrons in a metal or semiconductor as free particles that obey Newton's laws of motion when subjected to an electric field, but experience momentum relaxation scattering events with time constant τ [55]. Using the time dependent equation of motion for these electrons in an AC electric field, the AC conductivity for a metal or semiconductor is given by:

$$\sigma(\omega) = \frac{ne^2\tau}{m^*(1 - j\omega\tau)}) \tag{1.5}$$

where n is the free carrier density and m^* is the effective mass of the free carriers. Using Maxwell's equations to write permitivity in terms of conductivity, we can write the complex permitivity as predicted by the Drude model to be:

$$\epsilon(\omega) = \epsilon_r\epsilon_o - j\frac{\sigma(\omega)}{\omega} = \frac{\epsilon'(\omega) - j\epsilon''(\omega)}{\epsilon_o} \tag{1.6}$$

$$= \epsilon_o\left(\epsilon_r - \frac{\omega_p^2\tau^2}{1+\omega^2\tau^2} - j\frac{\omega_p^2\tau}{\omega(1+\omega^2\tau^2)}\right) \tag{1.7}$$

where $\omega_p = \frac{ne^2}{m^*\epsilon_o}$ is the plasma frequency of the material. The Drude losses, confinement factor, and threshold gain for the first three TM modes a 5 μm thick MM waveguide is plotted in Figure 1.7. Drude parameters for Au are given by: $N_{Au} = 5.9 \times 10^{28}$ cm^{-3}, $\tau_{Au} = 0.039$ ps, $m^*_{Au} = 1$; and Drude parameters for the heterostructure are modeled uniformly doped GaAs: $N_{GaAs} = 5 \times 10^{21}$ cm^{-3}, $\tau_{GaAs} = 0.5$ ps, m^*_{GaAs}=0.067.

1.4 Metamaterials

Metamaterials are a class of engineered electromagnetic structures that effectively behave as homogeneous materials with designed electromagnetic properties; i.e. metamaterials exhibit engineered permittivity and permeability. Metamaterials, similar to atoms organized in natural materials, are periodic electrical structures with periodicity that is small enough compared to the wavelength in question that refractive effects on the wave dominate over scattering or diffractive effects (typically $p < \frac{\lambda_g}{4}$, where p is the period of the metamaterial structure and λ_g is the guided wavelength in the structure). Designing metamaterials that demonstrate simultaneously negative ϵ and μ has been one of the primary goal of metamaterial research [56, 57].

Observing Maxwell's equations for time harmonic waves in a source free medium, we have the following relationship between electric field $\vec{E}$, magnetic field $\vec{H}$, and

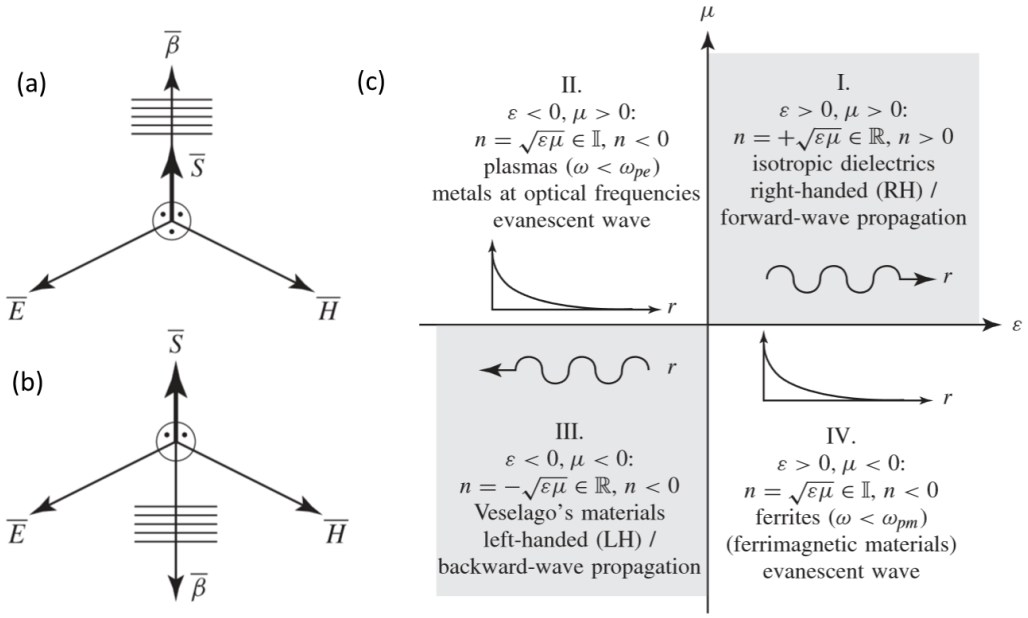

Figure 1.8: Vector relationships for (a) right handed wave propagation and (b)left handed wave propagation. (c) Propagation characteristics and refractive index of materials with positive and negative ϵ and/or μ. Quadrants II and IV only allow evanescent wave propagation while quadrants I and III allow wave propagation but have opposite phase velocity directions.

propagation constant $\vec{\beta}$:

$$\vec{\beta} \times \vec{E} = \omega\mu\vec{H} \tag{1.8}$$

$$\vec{\beta} \times \vec{H} = -\omega\epsilon\vec{E} \tag{1.9}$$

If a material has positive ϵ and μ, we have the commonly recognized right hand (RH) triad relating these three components of the wave. If we have a material with simultaneously negative ϵ and μ, the relationship between $\vec{E}$, $\vec{H}$, and $\vec{\beta}$ is described by a left handed (LH) triad where phase and group velocities are antiparallel (noting from Poynting's theorem that group velocity is always in the positive direction, or away from the source), see Figure 1.8. The possible physical effects of a negative ϵ and μ material were first proposed by Russian physicist

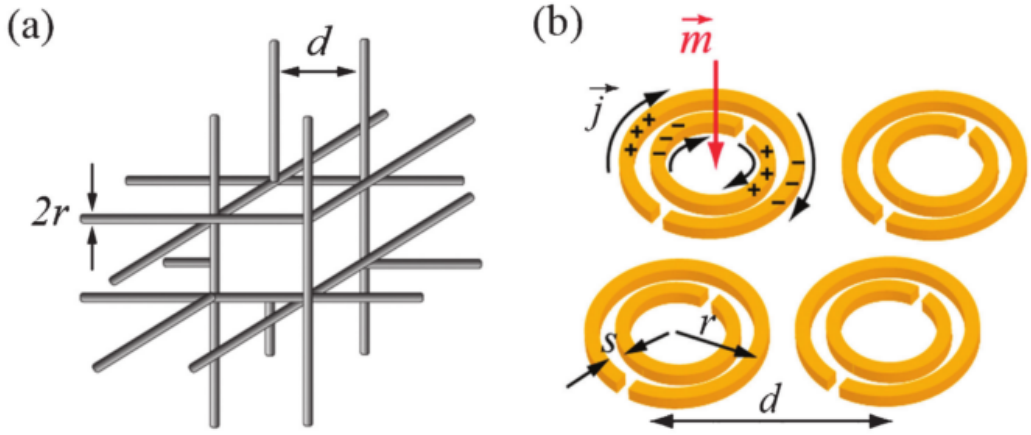

Figure 1.9: Illustrations taken from [57] of (a) a TW structure used as electric dipoles and (b) SRR structures used as magnetic dipoles.

Victor Veselago in 1967 [58]. Veselago theorized properties for a naturally occurring, homogeneous negative ϵ and μ material. These properties included negative refraction, reversal of the Doppler effect, reversal of Vavilov-$\ddot{C}$erenkov radiation, along with others. Naturally occurring materials with simultaneously negative ϵ and μ materials are not known to exist, but today many such properties are being effectively realized in metamaterials.

The first experimental demonstrations of metamaterials with simultaneously negative ϵ and μ came in 2000 from Smith, *et al.* [59, 60]. These first demonstration were based on periodic resonant structures such as metal split-ring resonators (SRR) and thin metal wire (TW) grids (see Figure 1.9). These structures act as electric and magnetic dipoles distributed at subwavelength periodicity, influencing the effective ϵ and μ seen by waves similar to the way naturally occurring ϵ and μ parameters can be described as the collective effect of charge oscillations in a material. The effective permittivity and permeability of SRR and TW structures have been determined to reflect the drude model with plasma frequency and scattering times that are dependent on the density and mobility of carriers in the

metamaterial structure [61, 62]. While SRR and TW based metamaterials seem to dominate metamaterial research efforts, the practicality of these structures are often under skepticism because the resonant nature of the designs results in narrowband performance and high material losses. The first SRR and TW structures were demonstrated in the microwave range, around 1-10 GHz, but as we move to higher frequencies, especially optical frequencies, material losses become worse and it becomes difficult to scale dimensions of the metamaterial structure in accordance with the decreasing wavelengths. Metamaterials using metal SRR and other nanoscale metallic configurations have been demonstrated up to THz and IR frequencies [63, 64]. These higher frequency metamaterials are typically two-dimensional and can be fabricated using photolithography techniques. 2-D metamaterials and metasurfaces show unique transmission and reflection characteristics, in the operating frequency range. The structural nature and decreasing dimensions of higher frequency metamaterials has drawn attention to the idea of tuning, switching, and modulating metamaterial properties using MEMS [66, 67]. In the THz, for example, tunable michromachined platforms have been used to adjust the spacing between planar SRR patterns, tuning a notch in the transmission from frequencies of ≈4-5.5 THz [68]. In another recent study, a switchable THz metasurface described by transmission line theory (nonresonant, see following paragraph) was demonstrated by incorporating switchable Au MEMS structures. By pulling in the MEMS membranes, the surface impedance switches, allowing for broadband phase modulation of reflected and transmitted waves below ≈1.5 THz [69] (see Figure 1.10(b)). Broadband phase and amplitude modulation of planar THz metamaterials has also been studied by tuning carrier concentrations in the substrate material [70, 71].

An alternative, non-resonant approach to THz metamaterials uses transmission line metamaterial techniques that were originally demonstrated in the microwave regime using microstrip waveguides [74–76]. THz metal-metal waveg-

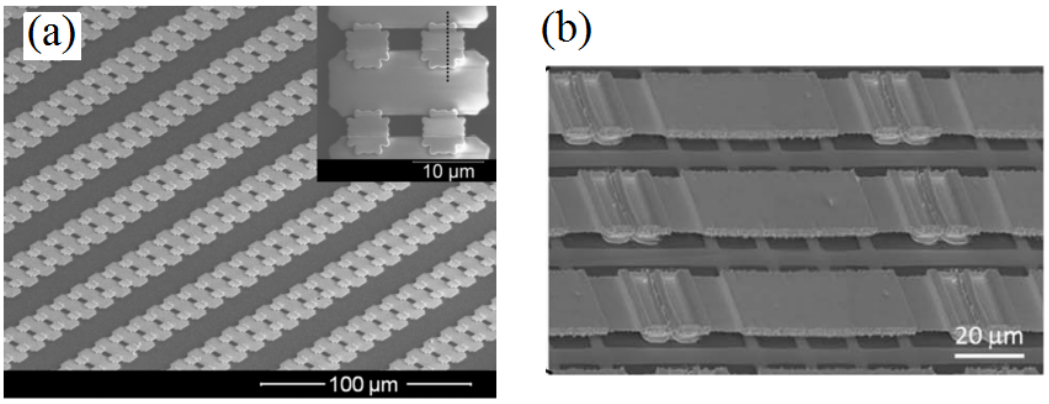

Figure 1.10: SEM images of (a) THz metal-metal waveguides based metamaterial showing both RH and LH wave propagation [82], and (b) MEMS based switchable scattering metasurface [69].

uides, similar in structure to microstrip waveguides (see section 1.3 and chapter 2) have been used to demonstrate active THz transmission line metamaterials with RH propagation above ≈2.6 THz and LH propagation below (see Figure 1.10(a)) [80, 81]. Broadband dispersions characteristics of these THz metamaterials have been shown to tune with the specific transmission line parameters [82]. The purpose of this thesis is to propose a new tuning mechanism for THz QCLs using metal-metal waveguide based THz transmission line metamaterials that have tunable MEMS elements.

CHAPTER 2

Tunable terahertz metamaterial QCL theory and design

2.1 Introduction

Broadband single-mode tunability is one of the key features needed to further the development of THz QCL applications. Tuning of a laser can typically be accomplished by either tuning the refractive index of the resonant cavity medium, or mechanically tuning the resonant cavity geometry. In semiconductor lasers, refractive index tuning can be achieved by varying the temperature of the device or current through the device, but both techniques are typically limited to <1% tuning [83, 84]. THz QCLs have shown temperature tuning up to 19.7 GHz around 2.92 THz (<1% tuning) using a surface emitting DFB design [85] and a peak electrical tuning up to 30 GHz around 3.5 THz (still <1% tuning) has been demonstrated using the cavity pulling of a photonic crystal resonant cavity [86]. As an alternative, external cavity (EC) setups that are mechanically tuned to provide selective feedback to the laser can provide more broadband tunability. EC semiconductor lasers are almost exclusively based on the use of a diffraction grating to tune the frequency feedback by adjusting the angle of the diffraction grating (see Figure 1.3(b)). Diffraction grating EC lasers have demonstrated broadband, continuous mode tuning of semiconductor lasers in the infrared and optical regimes [44, 87]. EC tuning of mid-IR QCL devices has shown up to ≈30% continuous tuning, but EC tuning of THz QCL devices has been more diffi-

cult because the large reflectivity of THz QCL facets makes it difficult to strongly couple to the grating feedback. As mentioned in chapter 1, EC grating implementations with THz QCLs have only shown up to ≈4% discontinuous tuning and <1% continuous tuning using a silicon hyperhemispherical lens to decrease the reflectivity of the coupled facet [43]. Some research efforts are now looking to less traditional tuning techniques. The most successful tuning of a THz QCL was reported using a large MEMS plunger to distort the mode profile of a THz "wire" QCL (only 10-15 μm ridge width) [45]. Using a micrometer to move the MEMS plunger, Qin *et al.* achieved 330 GHz of continuous, single-mode tuning around 3.85 THz (8.6%) [46], and using an electronically controlled version of the MEMS structure, Han *et al.* demonstrated 240 GHz of tuning around the same frequency [47]. In this chapter, I will present an alternative THz QCL tuning mechanism based on a tunable THz transmission line metamaterial.

2.2 Transmission line metamaterial theory

Many TEM and quasi-TEM transmission lines can be analyzed by replacing the physical structure of the transmission line by an equivalent circuit model. For example, many common right-handed transmission lines such as coax cables, stripline, microstrip, and two-wire lines can be modeled by the equivalent circuit in Figure 2.1(a). It consists of an infinite cascade of unit cells, each containing a lumped series inductance per unit length L'_R (H/m) and a lumped shunt capacitance per unit length C'_R (F/m). Applying Kirchhoff's voltage and current laws to a single unit cell, we can write the lossless Telegrapher's equations:

$$-\frac{d\tilde{V}(z)}{dz} = j\omega L'_R \tilde{I}(z) \tag{2.1}$$

$$-\frac{d\tilde{I}(z)}{dz} = j\omega C'_R \tilde{V}(z) \tag{2.2}$$

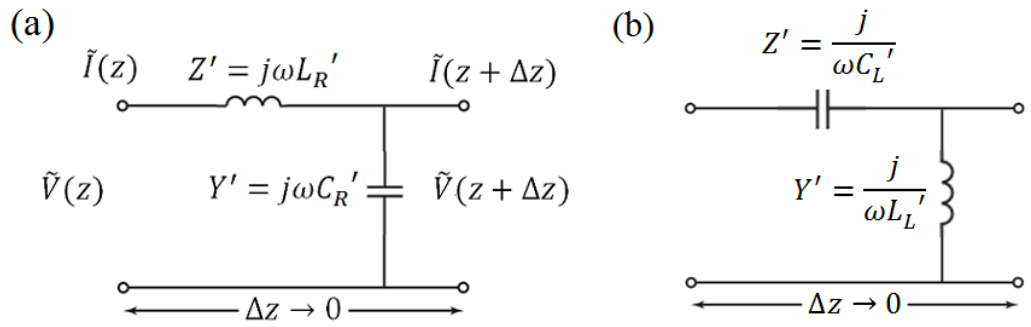

Figure 2.1: Lumped element circuit diagrams for (a) a lossless, purely right-handed transmission line, and (b) a lossless, purely left-handed transmission line.

which are two first order coupled equations that can be used to write current and voltage wave equations:

$$\frac{d^2\tilde{V}(z)}{dz^2} - \gamma^2\tilde{V}(z) = 0 \tag{2.3}$$

$$\frac{d^2\tilde{I}(z)}{dz^2} - \gamma^2\tilde{I}(z) = 0 \tag{2.4}$$

with solutions:

$$\tilde{V}(z) = V_0^+ e^{-\gamma z} + V_0^{\gamma z} \tag{2.5}$$

$$\tilde{I}(z) = I_0^+ e^{-\gamma z} + I_0^{\gamma z} \tag{2.6}$$

where the propagation constant γ is given by:

$$\gamma = \alpha + j\beta = \sqrt{(j\omega L'_R)(j\omega C'_R)} = j\omega\sqrt{L'_R C'_R} \tag{2.7}$$

The general form of the wave's propagation constant includes an attenuation coefficient α (cm^{-1}) in the real part, and wavenumber β (rad/m) in the imaginary part. In the lossless example, α is zero and β is a positive imaginary number at

all frequencies, describing typical RH wave propagation. The specific slope of γ is determined by the values of the lumped components, L'_R and C'_R.

The transmission line metamaterial concept is based on the theory that if sub-wavelength periodic electric elements (i.e. capacitors and/or inductors) with a period $p < \lambda_g/4$ are added to a transmission line, then the dispersion characteristics of the transmission line can be determined and engineered by treating the added components as lumped elements in the unit cell of the transmission line model. Much of this theory is developed and demonstrated in Caloz *et al*. [90].

2.2.1 Left-hand waves and CRLH structures

If we were to imagine a transmission line with a series capacitance times unit length C'_L (Fm) and a shunt inductance times unit length L'_L (Hm), as shown in Figure 2.1(b), and performed the same circuit analysis on this unit cell as done above, we find the propagation constant of guided waves is given by:

$$\gamma = \sqrt{Z'Y'} = -j\frac{1}{\omega\sqrt{L'_L C'_L}} \tag{2.8}$$

which describes a phase velocity that is opposite to group velocity $v_g = \frac{\partial\omega}{\partial\beta}$ (gives the velocity of energy propagation in the material).

A purely left-handed transmission line is not physically realizable because right-handed components are inherent to any physical structure being used as the transmission line. However, combinations of right-handed and left-handed transmission line lumped elements can be used to create composite right/left-handed (CRLH) transmission lines that have both RH and LH propagation constants depending on the frequency of operation. A generalized CRLH transmission line model is shown in Figure 2.2(a). In microwave engineering, a common implementation of such a CRLH transmission line is a microstrip line loaded with periodic capcitive gaps in the conductors and periodic inductive current paths to virtual

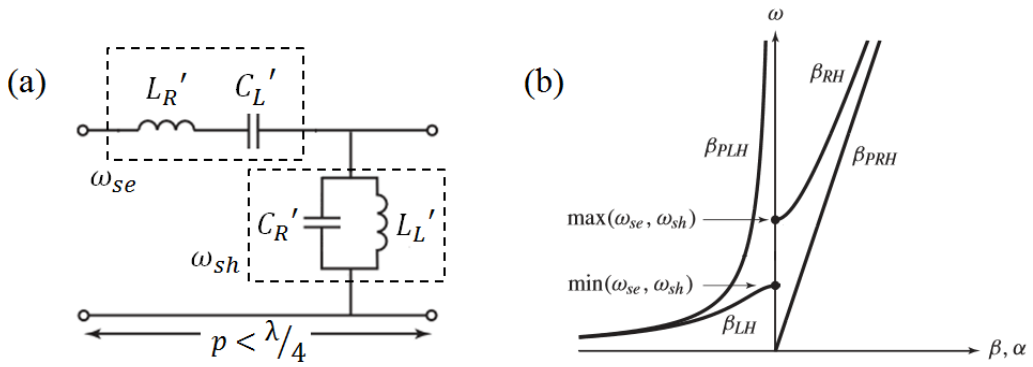

Figure 2.2: (a) CRLH generalized transmission line unit cell and (b) combined plot showing CRLH dispersion, purely right-handed dispersion, and purely left-handed dispersions. Figure (b) from [90].

grounds [90], [92].

Figure 2.2 offers a comparison between typical dispersion curves of a purely right handed transmission line (PRH), a purely left handed transmission line (PLH), and a CRLH transmission line. It should be observed that the RH and LH branches of the CRLH dispersion are separated by a stopband. Cutoff frequencies are defined by resonances in the series circuit $\omega_{se} = (C_L' L_R')^{-1/2}$ and shunt circuits $\omega_{sh} = (C_R' L_L')^{-1/2}$ of the CRLH structure. Inside of the stopband, γ is purely real so there is no wave propagation. If the transmission line is designed such that $\omega_{se} = \omega_{sh}$, then the line is said to be balanced and there is no stop band. In a balanced design, there is a smooth transition between the RH and LH branches and the group velocity is non-zero at $\beta = 0$. In sections 2.3-2.5, I will discuss a RH only THz transmission line metamaterial with an added series capacitance. There is no added shunt inductance, so this structure will not support any LH wave propagation. In section 2.6, a tunable THz CRLH design with LH capacitors and inductors is presented.

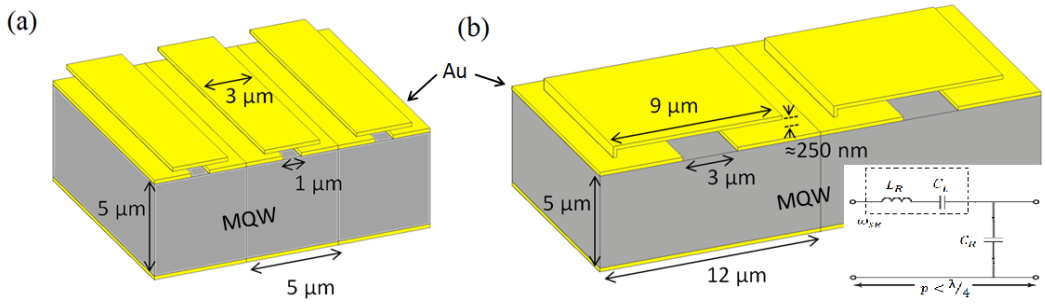

Figure 2.3: Tunable THz metamaterial designs using (a)separately biased MEMS structures and (b)self-actuated cantilevers.

2.3 Tunable THz metamaterial

One candidate for THz metamaterial transmission lines is the THz metal-metal waveguide described in Chapter 1, which is the preferred choice for many THz QCL resonators. THz metal-metal waveguides are very similar in design to microstrip transmission lines, which have provided the bases for successful work in microwave metamaterial transmission line engineering [77–79]. As done with microstrip lines, LH capacitive elements can be added by introducing discontinuities in the top metalization of the waveguide. By actuating the cantilever, the LH capacitance of the metamterial can be tuned, tuning the dispersion of the transmission line. Proposed unit cells of this structure are depicted in Figure 2.3. The free-standing overlays in 2.3(a) would presumably take the form of fixed-fixed MEMS bridge structures fabricated around the waveguide ridge that can be biased by separate electrodes that are not shown (see Chapter 3). The fixed-free cantilever structures in Figure 2.3(b), on the other hand, are self-actuated by the power in the waveguide mode (see Section 2.5).

The transmission line model for the structures in Figure 2.3 is given in the inset of the figure. This model applies assuming the TM_{00} mode is propagating (no phase variation in the z-direction). The dispersion is given by:

$$\beta^2 = \frac{L_R C_R}{p^2}(\omega^2 - \omega_{se}^2) \tag{2.9}$$

where $\omega_{se} = (C_L L_R)^{-1/2}$ is the series cutoff frequency. Note that because we're now describing a physical metamaterial unit cell, we no longer have a truly homogeneous distribution of lumped elements L'_R, C'_R, and C'_L, but rather we can define absolute L_R, C_R, and C_L values for a unit cell and divide by the period to determine average per-unit-length values. Lumped elements C_R and L_R can be approximated using parallel plate expressions: $C_R \approx \epsilon_0 \epsilon_r wp/d$, $L_R \approx \mu_0 \mu_r dp/w$, where w is the width of the unit cell, d is the thickness of the active region, and ϵ_r and μ_r are the relative permitivity and permeability of the material in the waveguide (GaAs/AlGaAs≈ 3.6). A first estimate of C_L can be made by $C_L \approx \epsilon_0 wl/h$, where l is the length of the overlap between the cantilever and the ground plane, and h is the height of the cantilever. Using the series cutoff observed in the simulation, a more precise effective LH capacitance can be determined ($C_L = 1/\omega_{se}^2 L_R$) and the equivalent transmission line model dispersion can determined (assuming parallel plate estimations for L_R and C_R). Actual values of C_L extracted from simulations are around a factor of two larger than the parallel plate estimate, suggesting C_L is not strongly confined to the cantilever gap.

2.3.1 Finite element simulations

2-D finite element simulations of the proposed structure were carried out using COMSOL Multiphysics. The simulation space and resulting field profiles are illustrated in Figure 2.4. An infinite cascade of unit cells is effectively modeled by applying Floquet-Bloch periodic boundary conditions to the edges of a single unit cell, enforcing a given propagation constant β in the x-direction. In order to simulate an infinite free space above the waveguide, the top boundary of the simulation space is set to an impedance boundary condition defined by the impedance

of free space. The structure is assumed to be uniform in mode profile and extend infinitely in the z-direction (i.e. the lateral direction). An eigenfrequency solver is used to determine the mode profile and dispersion characteristics. Using the series cutoff observed in the simulation, an effective LH capacitance can be determined ($C_L = 1/\omega_{se}^2 L_R$) and the equivalent transmission line model dispersion can determined (assuming parallel plate estimations for L_R and C_R).

Simulated dispersion data along with the subsequently determined transmission line dispersion for the structure in Figure 2.3(a) are shown in Figure 2.5. There is good agreement between the transmission line model and the simulated dispersion when looking at larger β values, but the two show very different behavior at smaller β values, within and around the light line. As the dispersion of the waveguide crosses into the light line, it will begin to radiate. At this point, there is a coupling and an anticrossing between the mode confined to the waveguide and plane wave modes excited by the radiation traveling in the air along the top metal of the waveguide. As a result of this coupling, the dispersion splits into a bound mode that hugs close below the light line and a radiating mode that hugs close above the light line. Structures with larger cantilever gaps show greater discrepancy between simulated and TL model results because there is stronger coupling to the light line through the larger opening in the waveguide. Structures with smaller gaps show weaker coupling to the light line and are more closely matched to the transmission line model.

The anticrossing at the light line has been observed experimentally by Hon, *et al.* in passive CRLH waveguide metasurfaces [98], but it is difficult to model accurately because reflections at the upper impedance boundary will cause the waveguide mode will couple to rectangular waveguide modes in the air space of the simulation rather than coupling to the true modes supported by free space. This is demonstrated in the inset of Figure 2.5, where the dispersion in and around the light line is shown to be highly dependent on geometry. Using a 100 μm tall

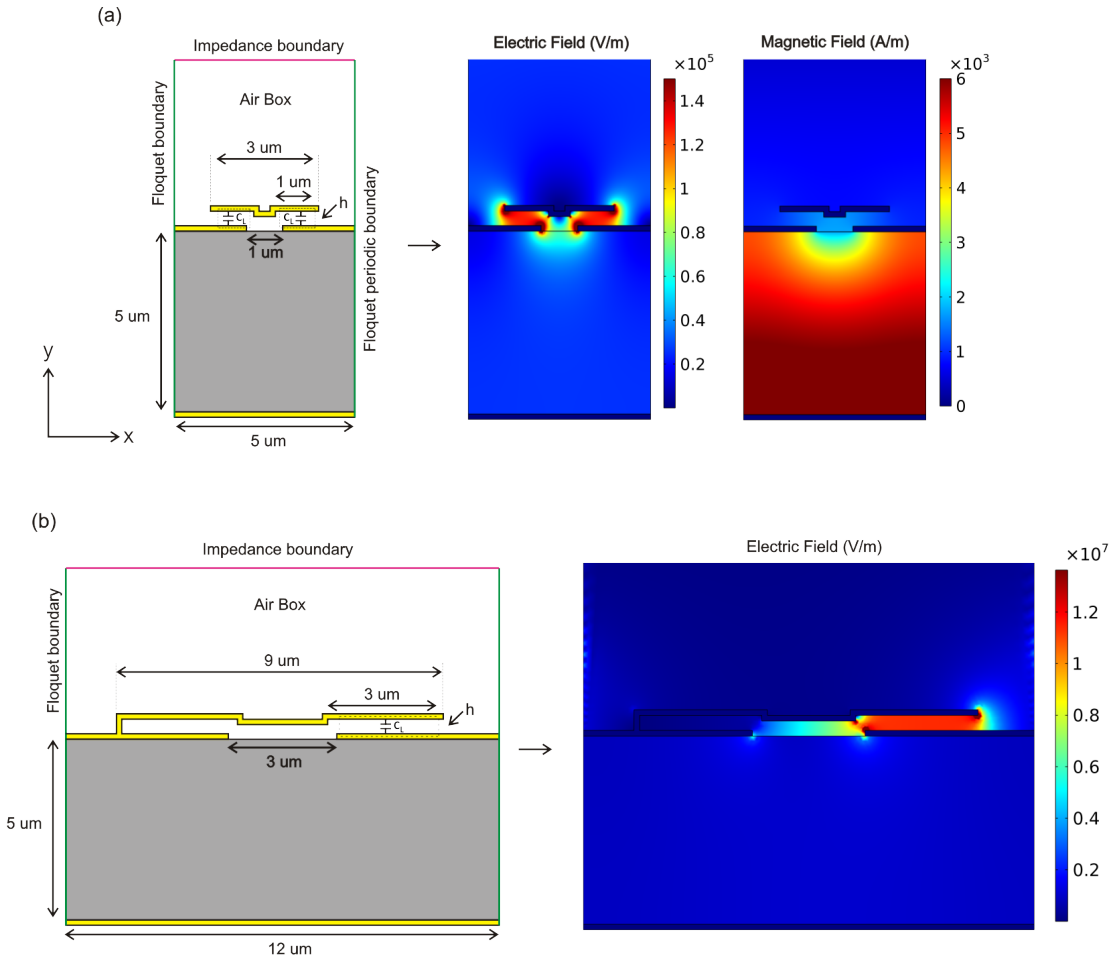

Figure 2.4: Simulation setup and eigenfrequency field profiles determined using COMSOL for (a) a 5 μm period, free-standing overlay structure, and (b) a 12 μm, self-actuated structure.

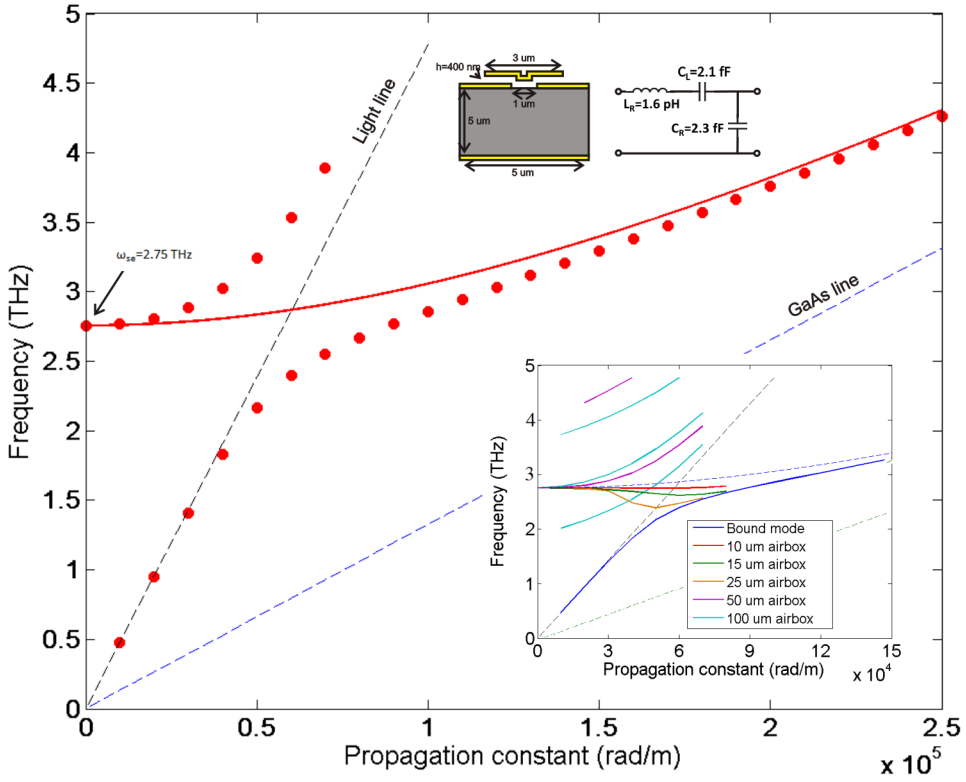

Figure 2.5: (a)Dispersion of the metamaterial anticrossed with radiative modes and the corresponding transmission line model. Inset shows the effects of simulation space on eigenfrequency solutions inside the light line. The GaAs line gives the dispersion of plane TEM waves in GaAs (the light line scaled by the refractive index of GaAs, n_{GaAs}=3.6).

air box, for example, results in several solutions inside the light line corresponding to coupling with different order modes in the airbox (see inset of Figure 2.5). However, because we are primarily interested in tunable waveguides suitable for laser resonators, the intended operating range of the proposed designs is outside the light cone, and the anticrossing will likely to be much weaker for a thin QCL ridge compared to the infinite surface of the 2D simulation. Fortunately, all geometries converge to the same cutoff frequency and the same solutions in the operating range of the device. For these reasons, in Figure 2.6, the dispersions inside the light line are not plotted, while bound mode dispersions and series cutoff frequencies are reported.

The dispersion tuning of a 5 μm period, free-standing overlay structure is shown in Figure 2.6(a). The height of the overlays over the waveguide is adjusted from 400 nm to 25 nm. For a constant wavenumber $\beta = 1.5 \times 10^5$ (rad/m), the structure shows a tuning of about 0.7 THz around a center frequency of 2.5 THz. For comparison, the dispersion tuning of a 12 μm, self-actuated structure is shown in Figure 2.6(b). The height of the cantilever is adjusted from 250 nm to 175 nm, giving a tuning of about 0.05 THz (50 GHz) around a center frequency of 2.5 THz. The actuation of a cantilever is limited to the upper third of it's initial height (in the ideal case, see section 2.4), greatly limiting its tuning range. Additionally, the 5 μm metamaterial shows more tuning because the smaller period increases the series resonant frequency, bringing the 2.5 THz operating range closer to the ω_{se}. Operating closer to the series resonant frequency suggests more of the mode's energy is in the series circuit, in turn suggesting that tuning of the series circuit will have a greater effect on the mode in this region. More formally, from the transmission line model, we can write:

$$\omega = \sqrt{\left(\frac{p^2\beta^2}{L_R C_R} + \omega_{se}^2\right)} \tag{2.10}$$

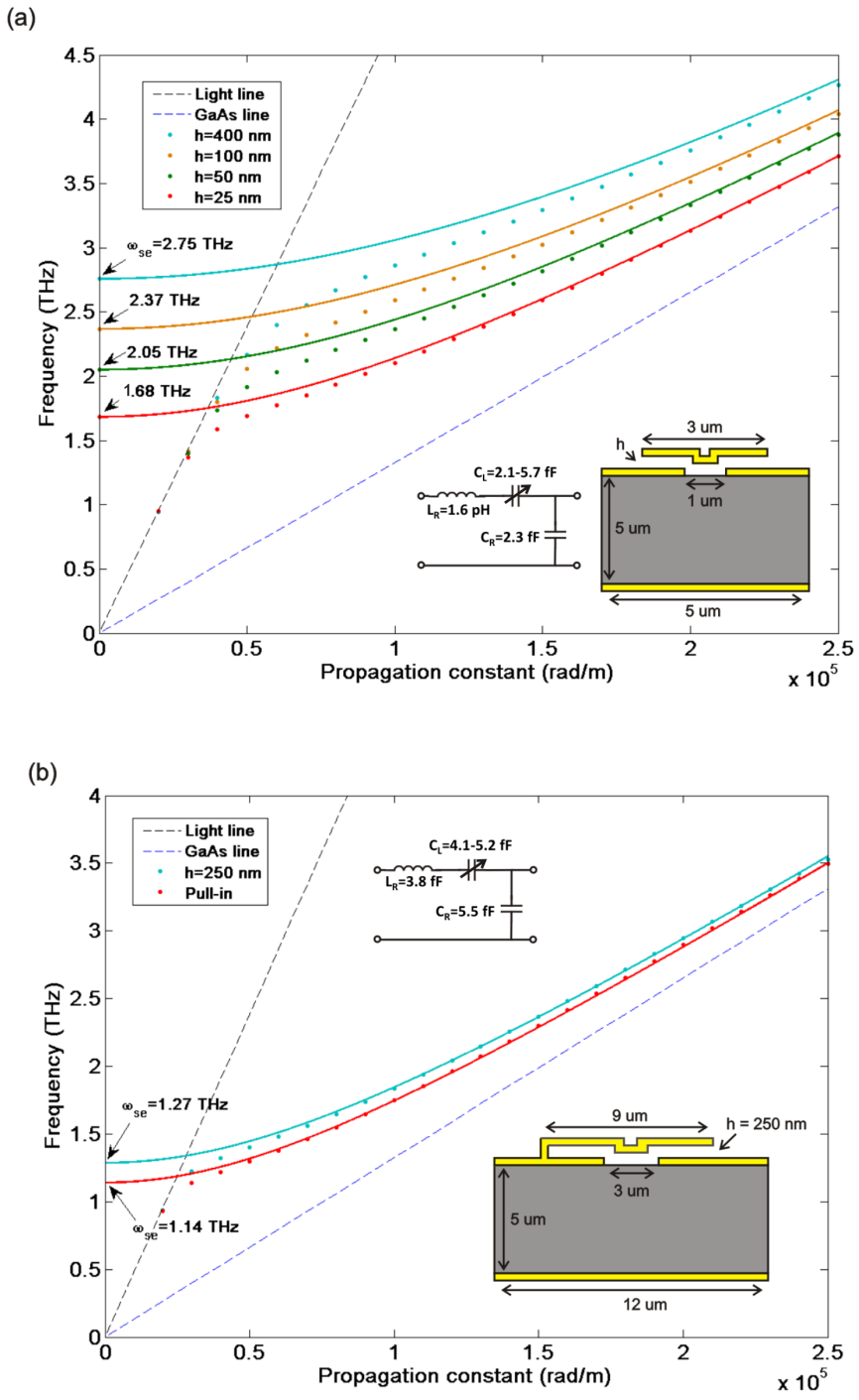

Figure 2.6: (a)Tuning of the bound modes of a 5 μm period, separately biased structure. (b)Tuning of the bound modes of a 12 μm, self-actuated cantilever structure (parallel plate estimate for cantilever C_L is 2.1-2.9 fF).

$$\left.\frac{d\omega}{dC_L}\right|_{\beta} = \frac{-1}{2L_R C_L^2}\left(\frac{L_R C_R}{p^2\beta^2 + L_R C_R \omega_{se}^2}\right)^{\frac{1}{2}} \tag{2.11}$$

where we see that frequency tunability around a fixed β is largest at smaller values of beta, closer to the cutoff frequency.

The 5 μm period design is intended not necessarily as the starting point, but rather an aggressive design, so as to demonstrate the potential of this approach. The larger, 12 μm period, self-actuated design shows significantly less tuning potential, but for initial demonstration, requires fewer processing steps and uses larger dimensions so that it will be easier to fabricate using contact lithography.

2.4 Tunable THz QCL design

In sections 2.2 and 2.3, analysis of an infinitely long metamaterial waveguide was developed. If the waveguide presented here was filled with QCL gain material, the gain material could not be biased by a single wire bond because the LH capacitances create discontinuities in the top metalization. This problem can be solved using higher order TM_{01} metamaterial designs that have continuous top contacts, but the fabrication process is notably more complex (see section 3.4). In order to develop a tunable THz QCL using the TM_{00} metamaterial designs, a two-section cavity is designed that includes a passive (i.e. unbiased) metamaterial waveguide fed by a biased metal-metal THz QCL waveguide. The passive metamaterial adds material losses to the cavity round trip, increasing the threshold gain, while coupling of the MM waveguide mode to the metamaterial mode decreases $\mathrm{d}\omega/\mathrm{d}C_L$ of the full structure compared to a purely metatmaterial structure. In this section, I will develop designs criteria to maximize tuning without increasing losses beyond the gain capabilities of the QCL.

2.4.1 Tuning of compound resonant cavity

In order to meet resonant conditions for lasing, the laser mode must have a cumulative round trip phase change given by:

$$\Delta\Phi = L_a\beta_a + L_p\beta_p = \frac{\omega}{c}(L_a n_{eff,a} + L_p n_{eff,p}) = m\pi \tag{2.12}$$

where β_a is the propagation constant in the active region, L_a is the length of the active region, m is an integer, ω is the frequency of operation, and $n_{eff,a}$, $n_{eff,p}$ are the frequency dependent effective refractive indices of the active and passive sections respectively.

In an ideal active metamaterial THz QCL, the resonant waveguide would be made entirely from active THz metamaterial. In such a uniform waveguide, laser operation would be defined by a fixed wavenumber β, forcing ω to tune as C_L is tuned. Comparatively, if ω were somehow fixed, β would be forced to tune as C_L is tuned. Discussion of frequency tuning to this point has assumed the laser operates at a constant β, where frequency tuning with C_L is a maximum. However, if we assume the total phase change $\Delta\Phi$ is locked to the $m\pi$ condition for the compound cavity, then as C_L tunes, both β_a and β_p must tune to continue lasing in the same mode (constant m integer). The new lasing frequency is determined from equation (2.12). This hybrid tuning of β and ω results in less net tuning with C_L than when ω alone is forced to tune with C_L. Assuming a constant L_a, equation (2.12) is used to determine the influence of relative passive and active lengths on the tuning of the compound cavity and the results are plotted in Figure 2.7 (see Appendix A for details on calculation). The data suggests that the majority of the frequency tuning potential is achieved if $L_p > 3L_a$.

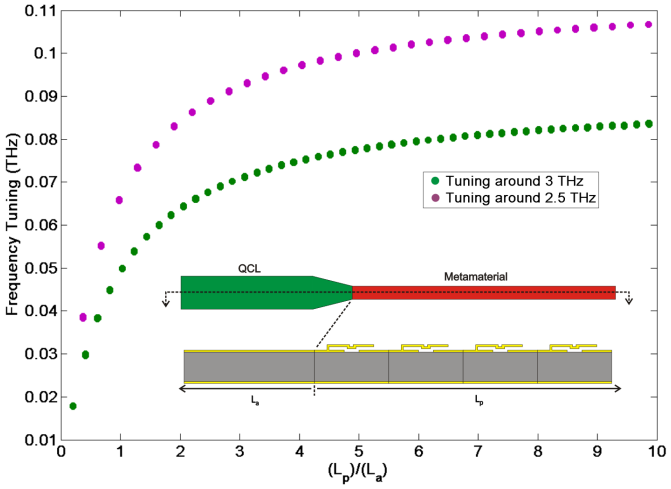

Figure 2.7: Tuning of compound resonant cavity as a function of relative active and passive section lengths. Metamaterial in question is a 12 μm self-actuated structure.

2.4.2 Three mirror resonant cavity

The compound cavity can be modeled with three reflections: two reflections from the etched facets (r_1 and r_3) and one reflection due to mode mismatch between the MM QCL and the MM metamaterial (r_2). This can be simplified to a simple two mirror laser where one mirror, representing the passive metamaterial, is given by the complex reflection of a Fabry-Perot etalon:

$$r_{eff} = -r_1 + \frac{t_1^2 r_2 \exp^{-2j\tilde{\beta}_p L_p}}{1 - r_1 r_2 \exp^{-2j\tilde{\beta}_p L_p}} \tag{2.13}$$

where L_a is the length of the active section, L_p is the length of the passive section, and β_p is the propagation constant in the passive region. Reflection coefficient r_2 can be determined using the transmission line model:

$$r_2 = \frac{Z_{meta} - Z_{MM}}{Z_{meta} - Z_{MM}} = \frac{\sqrt{\omega^2 - \omega_{se}^2} - \omega}{\sqrt{\omega^2 - \omega_{se}^2} + \omega} \tag{2.14}$$

where Z_{MM} is the characteristic impedance of a regular metal-metal QCL waveguide ($Z_{MM} = sqrt(L_R/C_R)$, and Z_{meta} is the characteristic impedance of the metamaterial design:

$$Z_{meta} = \sqrt{\frac{L_R}{C_R}}\sqrt{1 - \frac{\omega_{se}^2}{\omega^2}} \tag{2.15}$$

The threshold gain condition is then given by:

$$\Gamma g_{th} = \alpha_{mat} - \frac{1}{2L_a} ln(r_1 r_{eff}) \tag{2.16}$$

Where α_{mat} represents material losses as described by the Drude model (see section 1.3), and Γ is the modal confinement to the active region. Z_0, Z_{meta}, r_2, and r_{eff} from a lossless 300 μm metamaterial Fabry-Perot cavity are plotted in Figures 2.8(a) and (b) using the transmission line model and equation (2.35). The periodic rippling of r_{eff} is characteristic of Fabry-Perot reflectivity. As frequency increases, the rippling in r_{eff} decreases as as a result of the decreased mode mismatch between Z_{meta} and Z_{MM}. The effect of 30 cm^{-1} of material loss on the reflectivity is also demonstrated in Figure 2.8(b). The structure will lase at the reflection peak in r_{eff} that is closest to the peak of the laser gain profile. Lasing at the largest r_{eff} minimizes the threshold gain requirements, but it also means that more power is reflected due to mode mismatch r_2 and less power is be transmitted into the metamaterial, decreasing the potential to tune the structure via self-actuation. As Z_{meta} approaches Z_{MM}, less power is reflected at r_2 and r_{eff} approaches a constant equal to the reflection r_3. Bragg reflections from the period of the metamaterial will dominate at higher frequencies, but they are avoided by operating within the $\lambda_g/4$ metamaterial limit. As dispersion of the metamaterial is tuned, the reflection peaks will tune.

Material free-carrier losses in the self-actuating metamaterial design have the effect of lowering the overall magnitude of r_{eff}, as seen in Figure 2.8(b). Losses for

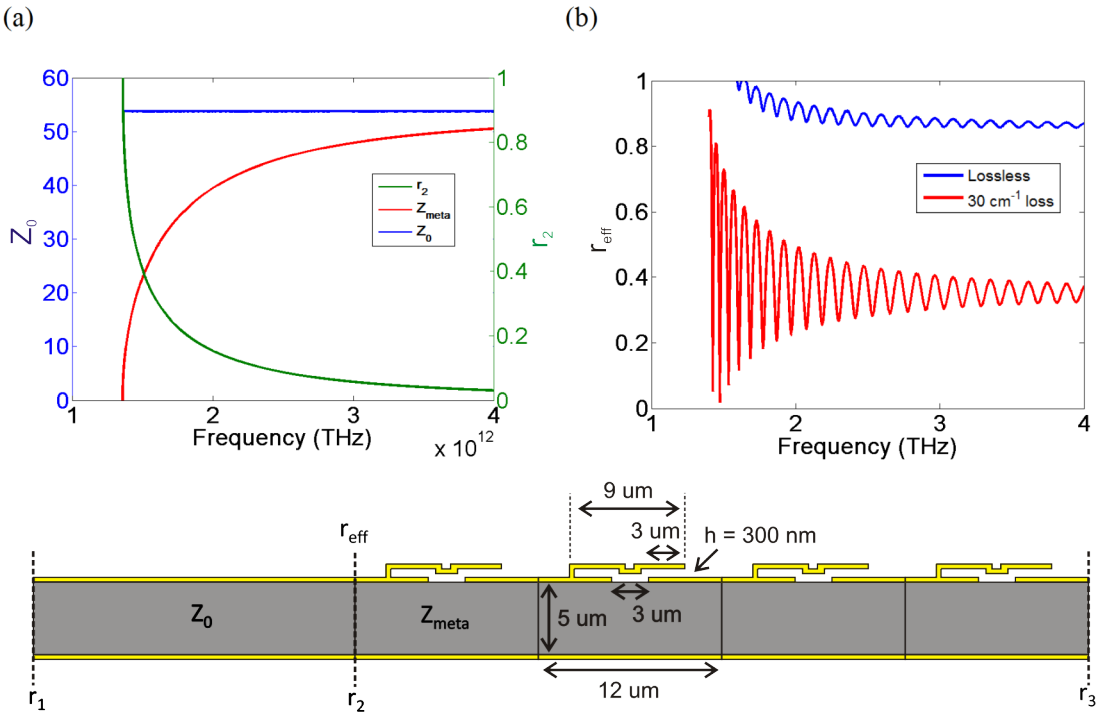

Figure 2.8: (a)Impedance of metamaterial and MM waveguides over frequency. (b)Passive 300 μm metamaterial Fabry-Perot reflectivity with and without losses (r_3=0.9)

.

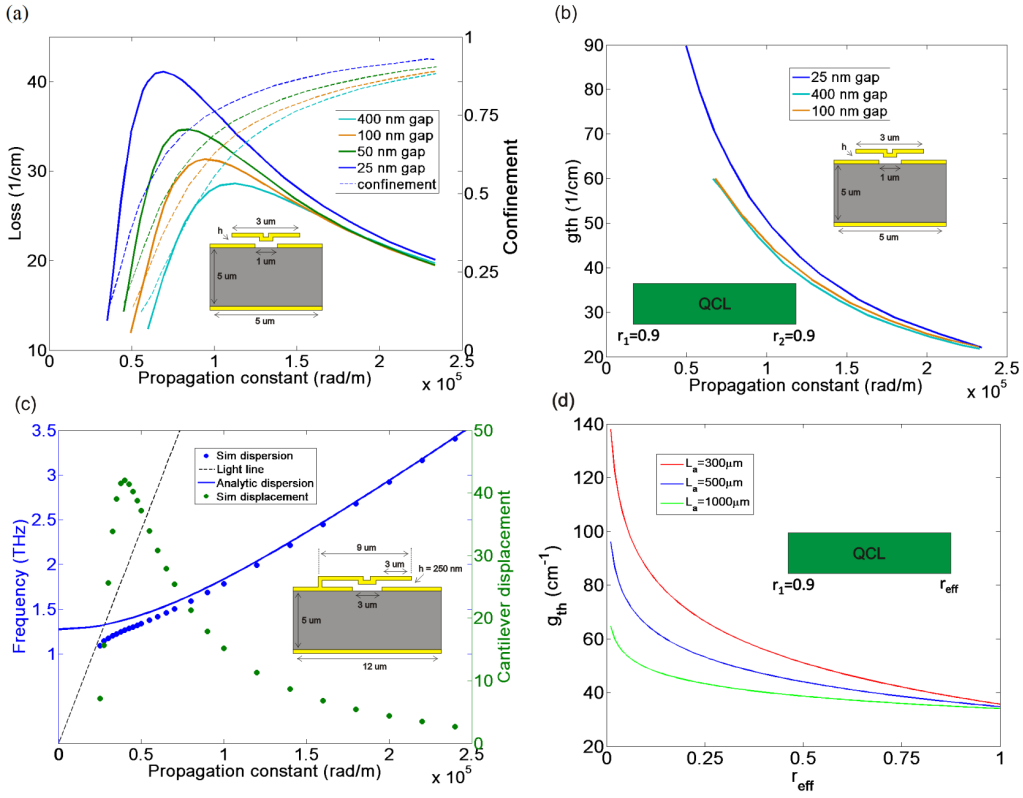

Figure 2.9: (a) Loss and confinement for a 5 μm, free-standing overlay THz metamaterial (Drude parameters: $N_{Au} = 5.9 \times 10^{28}$ cm^{-3}, $\tau_{Au} = 0.039$ ps, $m^*_{Au} = 1$, $N_{actv} = 5 \times 10^{21}$ cm^{-3}, $\tau_{actv} = 0.5$ ps, m^*_{actv}=0.067). (b)Threshold gain requirements for a THz QCL made entirely from the structure in (a). (c)Cantilever displacement due to bound modes. Displacement drops rapidly when the dispersion approaches the light line and more of the mode's power is in an evanescent wave in the air above the waveguide. (d) Threshold gain requirements as a function of facet reflectivity.

a 5 μm period metamaterial are plotted over frequency in Figure 2.9(a). Losses outside the light line are consistent with typical THz QCL losses (see Figure 1.7), showing increasing losses at lower frequencies. There is a steep drop-off in losses as the dispersion approaches the light line because confinement has decreased and most of the mode is in the air. Poor confinement along with leaky wave radiation make lasing more difficult near and within the light line. Furthermore, increased mode mismatch between the QCL and metamaterial at low β values will decrease power coupling into the metamaterial, and poor mode confinement decreases the force on the cantilever as simulated in Figure 2.9(c). For these reasons, we must operate outside the light line.

Threshold gain requirements g_{th} for an all metamaterial QCL are plotted in Figure 2.9(b), and threshold gain requirements for a metal-metal feed QCL with varying r_{eff} are plotted in Figure 2.9(d). Consider Figure 2.8(b), for example, which predicts a peak reflectivity of r_{eff} $\approx$0.45 from a 300 μm passive metamaterial section with free carrier losses of 30 cm^{-1}. Referring back to Figure 2.9(d), and assuming THz QCL gains in high quality active regions readily reach 40-60 cm^{-1}, we can predict that the feed QCL will need to be at least 300 μm long, giving $L_p/La = 1$, which gives access to about half the tuning potential of the metamaterial.

2.5 Self-actuation of cantilevers

Observing the TM_{00} eigenfrequecy mode profiles in Figure 2.4(b), we see that the mode has significant electric field strength in the fixed-free cantilever's capacitive gap. The E-field will generate a force between the cantilever and the top metal of the waveguide, but the mechanical response times of the cantilever are well below THz timescales, so the cantilever experiences a constant force from an root-mean-square voltage proportional to the electromagnetic power in the mode.

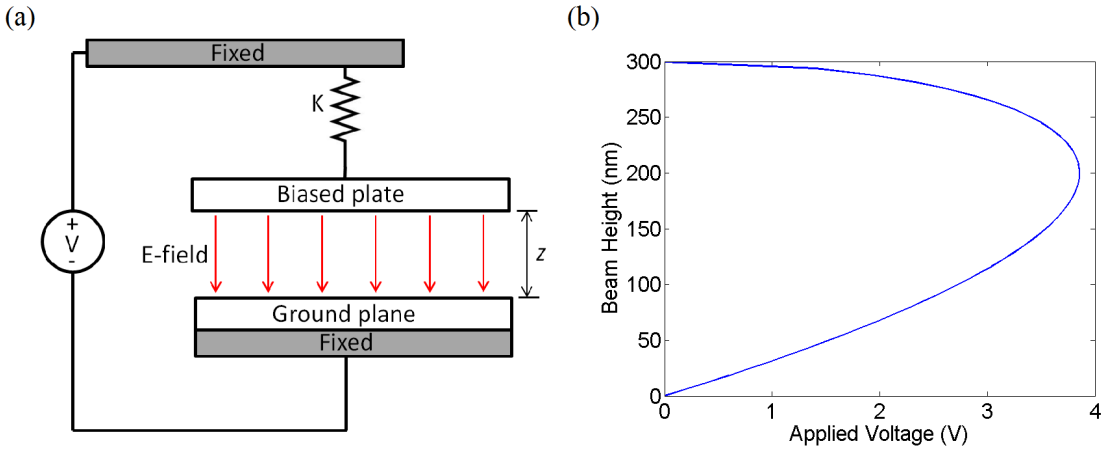

Figure 2.10: (a)Physical model for MEMS cantilevers and bridges based on a parallel plate assumption. (b)Actuation of cantilever height with applied voltage shows an instability at h≈200 nm.

The laser is tuned by sweeping the output power/bias on the QCL. In other words, the self-actuated metamaterial is in effect a nonlinear material with an intensity dependent refractive index. THz QCLs are not particularly high power sources, so it is necessary in this section to investigate the plausibility of actuating cantilevers with the power available in a typical THz QCL.

2.5.1 Mechanics of cantilevers

A simple physical model that can be applied to electrostatically actuated cantilevers is shown in Figure 2.10. The cantilever is represented by a metal plate hanging from a spring with spring constant K. This plate is held parallel with a fixed metal ground plane as an electrostatic voltage is applied between the two plates. The spacing between the plates with no voltage applied is given by z_0. The equation of motion for the system is an equivalence between the restoring force of the spring $F_M = k(z - z_0)$ and the electrostatic force of the applied voltage $F_E = -\frac{dU}{dz}$, where U is the energy stored in the parallel plate capacitor:

$$k(z - z_0) = \frac{dU}{dz} = \frac{d}{dz}\left(\frac{1}{2}CV^2\right) = \frac{1}{2}\frac{\epsilon A V^2}{z^2} \tag{2.17}$$

where C is the capacitance, V is the voltage across the capacitor, and A is the area of overlap between the plates. The restoring force is a linear function of z while the electrostatic force is a nonlinear function of z. This results in an unstable point at $z = \frac{2}{3}z_0$ as demonstrated by the plot in Figure 2.10(b). If the plate starts at z_0 and is actuated by an increasing voltage, at $\frac{2}{3}z_0$, it will pull-in to zero separation. This pull-in voltage can be determined as:

$$V_{pull-in} = V\left(\frac{2}{3}z_0\right) = \sqrt{\frac{2K}{\epsilon A}z^2\left(z_0 - \left(\frac{2}{3}z_0\right)\right)} = \sqrt{\frac{8K}{27\epsilon A}z_0^3} \tag{2.18}$$

Pull-in voltage is a well known phenomenon and is a common design parameter in MEMS work [99]. Actual pull-in voltages for MEMS cantilever and bridge structures, however, are not so easily modeled [100]. Ground planes and biased planes are not perfectly parallel, spring constants are nonlinear, and fringing fields at the edges of the plates are not accounted for in the parallel plate model in Figure 2.10.

More accurate pull-in models for MEMS cantilevers and beams have been developed in several sources [101], [108], [102]. One approach proposed by Pamidighantamn, *et al.*, is to use equation (2.18), but replace spring constant K with an effective spring constant K_{eff}, and overlap area A with effective overlap area A_{eff}. For cantilever beams, K_eff is determined by [102] as:

$$K_{eff} = \frac{2}{3}\frac{\hat{E}wt^3}{l^3}\left[\frac{3}{8 - 6\zeta_r + \zeta_r^3}\right] \tag{2.19}$$

where w is the width of the cantilever, t the thickness of the cantilever material, l the total length of the cantilever, $\zeta_r = l_{tot}/l_{ovr}$ is the ratio of the total cantilever

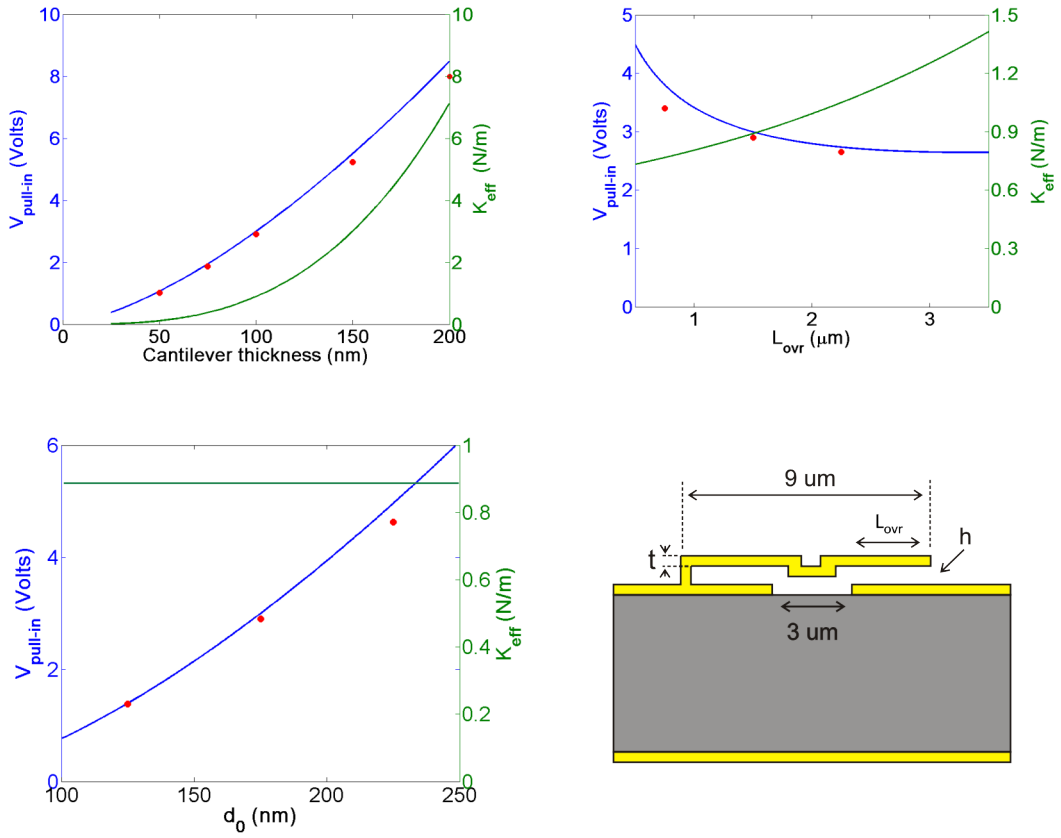

Figure 2.11: Simulated (red dots), and analytically determined (blue lines) cantilever pull-in voltage as a function of (a) initial cantilever height (constant overlap = 3 μm), (b) cantilever overlap (constant height = 250 nm), and (c) cantilever thickness (constant overlap = 3 μm, constant height = 250 nm) using K_{eff} from [102].

length to the length of the overlap area, and $\hat{E} = E/(1-\nu^2)$ is the plate modulus and E is the Young's modulus (79 GPa for room-temperature Au). A_{eff} is determined by [102] as:

$$A_{eff}(\xi, \zeta_r) = \alpha(\xi, \zeta_r) b_{eff}(\xi) l \tag{2.20}$$

$$\alpha(\xi, \zeta_r) = \frac{4}{\pi} \frac{1-\xi}{\sqrt{1-2\beta}} \left(\arctan(\sqrt{1-2\xi} - \arctan\left[(\sqrt{1-2\xi}) \tan \frac{\pi}{4}(1-\zeta_r) \right] \right) \tag{2.21}$$

$$b_{eff}(\xi) = w \left(1 + 0.65 \frac{(1-\beta)h}{w} \right) \tag{2.22}$$

where $\xi = z_{max}/h$ is the ratio of the pull-in cantilever displacement to the initial cantilever height. In Figure 2.11, pull-in voltages have been plotted using equations (2.18-2.22) for 9x20 μm Au cantilevers as a function of cantilever thickness, initial cantilever height, and cantilever overlap. For comparison, the pull-in voltage of the structure has been simulated in Comsol Multiphysics (shown in red dots).

The above expressions for fixed-free cantilever mechanics are good for initial estimations, but it should be noted that operations at cryogenic temperature will complicate cantilever behavior and likely increase cantilever pull-in voltage. For example, as temperature decreases from room temperature to 4 K, the Young's modulus of Au thin films has been reported to increase by about 5-10% depending on the quality of the film [103]. Additionally, differences between the coefficients of thermal expansion of the substrate and cantilever material causes deformation of the cantilever and increases pull-in voltage. This problem is particularly acute for fixed-fixed beam structures and can cause up to an order of magnitude increase in the actuation voltage of beams [104–106]. For all gold, fixed-free cantilevers (2.2 μm thick, 75 μm long, 40 μm wide), Gong, *et al.* have reported a 60% increase in

actuation voltage from 300 K to 4 K [107]. Both sources attribute the increase in pull-in voltage largely to cantilever deformation, and only slightly to the Young's modulus increase. Lastly, the yield of MEMS cantilevers will be important to this project as the designed structures use long arrays of cantilevers. Yield in fixed-fixed gold beams has shown to decrease from 82% to 39% as temperature decreases from 300 K to 80 K, which could pose a challenge for successful realization of this structure [105].

2.5.2 Pull-in power, transmission line model

One approach to estimating cantilever displacements and power requirements for full actuation of the THz metamaterial structure is using the transmission line model to estimate the voltage on the series capacitor and determine when it will pull-in the cantilever. The average power for TEM and quasi-TEM modes in transmission line theory is given by:

$$P_{av} = \frac{|\tilde{V}(z)|^2}{2Z_0} \tag{2.23}$$

where $|\tilde{V}(z)|$ is the magnitude of the shunt voltage phasor, and Z_0 is the characteristic impedance of the THz metamaterial transmission line given by equation (2.15).

The root-mean-square voltage across the series capacitor is given by:

$$V_{C_L,rms} = \frac{|\tilde{V_{C_L}}|}{\sqrt{2}} = \frac{|\tilde{I}(z)|Z_{C_L}(\omega)}{\sqrt{2}} = \frac{|\tilde{V}(z)|}{Z_0\sqrt{2}}\frac{1}{\omega C_L} = \frac{\sqrt{P_{avg}}}{j\sqrt{Z_0}\omega C_L} \tag{2.24}$$

substituting equation (2.23) for $|\tilde{V}(z)|$. Using the cantilever pull-in voltages calculated in section 2.5.1, we can estimate the power required to reach pull-in voltage on the cantilevers in the metamaterial, $P_{avg} = Z_0\omega^2 C_L^2 V_{pi}^2$.

2.5.3 Pull-in power, energy approach

As done in the parallel plate model, the force of the THz mode on the cantilever can be calculated as $F_{THz} = -\frac{dU_{C_L}}{dh}$, where h represents the height of the cantilever and U_{C_L} is the energy stored in the series capacitor C_L. The energy in C_L, assuming a parallel plate model is given by:

$$U_{C_L} = \frac{1}{2} C_L V_{C_L,rms}^2 = \frac{1}{2} C_L \left(\frac{P}{Z_0 \omega^2 C_L^2} \right) \tag{2.25}$$

where Z_0 is the characteristic impedance of the metamaterial transmission line, and P is the power in the transmission line. Substituting equation (2.15) for Z_0, we have:

$$U_{C_L} = -\frac{Pp\omega_{se}^2}{c\omega^2} n_g \tag{2.26}$$

where n_g is the group refractive index derived from equations (2.9) and (2.10) as:

$$n_g = c\frac{d\beta}{d\omega} = \frac{n_0}{\sqrt{1 - \frac{\omega_{se}^2}{\omega^2}}} = n_0 \sqrt{1 + \frac{C_R}{p^2 \beta^2 C_L}} \tag{2.27}$$

where $n_0 = c\sqrt{L_r C_R}/p$ is the refractive index of an unperturbed metal-metal waveguide of the same dimensions, and $\omega_{se} = (L_R C_L)^{-1/2}$. Assuming a constant power in the waveguide and a constant β, the force on a parallel plate LH capacitor, $C_L = \epsilon A/h$, as a function of plate separation h and LH capacitor energy U_{C_L} can be calculated as:

$$F_{THz,\beta}(U_{C_L}, h) = \left(\frac{dU_{C_L}}{dn_g} \right) \left(\frac{dn_g}{dC_L}\bigg|_\beta \right) \left(\frac{dC_L}{dh} \right) \tag{2.28}$$

$$= -\frac{Ppn_0}{2hc} \frac{\omega_{se}^4}{\omega^3 \sqrt{\omega^2 - \omega_{se}^2}} = -\frac{U_{C_L} \omega_{se}^2}{2h\omega^2} \tag{2.29}$$

The same force can be calculated under the assumption of constant frequency:

$$F_{THz,\omega}(U_{C_L},h)=\left(\frac{dU_{C_L}}{dn_g}\right)\left(\frac{dn_g}{dC_L}\bigg|_{\omega}\right)\left(\frac{dC_L}{dh}\right) \tag{2.30}$$

$$=-\frac{Ppn_0}{2hc}\frac{\omega_{se}^4}{\omega\left(\omega^2-\omega_{se}^2\right)^{3/2}}=-\frac{U_{C_L}\omega_{se}^2}{2h\left(\omega^2-\omega_{se}^2\right)} \tag{2.31}$$

As discussed in section 2.4, an entirely metamaterial laser should follow a fixed β analysis, but the proposed structure involves movement of both β and ω, so both models should be considered. Similar techniques for deriving optical forces on dielectric optical waveguides have been demonstrated in [109, 110]. Assuming the cantilever's equation of motion can be described by an effective spring constant K_{eff}, the cantilever tip displacement can be estimated as:

$$x=\frac{F_{THz}}{K_{eff}} \tag{2.32}$$

In simulations, the force on the cantilever can be determined numerically via integration of the time averaged Maxwell stress tensor (MST) along the cantilever:

$$\langle\mathbf{F}\rangle=\int_S\langle\mathbf{T}\rangle\cdot\mathbf{n}da \tag{2.33}$$

where s is the surface of the cantilever, $\mathbf{n}$ is the unit vector normal to the cantilever surface, and $\mathbf{T}$ is the MST given by:

$$\mathbf{T}=\epsilon\epsilon_0\mathbf{EE}+\mu\mu_0\mathbf{HH}-\frac{\mathbf{I}}{2}(\epsilon\epsilon_0\left|\mathbf{E}\right|^2+\mu\mu_0\left|\mathbf{H}\right|^2) \tag{2.34}$$

where $\mathbf{I}$ is the identity tensor. Cantilever displacement can be directly simulated through application of the MST to a Comsol structural mechanics solver.

Figure 2.12 shows a comparison of $F_{THz,\omega}$ and $F_{THz,\beta}$ calculated using equations (2.29) and (2.31) assuming a constant power of 100 mW in the 12 μm self-actuated structure. $F_{THz,\omega}$ is observed to be considerably larger than $F_{THz,\beta}$ because group index n_g changes more quickly with C_L for a constant ω compared to a constant β:

$$\left(\left.\frac{dn_g}{dC_L}\right|_{\omega}\right) < \left(\left.\frac{dn_g}{dC_L}\right|_{\beta}\right) \tag{2.35}$$

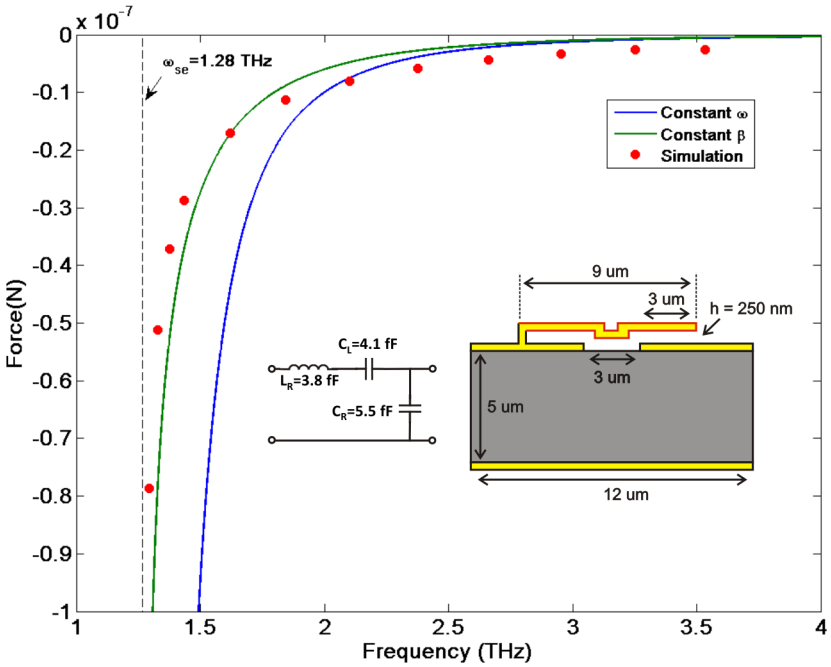

Figure 2.12: Forces calculated for constant β and constant ω expressions as well as simulated force on the cantilever. Parallel plate estimation for C_L is 2.1 fF

The forces extracted from simulations are also plotted in Figure 2.10. At lower frequencies, the simulated forces seem to be in better agreement with the constant β expression. At higher frequencies, the constant β and ω expressions converge to similar results, while the simulated force is a little larger. This is likely due to the inaccuracy of describing the series capacitance by a parallel plate capacitor, as is also observed in the discrepancies between extracted values of C_L and those calculated using the overlap of the cantilever.

For comparison, consider the force resulting from the total change in the energy in the waveguide (not just the change in U_{C_L}) when a constant power is applied:

$$U_{tot} = \frac{Ppn_g}{c} \tag{2.36}$$

The force, assuming constant β, can be derived as done previously:

$$F_{THz,\beta}(U_{tot}, h) = \left(\frac{dU_{tot}}{dn_g}\right)\left(\left.\frac{dn_g}{dC_L}\right|_{\beta}\right)\left(\frac{dC_L}{dh}\right) \tag{2.37}$$

$$= -\frac{Ppn_0}{2hc}\frac{\omega_{se}^2}{\omega\sqrt{\omega^2 - \omega_{se}^2}} = -\frac{U_{tot}\omega_{se}^2}{2h\omega^2} \tag{2.38}$$

The expression is the same in terms of energy as that in equation (2.29), appropriate expression for energy just needs to be used. The force from U_{tot} accounts for forces on all elements of the waveguide and is determined in simulations by integrating the MST over all surfaces of the waveguide unit cell. In Figures 2.13 and 2.14, constant β equations (2.29) and (2.38) are plotted along with their equivalent simulated forces for varying cantilever structures. It's observed that in all cases, the expression for total force from equation (2.38) is consistently in good agreement with integration of the MST along all surfaces of the unit cell. Results of equation (2.29) compared with the simulated forces on the cantilever alone show little agreement and suggests that the confinement of C_L to the cantilever gap is highly dependent on the specific geometry and cantilever height. It's observed, however, that the simulated force on the cantilever alone never larger than the total possible force predicted by equation (2.38).

2.5.4 THz metamaterial effective nonlinear index

Similar to the force calculation above, the actuation of the cantilevers and tuning of the structure can be described by the change in effective index:

$$\Delta n_{eff} = \left(\frac{dn_{eff}}{dC_L}\right)\left(\frac{dC_L}{dh}\right)\Delta h \tag{2.39}$$

Using the expressions for K_{eff} (eqn. (2.18)) and $F_{THz,\beta}$ (eqn. (2.29)) calculated above, Δh can be determined as a function of power and $\Delta n_{eff,\beta}$ can be written in terms of an intensity dependent nonlinear index:

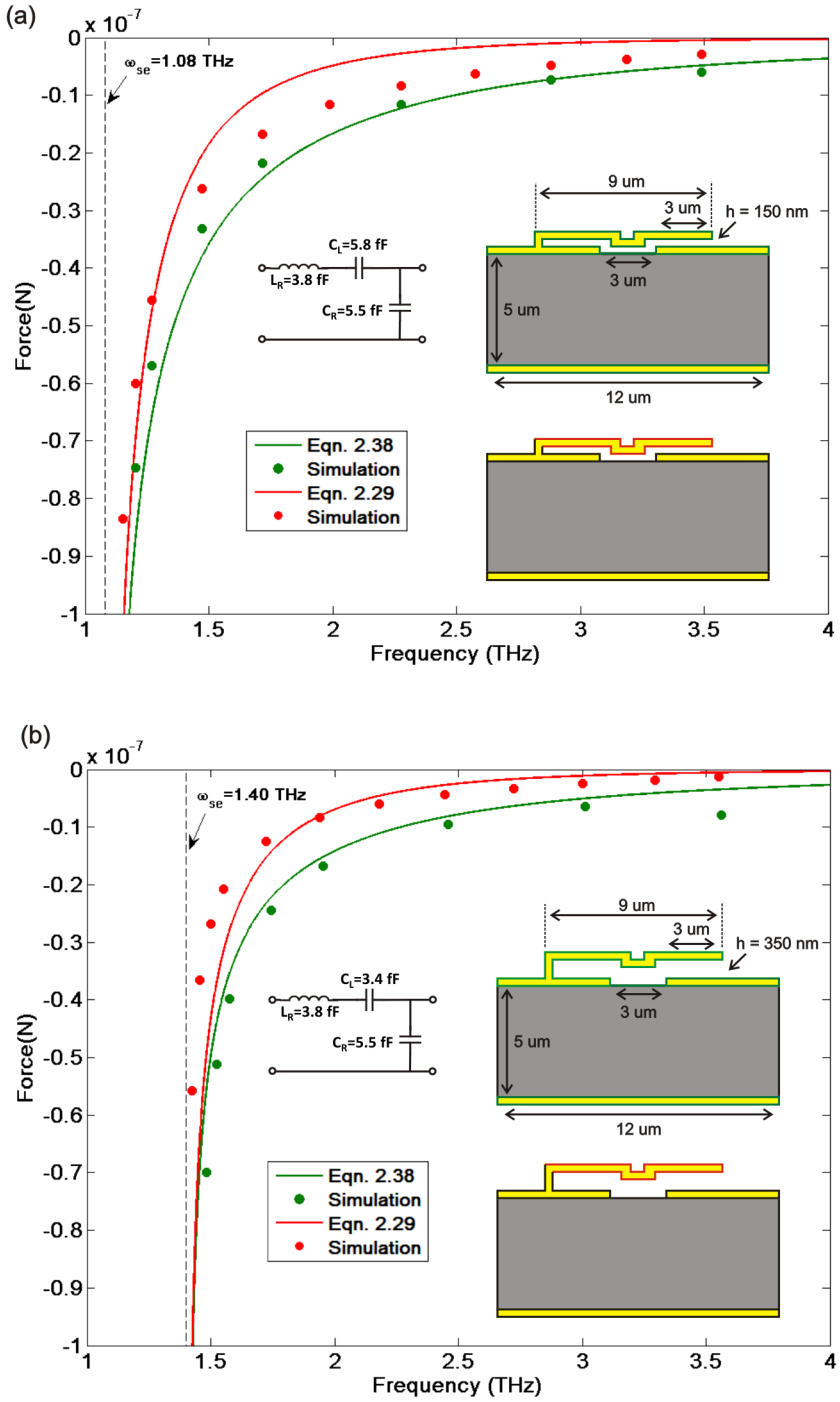

Figure 2.13: Varying initial height. Forces calculated using equations (2.29) and (2.38) compared to simulated forces extracted from simulations. Parallel plate estimations for C_L are (a) 3.5 fF and (b) 1.5 fF

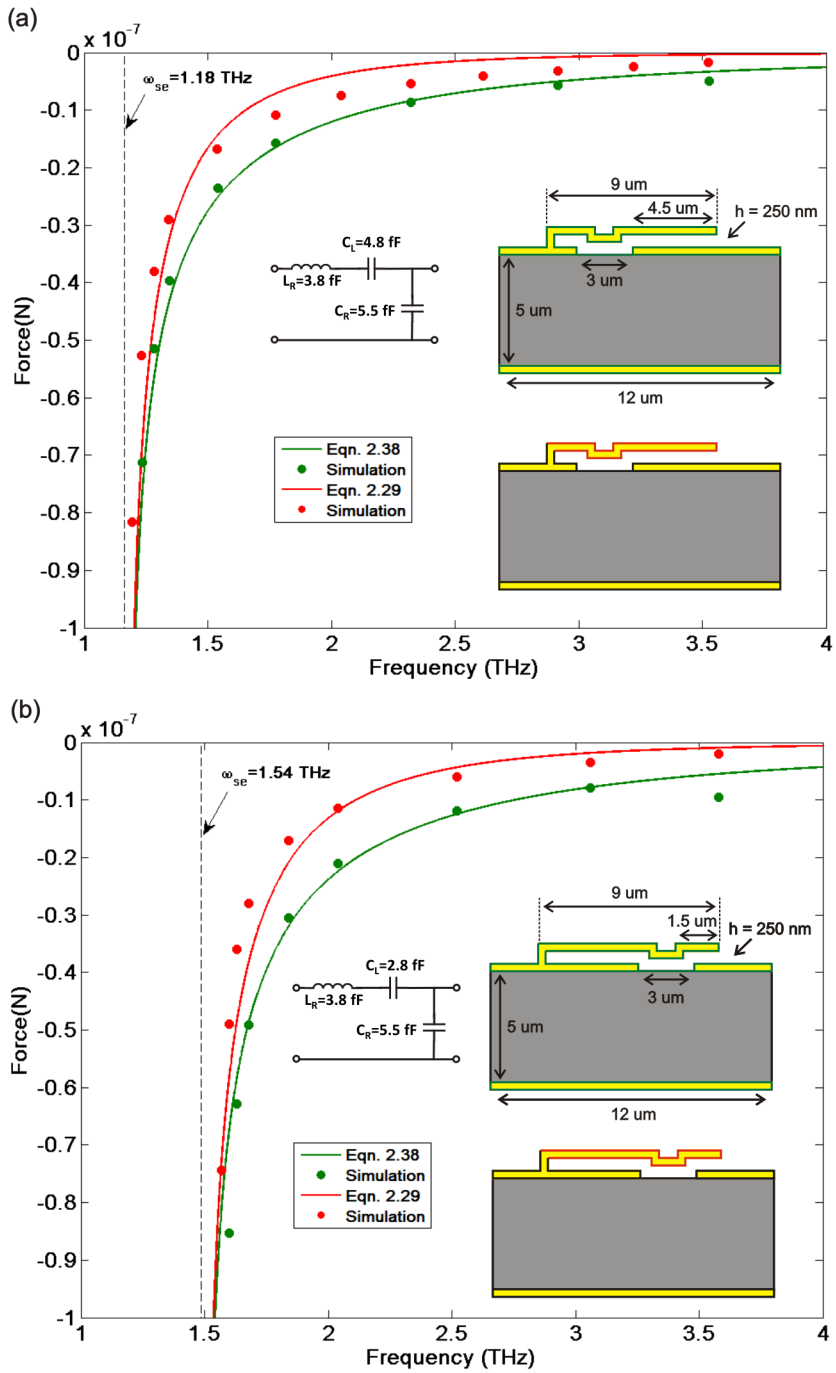

Figure 2.14: Varying cantilever overlap. Forces calculated using equations (2.29) and (2.38) compared to simulated forces extracted from simulations. Parallel plate estimations for C_L are (a) 3.2 fF and (b) 1.1 fF

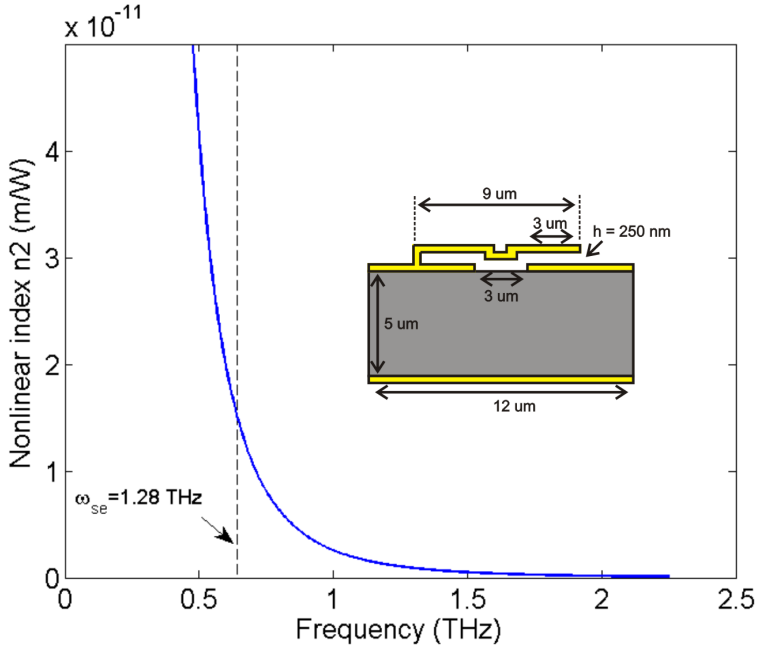

Figure 2.15: Nonlinear coefficient assuming cantilever spring constant K_{eff}.

$$\Delta n_{eff} = \left(\frac{dn_{eff}}{dC_L}\right)\left(\frac{dC_L}{dh}\right)\left(\frac{F_{THz,\beta}}{K_{eff}}\right) \tag{2.40}$$

$$= \left(\frac{pn_0^2\omega_{se}^4}{4Kh^2c\omega^4}\right)P = n_{2,\beta}\frac{P}{tw} \tag{2.41}$$

Few naturally occurring materials show strong nonlinear properties in the THz range. The nonlinear index described here reflects a slow nonlinear process limited by the resonant frequency of the cantilever (simulated to be ≈4-7 MHz depending on cantilever thickness). This nonlinearity can be used for slower-speed applications such as switching and tuning, and does not require such high field intensities.

A number of research efforts are studying fast terahertz nonlinear properties in semiconductor material systems, superconducting thin-films, and graphene structures for development of traditional nonlinear processes in the terahertz, such as frequency mixing [112–114]. Very high field intensities are needed to activate these

nonlinear process. THz metamaterials have been noted as a good platform for the development of ultrafast nonlinear THz processes due to high E-field regions associated with the subwavelength confinement of many metamaterials [115]. The metamaterial transmission lines presented here, for example, have strong field enhancement in the cantilever gaps. Deposition of nonlinear materials inside the gaps could allow access to the fast THz nonlinear properties of these materials without the need for extremely high intensity THz sources. Nonlinear index n_2 from equation (2.41) is plotted in Figure 2.15.

2.5.5 Comparison

The initial goal was to determine if a THz QCL can produce enough average power to fully actuate the Au cantilevers in the metamterial. We've developed two models for the actuation of the cantilevers by the fields in the waveguide: one based on voltage calculations, one based on force calculations. In addition, the actuation has been simulated in COMSOL. Using the K_{eff} model from [102], the power requirements for actuation around 2.5 THz based on these different analysis techniques are tabulated for comparison in Figure 2.16. Assuming the simulated result is most accurate, the pull-in power calculated using $F = dU/dh$ is too large. This is expected because the force predicted in section 2.5.3 was too small. The power requirements predicted by the transmission line model are also too large, suggesting again that C_L is not strictly defined by the cantilever gap. Fortunately, both models provide results that are within about a factor of two of the simulated value, and both models are consistent in their error, making rough estimation possible.

The data in Figure 2.16 shows that the pull-in power requirements can be decreased by decreasing the cantilever height and decreasing the overlap, but the strongest factor determining cantilever pull-in is the thickness of the deposited cantilever. Based on reported reflectivities at MM THz QCL facets and typical

h = 250 nm, overlap = 3 um			
Cantilever thickness	Pull-in power, sim	Pull-in power, TL model	Pull-in power, force model
50 nm	132 mW	200 mW	338 mW
75 nm	484 mW	684 mW	1.14 W
100 nm	1.16 W	1.64 W	2.71 W
150 nm	4.00 W	5.34 W	9.12 W

Overlap = 3 um, thickness = 100 nm			
Cantilever height	Pull-in power, sim	Pull-in power, TL model	Tuning around 2.5 THz
150 nm	530 mW	742 mW	62 GHz
250 nm	1.16 W	1.64 W	65 GHz
350 nm	1.80 W	2.70 W	70 GHz

h = 250 nm, thickness = 100 nm			
Cantilever overhang	Pull-in power, sim	Pull-in power, TL model	Tuning around 2.5 THz
1.5 um	840 mW	1.07 W	65 GHz
3 um	1.16 W	1.64 W	65 GHz
4.5 um	1.47 W	2.20 W	59 GHz

Figure 2.16: Power requirements for cantilever pull-in. Cantilever thickness has the largest influence on pull-in.

THz QCL output powers, circulating powers in THz QCLs should be ≈100 mW to 1 W, suggesting that full range self-actuation of the purposed THz metamaterial is plausible if the cantilevers can be fabricated thin enough, and if we have access to high quality THz QCL materials [89]. The frequency tuning of the structure is relatively independent of the specific cantilever positioning and height. For details on the current status of fabrication results and device testing, see Chapters 3 and 4.

2.6 Higher order THz metamaterial design

As discussed in section 2.4, the metamaterials presented thus far are designed to operate in the TM_{00} mode and require series capacitive gaps that break the continuity of the top metalization. This makes it challenging, if not impossible to bias a metamaterial QCL directly, resulting in two section cavity designs that

have larger losses and decreased tuning capabilities. In order to directly bias the metamaterial, higher order TM_{01} metamaterial designs are under investigation.

A number of theoretical and experimental demonstrations of non-tunable TM_{01} THz metal-metal metamaterial designs have been published by previous researchers in this lab [36, 80–82, 98]. The design of a tunable TM_{01} THz metamaterial is presented in Figure 2.17. The design is based on a non-tunable TM_{01} "meander" design presented in [50] and can be loosely described as two metal-metal THz waveguides with left-handed series capacitors coupled together via a left-handed inductance (see transmission line model in Figure 2.17(b)). By alternating the series capacitive gaps for each of the coupled waveguides, the top metalization of the metamaterial waveguide can be made continous and can be biased using a single wire bond at one end of the waveguide. The inclusion of a left-handed inductor gives rise to a left-handed branch in the dispersion, making this design a composite right/left handed (CRLH) metamaterial transmission line as described in section 2.2.

In Figure 2.17(c), the dispersion of the TM_{01} mode determined using a 3-D FEM eigenfrequency solver (COMSOL) is plotted in red dots. The series cutoff frequency is given by $\omega_{se} = (L_R C_L)^{-1/2}$ and the shunt cutoff frequency is given by $\omega_{sh} = (L_L C_R)^{-1/2}$. The larger of the two cutoff frequencies gives the RH-branch cutoff while the smaller of the two gives the LH-branch cutoff. In the design presented in Figure 2.17, the RH-branch cutoff is given by ω_{se} while the LH-branch cutoff is given by ω_{sh}, but it is possible to flip the two by adjusting the geometry of the unit cell. The waveguide also supports a fundamental right-handed TM_{00} mode, which is plotted using blue dots.

The unit cell of a non-tunable TM_{01} meander design is shown in Figure 2.17(a). Similar to the TM_{00} designs presented in section 2.3, tunability can be provided by the addition of self-actuated or separately biased cantilevers over the series capacitive gaps. Because self-actuated designs provide less tuning and require

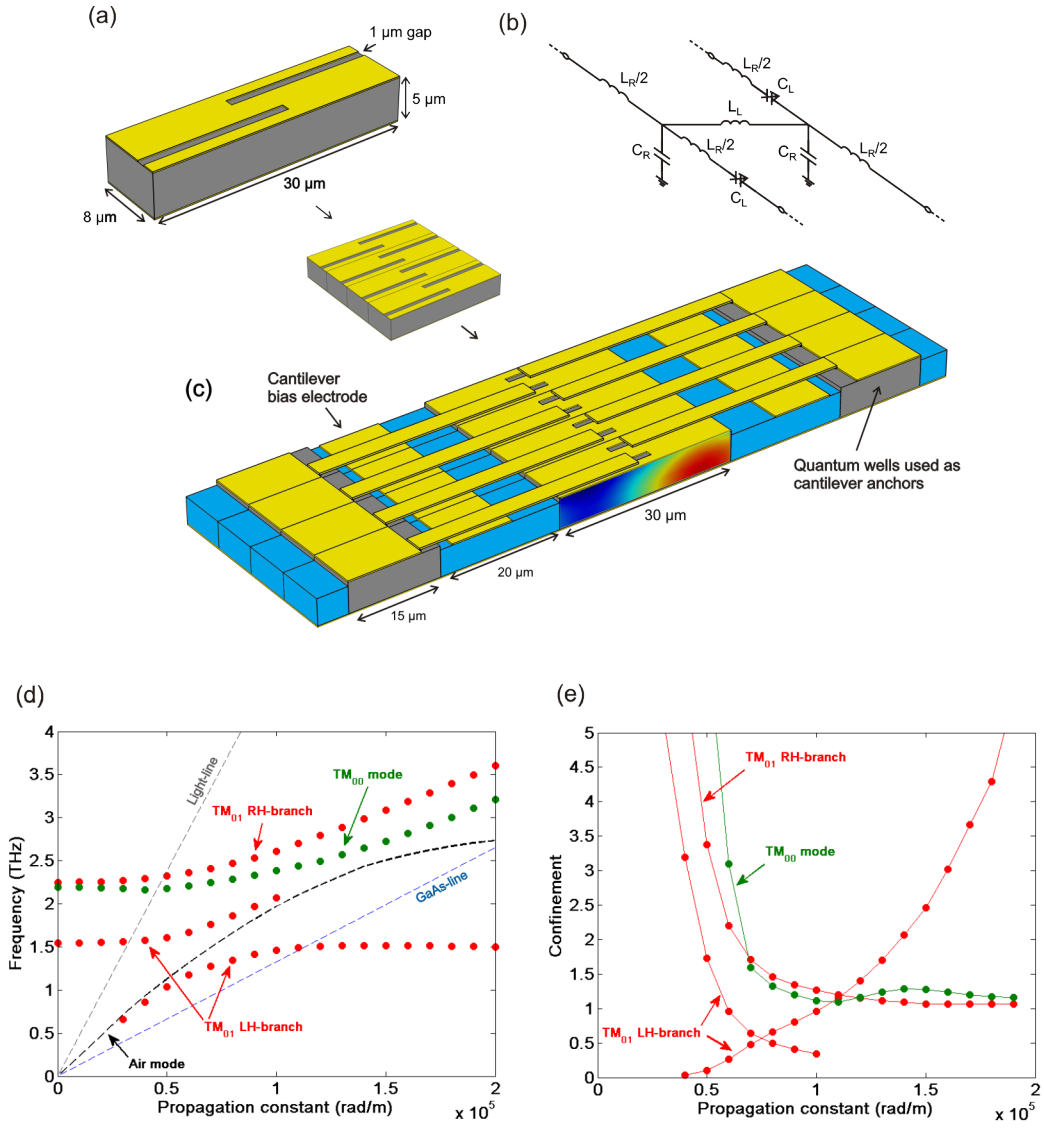

Figure 2.17: (a)Unit cell of a TM_{01} metamaterial design. (b)Approximate transmission line model. (c)Full structure for tunable TM_{01} metamaterial design with TM_{01} E-field profile shown. (d)Simulated dispersion of TM_{01} and TM_{00} mode with simulated dispersion of anticrossed air-mode plotted as black dashed line. (e)Group-index-scaled confinement factor for TM_{01} and TM_{00} modes (using equation (1.2)). Confinement is $\geq$1 through the entire dispersion of the RH-branch and the fundamental mode while the LH-branch confinement drops to nearly zero at the anticrossed point.

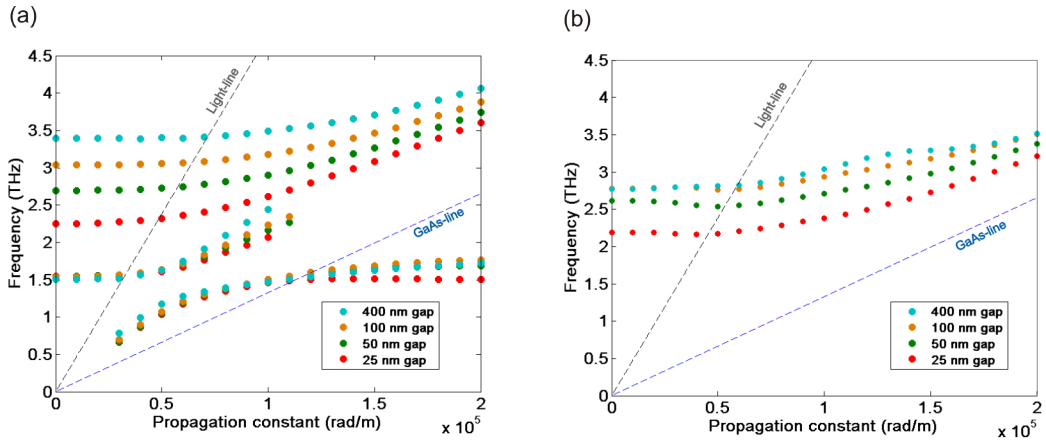

Figure 2.18: Meander design. (a)Tuning of TM_{01} mode. (b)Tuning of TM_{00} mode.

high THz QCL power, only separately biased structures are considered here. The full geometry of the simulated structure is shown in Figure 2.17(c). It is important to simulate the full structure (including cantilever anchors and bias electrodes) because the near proximity of such metallic structures to the waveguide could influence the actual dispersion of the structure as well as the confinement of the mode to the QCL gain region. Indeed, this is observed in Figure 2.17(d), where the LH-branch shows an anticrossing with a mode primarily confined in the air between the cantilevers and their bias electrodes (simulated air mode dispersion is plotted as a dashed black line). The anticrossing leads to poor modal confinement of the LH-branch, but should be of little concern because we intend to operate at higher frequencies in the RH-branch. If the bias electrodes are removed, the dispersion is the same, but without an anticrossing in the LH-branch.

Tuning of the TM_{01} metamaterial is shown in Figure 2.18(a). The RH-branch of the design shows ≈1 THz of tuning around 3 THz (33% fractional tuning), while the LH-branch shows little movement. The transmission line model in Figure 2.17(b) gives a good qualitative understanding of this tuning, suggesting that actuation of the cantilevers corresponds to tuning of the series capacitors C_L, while the LH-branch elements C_R and L_L are largely unaffected. The analytic

dispersions can be solved as eigenvalue problems using the transmission line model, but it is difficult to closely match this result to the simulated result as the detailed transmission line characteristics of the meander design may be more complex than that drawn in Figure 2.17(b). Tuning of the TM_{00} mode is plotted in Figure 2.8(b) and shows ≈0.65 THz of tuning around 2.5 THz (25% fractional tuning). Restricting the QCL operation to either the TM_{00} mode or the TM_{01} mode can be challenging, so it is encouraging to see such large tuning regardless of the mode that lases. Simulated voltage requirements to actuate cantilevers in Figure 2.17 through 500 μm ranges from 15-70 V as the thickness of the cantilever is adjusted from 200-500 nm.

Material losses for the structure have not been calculated yet due to the large computational demand associated with fine meshing of the metallic regions. It's noted, however, that modes outside of the light-cone (where we intend to operate) show similar material losses between plain metal-metal waveguides and the metamaterial waveguides presented in section 2.4. Considering that the the TM_{01} RH-branch and the fundamental mode both show strong confinement to the active region, it may be safe to assume material losses will again be similar.

Lastly, it is important to set the bias on the top metalization of the waveguide equal to the bias on the cantilevers so that the series capacitive gaps can be actuated over the larges range possible. Small potential differences between the top metalization and the cantilevers can cause pull-in to occur earlier. Such early pull-in could be a serious problem in the separately biased TM_{00} metamaterial designs presented in section 2.3.

2.7 Summary

In this chapter, the design and analysis of tunable THz metamaterials based on transmission line theory has been presented, as well as the applicability of such

metamaterials to designing a tunable THz QCL. Large tuning ranges of up to $\Delta f/f = 30\%$ are predicted for TM_{00} and TM_{01} designs with small features and full cantilever actuation capabilities, while smaller tuning ranges of ≈50 GHz around 2.5 THz is predicted for self-actuated, large feature TM_{00} devices. Self-actuation of cantilevers generally requires upwards of 1 W of power circulating inside the QCL, but could be brought down to almost 100 mW if cantilevers are made thin enough. Assuming about 10% of the power from a THz QCL is coupled to free space, actuating these cantilevers should be possible assuming 1-10 mW of peak output power can be achieved (which are relatively average peak output powers for quality THz QCL devices). In the following chapter, I discuss fabrication techniques for self-actuated and separately-biased designs and present current results for attempted self-actuated THz QCLs fabrication.

CHAPTER 3

QCL ridge waveguide fabrication and modeling

3.1 Introduction

In order to realize the development of real, working tunable THz QCL devices, proposed fabrication processes have been developed for THz metamaterials with self-actuated and separately biased cantilevers. In this chapter, I will detail the fabrication processes and discuss the results of an attempt to fabricate self-actuated THz QCL devices using 5 μm thick active regions grown by Dr. John Reno at Sandia National Laboratories.

3.2 MM self-actuated fixed-free cantilever metamaterial fabrication

Figure 3.1 gives a slightly more detailed look at the heterostructure growth prior to metal-metal bonding. The top of the heterostructure (that will be bonded to the n-doped GaAs wafer) is capped with a 500 $\mathring{A}$, 5×10^{18} cm^{-3} Si n-doped GaAs layer (typical bulk n-doping limit in GaAs), followed by a 100$\mathring{A}$, 5×10^{19} cm^{-3} Si n-doped GaAs layer (surface pinning of the Fermi level to mid-bandgap allows for particularly high surface doping density). The 100 $\mathring{A}$ highly doped surface layer of GaAs creates a large space charge density near the surface that facilitates electron tunneling through defect states, establishing an ohmic contact. To prevent this layer from oxidizing and subsequently being removed by the pre-

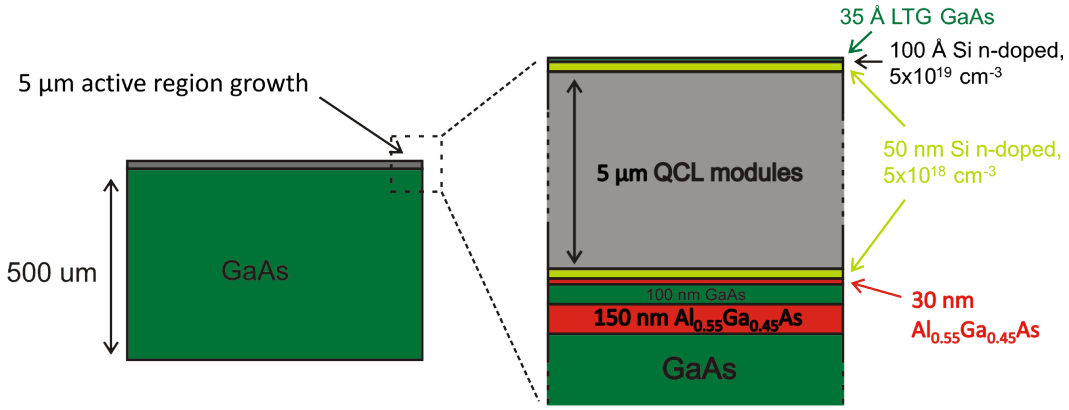

Figure 3.1: Details of QCL wafer growth. 5 μm of QCL modules are grown on top of a ≈500 μm GaAs wafer. Close up shows the QCL modules are sandwiched between Si-doped GaAs contact layers, and $Al_{0.55}Ga_{0.45}As$ substrate-removal etch-stop layers are grown below the contact layer.

metal evaporation BOE dip, the surface is passivated with a 35 $\mathring{A}$ low-temperature grown (LTG) GaAs. The bottom of the heterostructure is forwarded by a 600 $\mathring{A}$, 1×10^{18} cm^{-3} Si n-doped GaAs layer that will form a Schottky contact on top of the QCL. This bottom contact layer sits on top of two $Al_{0.55}Ga_{0.45}As$ etchstop layers separated by 100 nm of undoped GaAs. These etch stop layers are used for controlled removal of the GaAs substrate.

Starting with this growth, the following process is used to fabricate the self-actuated, cantilever based metamaterial of Figure 2.3(b). Upon receiving the QCL wafers, small pieces (≈1×1 cm) are cleaved and individually processed as follows (see Figure 3.2 for reference):

1. Evaporate Ta/Cu (300/3000 $\mathring{A}$) on top of the QCL growth and on top of a n+ doped GaAs receiving substrate immediately after a 10 second BOE dip to remove native oxide.

2. Bond the metalized surfaces of QCL wafer and the receiving GaAs wafer using thermocompression bonding.

3. Deposit 3000 $\mathring{A}$ of SiO_2 on the backside of the bonded pair (the back of the n+ GaAs wafer) using PECVD. This is for protection of the backside during steps 4-6.

4. Mechanically lap the top of the bonded pair (backside of the QCL wafer) down to $\approx$50 μm.

5. Wet etch the rest of the $\approx$50 μm GaAs remaining on top of the heterostructure growth using NH_4OH:H_20_2 (1:25). The etch stops on a 1500 $\mathring{A}$ AlGaAs etchstop layer grown on top of the heterostructure.

6. Remove the etchstop layer with 49% concentrated HF ($\approx$10 second dip).

7. Remove additional 1000 $\mathring{A}$ epitaxial GaAs layer with NH_4OH:H_20_2 (1:100). Lower NH_4OH conentration is used for a more controlled etch of the epitaxial layer compared to the fast bulk etching in step 4. The etch stops on a second AlGaAs etchstop layer.

8. Remove the second etchstop layer (300 $\mathring{A}$ thick) with 49% concentrated HF.

9. Deposit Cr/Au (200:1500 $\mathring{A}$) for for the top contact using standard negative contact photolithography techniques (include a BOE dip prior to the deposition to remove native oxide).

10. Etch away exposed n-doped contact layer between series capacitive gaps with NH_4OH:H_20_2 (1:100). This prevents shorting of the series capacitors and decreases the free-carrier losses in the metamaterial.

11. Deposit 250 $\mathring{A}$ of SiO_2 using PECVD and etch openings for cantilever contact.

12. Evaporate Cr/Au (20/200 $\mathring{A}$) for the cantilever overlays using standard negative photolithography.

13. Evaporate 2000 $\mathring{A}$ Ni mask for mesa definition using standard negative photolithography.

14. Dry etch 5 μm ridges into the QCL growth using ICP-RIE with BCl_3 chemistry.

15. Remove remaining Ni mask using Transene Ni etchant.

16. Evaporate Cr/Au (200/2000 $\mathring{A}$) onto the back n+ GaAs surface after a BOE dip for back contact.

17. Remove SiO_2 sacrificial layer to release cantilevers. To avoid cantilever stiction, two etch option are: a wet BOE etch followed by critical point drying, or an HF vapor etch.

3.3 Fabrication results

An SEM of first fabrication attempts is shown in Figure 3.3 prior to cantilever release. Cross sectional cuts of an unreleased cantilever shown in Figure 3.4 reveal that poor sidewall coverage during the oxide deposition resulted in discontinuities in the cantilever metal. As a result, the cantilever structure won't stand upon release. Cantilever thicknesses of 200 nm and 350 nm were attempted, but both showed problems with cantilever continuity. The problem may be resolved by developing a more effective oxide deposition recipe. Additionally, the use a of carousel planetary wafer holder during metal evaporation should improve sidewall coverage but could make photoresist lift-off more challenging. Despite these issues with cantilever continuity, cantilever release etches have been attempted with both critical point drying and HF vapor etching, but results are currently inconclusive due to compatibility issues of the CPD and HF etcher with small wafer pieces. These issues are currently being resolved.

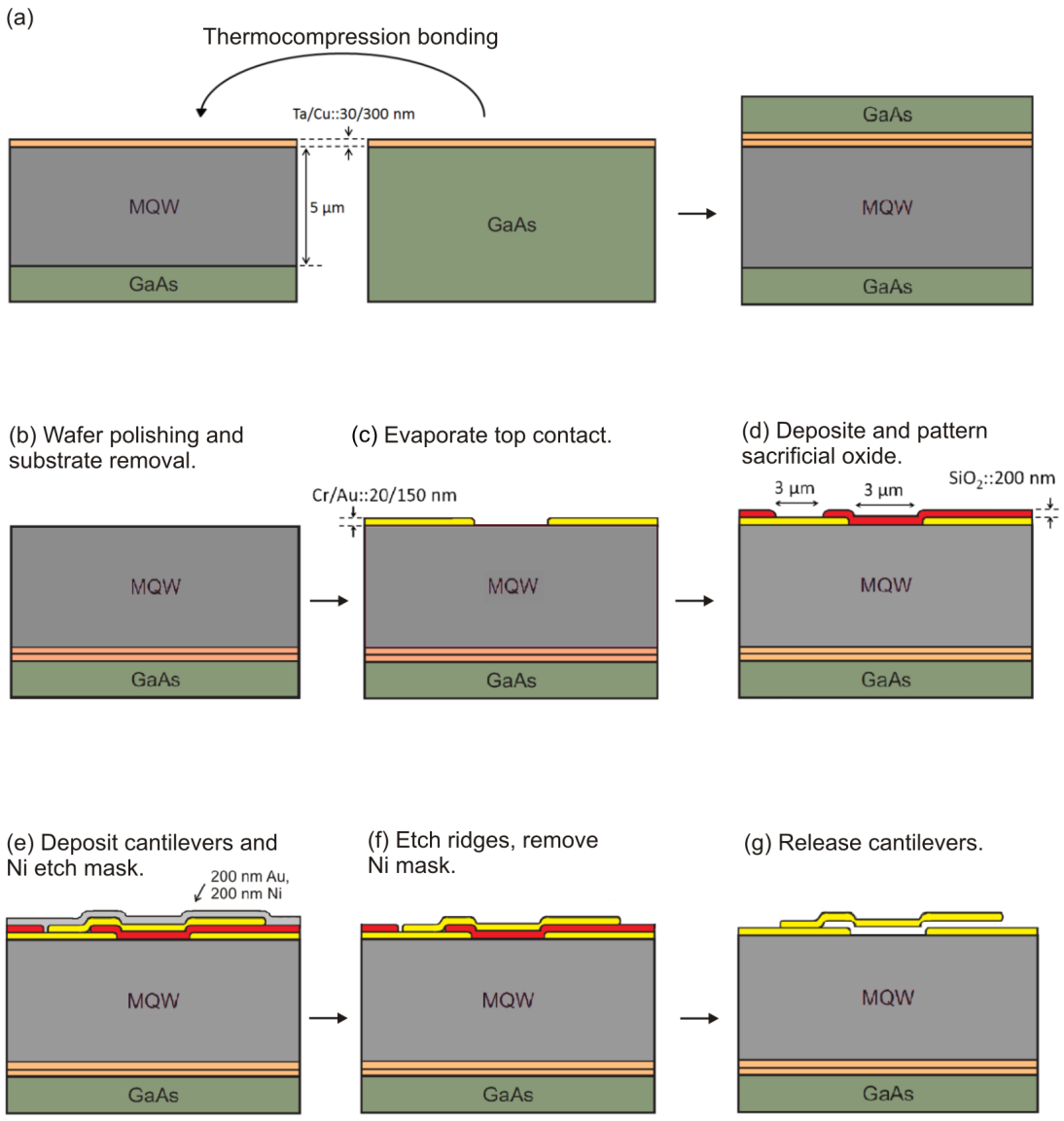

Figure 3.2: Fabrication process for metal-metal metamaterial waveguides. Steps (a)-(c) describe the standard QCL metal-metal waveguide process (with series capacitance) first developed in [49, 50]. Steps (d)-(g) describe the additional fabrication steps for making the cantilever. The Ni and Au layers in step (e) require two separate metal evaporations.

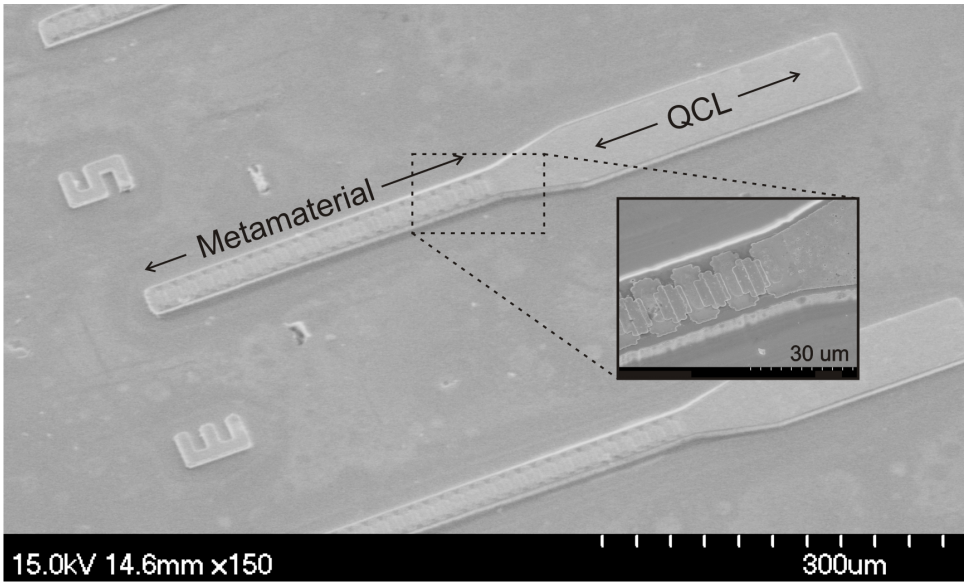

Figure 3.3: SEM of a 50 μm wide THz QCL tapered to a 20 μm wide passive metamaterial section. The metamaterial has a 12 μm period with 3 μm series capacitive gaps in the top metalization and 9 μm cantilever overlays. The cantilevers have not been released, so the metamaterial appears dark (oxide) with light Au patches.

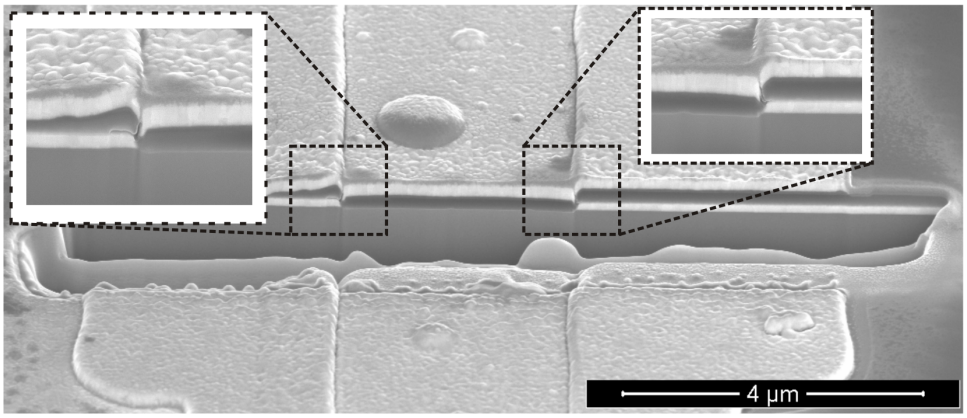

Figure 3.4: SEM of cross-sectional cut of cantilever. Discontinuities in the sacrificial oxide and cantilever metal are observed at points of sidewall coverage.

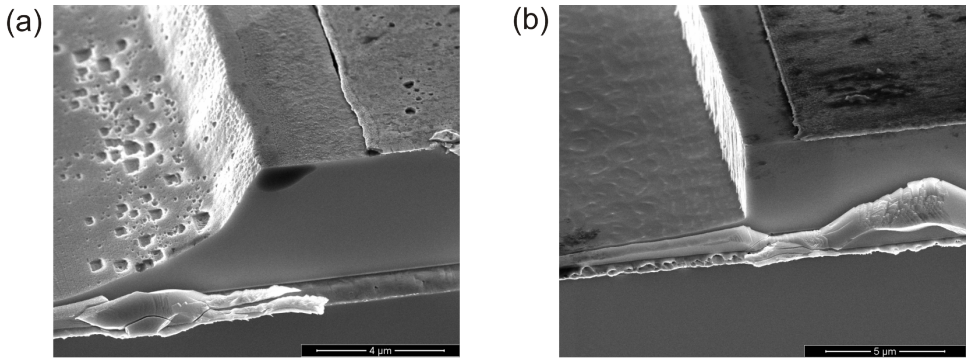

Figure 3.5: (a) SEM of metamaterial QCL ridge. A 300 nm Ni mask was used, causing photoresist peeling during evaporation and sloped sidewalls during the dry etch. (b) SEM of sharp ridge from a standard metal-metal waveguide using a 200 nm Ni mask.

In light of issues concerning the structural integrity of the cantilevers, attempts to demonstrate lasing from unreleased MM metamaterial waveguides were made for the purpose of observing static tuning of different lasers made from the same growth. Should the devices lase, distinct frequency shifts should be observed between the metamaterial devices and the standard MM waveguide devices. There would be no tuning available, but information about losses resulting from the passive metamaterial section could be determined, and available frequency tuning could be determined. Unfortunately, none of the devices have lased (see Chapter 4).

SEM images of the QCL ridges (Figure 3.5(a)) show that one problem could be that the sidewalls from the mesa definition (dry etch, step 13) are sloped rather than vertical. This is a result of stress in the Ni deposition causing the photoresist edges to peel back during the evaporation, allowing thinning amounts of nickle to deposit beyond the intended waveguide etch. During the dry etch, these thin Ni mask extensions are removed progressively, leaving the observed slope and roughness in the etched sidewalls. Sloped sidewalls can result in uneven cur-

rent distribution, decreasing the gain of the structure and the sidewall roughness decreases the sidewall reflectivity and adds loss. Standard, flat MM waveguides that only use a 2000 $\mathring{A}$ Ni mask show sharp, vertical sidewalls (Figure 3.5(b)). A 3000 $\mathring{A}$ Ni mask was used on the metamaterial waveguides to improve sidewall coverage, but the increased stress caused the observed photoresist peeling. The author hopes to resolve this problem by use of a carousel planetary holder during Ni evaporation to improve sidewall coverage and decreased the required thickness of the mask.

3.4 Fixed-fixed beam Fabrication

The long-term goal of achieving competitive levels of frequency tuning depends on the development of the separately biased, free-standing metal overlay design as shown in Figure 2.3(a). A proposed fabrication procedure for free-standing overlays is as follows (see Figure 3.6 for illustrations):

1. Repeat steps 1-8 from above to prepare metal-metal waveguide structure.
2. Evaporate Cr/Au (200:1500 $\mathring{A}$) for the top contact using standard negative contact photolithography.
3. Etch away exposed n-doped contact layer between series capacitive gaps with NH_4OH:H_20_2 (1:100).
4. Evaporate 2000 $\mathring{A}$ Ni for mesa definition. Observe in Figure 3.5(c) that ridges without Cr/Au will be defined to the left and right of the QCL as anchors for the bridges.
5. Dry etch 5 μm ridges into the QCL growth using ICP-RIE with BCl_3 chemistry.
6. Remove remaining Ni mask using Transene Ni etchant.

7. Deposit 250 $\mathring{A}$ SiN to prevent shorting the LH capacitive gaps at pull in and to electrically isolate the anchor QCL ridges from the biased bridge structures.

8. Spin on BCB (benzocyclobutene) polymer and etch back to expose QCL ridges.

9. Evaporate Cr/Au (200/1500 $\mathring{A}$) on the BCB for the bottom electrode of the bridges.

10. Deposit 6000 $\mathring{A}$ $Si0_2$ using PECVD and pattern using positive photolithography and BOE etching.

11. Deposit second oxide layer 4000 $\mathring{A}$ thick and pattern using positive photolithography and BOE etching.

12. Deposit Cr/Au (200/1000 $\mathring{A}$) for bridges.

13. Release bridges with HF vapor etch.

MEMS bridges, like MEMS cantilevers, typically pull in at a height equal to ≈2/3 the initial height of the structure. In order to fully actuate the bridge over the metamaterial waveguide, two sacrificial oxide layers are used so the initial height of the bridge at bias points is larger than the initial height over the metamaterial. In the process described above and illustrated in Figure 3.6, biased portions of the bridge are initially separated by ≈1 μm, while the initial separation between the QCL and the bridge is only 400 nm. This way, the pull-in condition for the bridge should occur after ≈ 330 nm of actuation (rather than $\frac{400}{3} \approx 133$ nm of actuation), allowing for a larger tuning range of the metamaterial.

(a) Evaporate Cr/Au top metal

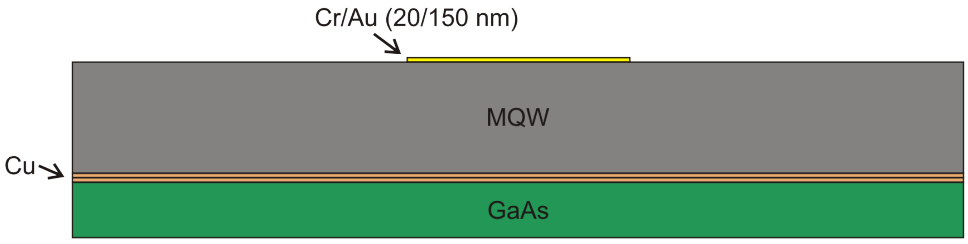

(b) Evaporate Ni mask

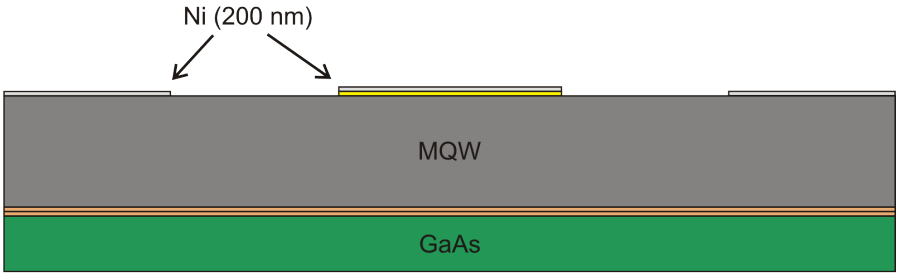

(c) Mesa definition

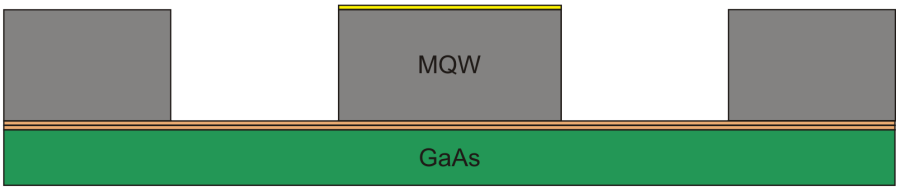

(d) Deposit isolation layer (PECVD)

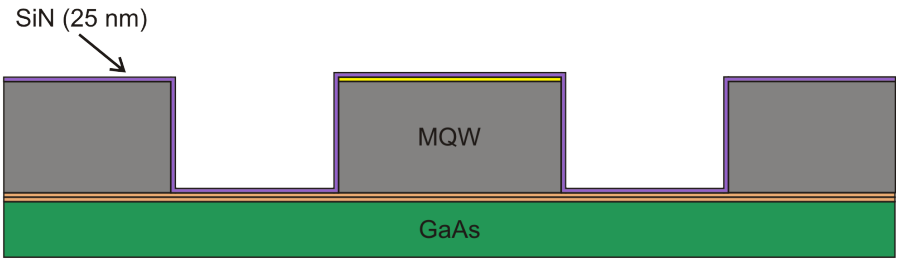

(e) Spin and etch BCB

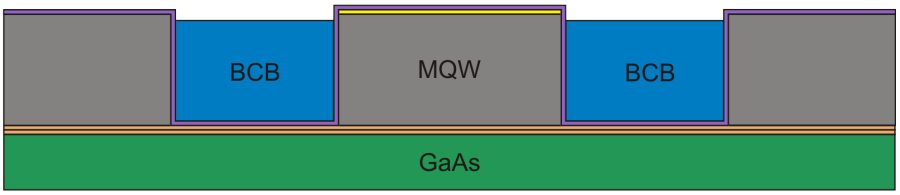

(h) Evaporate cantilever bias electrodes

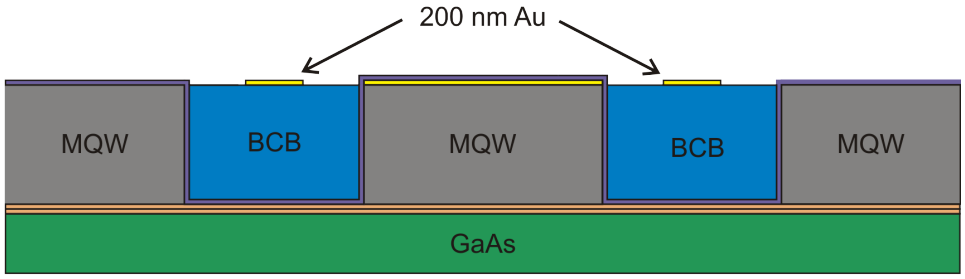

(g) Deposit and etch first sacrificial oxide layer

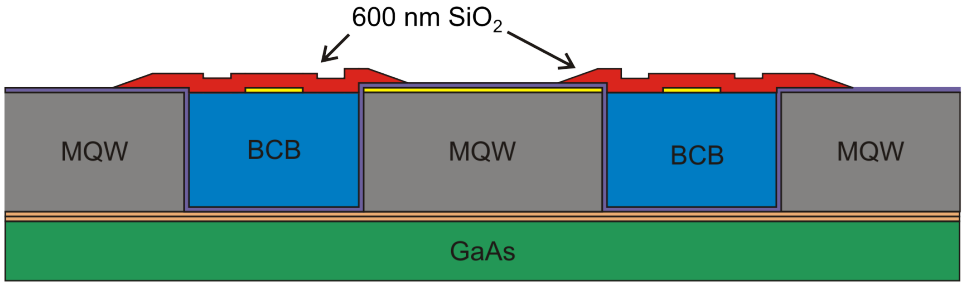

(h) Deposit and etch second sacrificial oxide layer

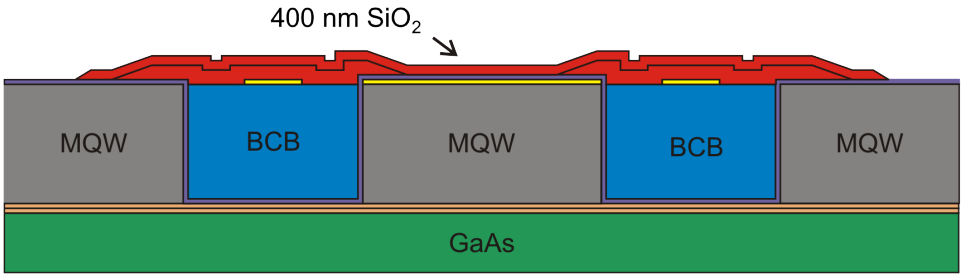

(i) Evaporate Cr/Au for fixed-fixed beams

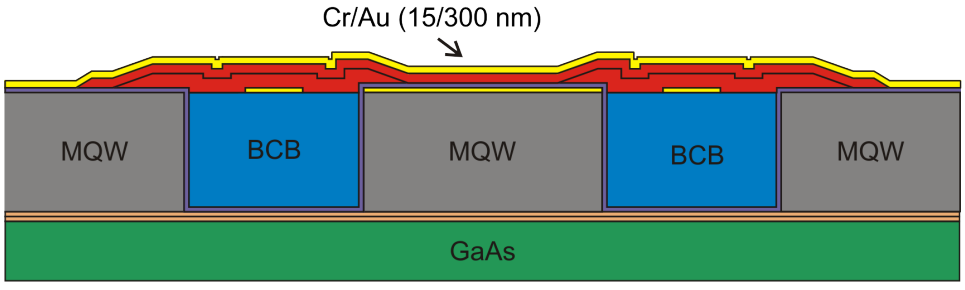

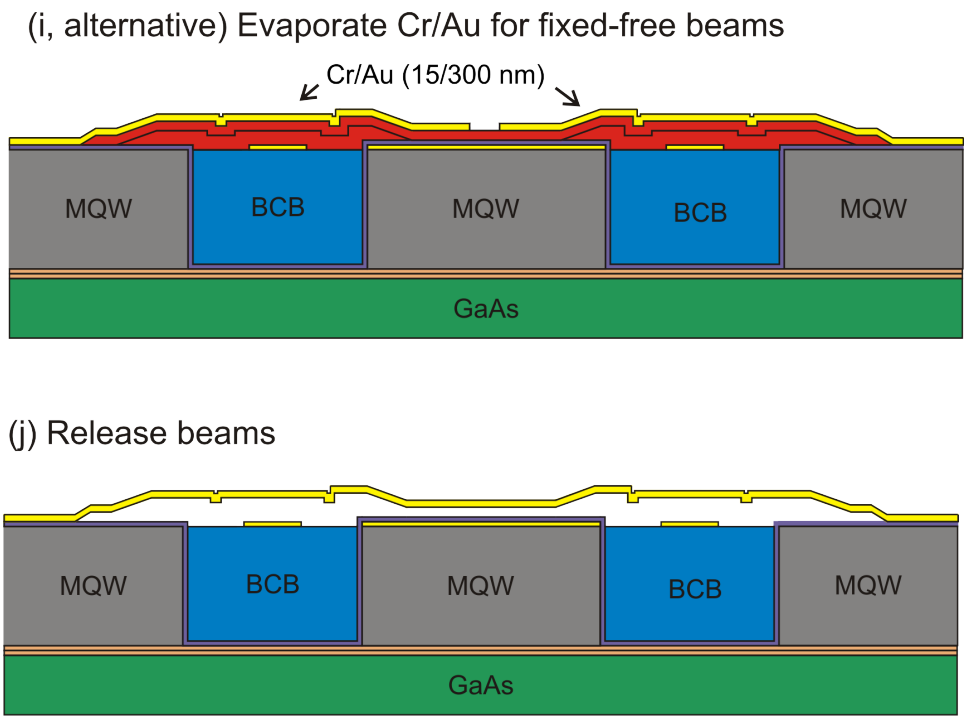

Figure 3.6: Fabrication process for free-standing, separately biased bridges. Same process can be used to fabricate self-actuated cantilever structures such as that in Figure 2.17. Figures show cross-section of structure, rather than the profile of the structure, which was used to illustrate the fabrication process for the self-actuated structure in Figure 3.2. Metal-metal wafer bonding and substrate removal are done first but not shown. Width of BCB trenches and BCB electrodes are not necessarily to scale. See Figure 2.17 for more accurate scales.

CHAPTER 4

Device testing

4.1 Introduction

This project started with four new 4" GaAs wafers with MBE grown QCL heterostructures, each with a different active region design. The wafers were provided by Dr. John Reno of Sandia National Laboratories. Despite the fact that QCL modules can be designed to lase at very specific frequencies, QCL heterostructures are challenging to grow and device characteristics can be very sensitive to the quality of the growth in terms of doping concentration, layer thicknesses, and interface roughness. For these reasons, the new wafers have first been processed into standard MM waveguide lasers so their lasing characteristics (frequency, temperature performance, power output, etc.) can be determined. This also provides control data to compare with metamaterial laser data. In this chapter, I will describe the experimental setup used to collect data, provide some details on the active region designs used, and present the results of tested metal-metal waveguide QCL devices and metamaterial QCL devices.

4.2 Experimental setup

Fabricated devices are cleaved into small pieces ≈1-1.5 mm long and a few millimeters wide. In cases of long MM waveguide lasers, these cleaves provide the facets for the laser cavity. In the case of etched facet devices, cleaves are simply made close to the etched facet. The cleaved pieces are then indium soldered onto

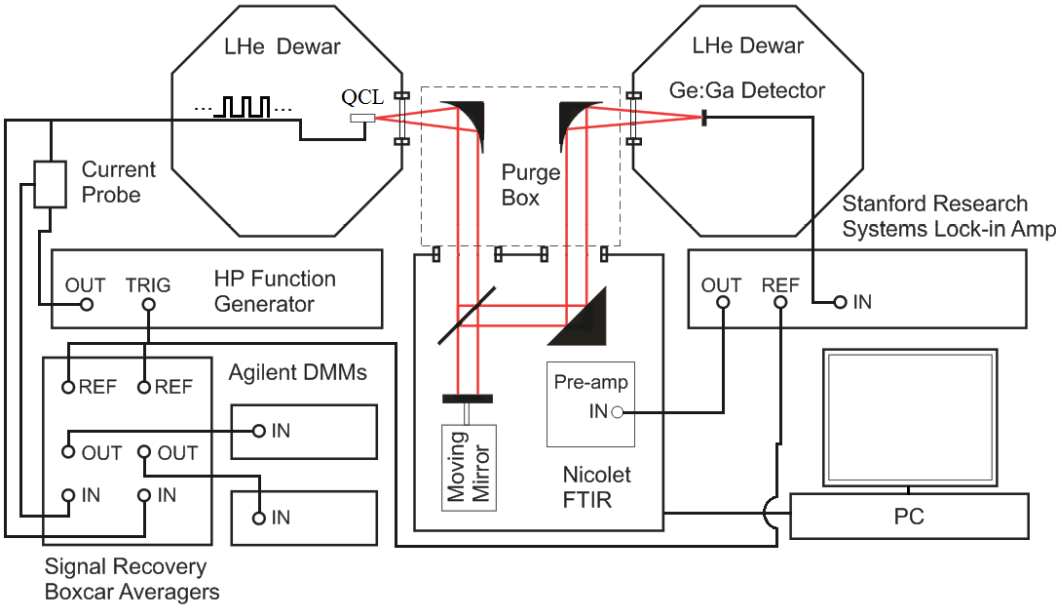

Figure 4.1: Experimental setup for measuring LIV and spectrum data at cold temperature.

a Cu chip carrier and wirebonded to electrically isolated Cu bond pads on the chip carrier. The chip carrier is then attached to a cryostat mount with a Winston cone to collect the divergent beam and the whole structure is mounted to the cold stage of an Infrared (IR) Labs dewar with a polyethylene window to let THz radiation out (see Figure 4.1). THz radiation is detected using an IR-Labs liquid helium cooled gallium-doped germanium (Ge:Ga) photodetector. The detector dewar also uses a polyethylene widow to allow THz radiation in and a Winston cone to focus incoming radiation onto the 1x1 mm detector.

Current, voltage, and light intensity measurements (LIVs) are performed with the device and detector windows face-to-face. Initially, devices are cooled to 77 K and pulsed at 10 KHz and 0.25% duty cycle (250 ns pulses) to avoid device heating. The pulsed signal from the detector is amplified via lock-in detection while the pulsed currents and voltages are probed using a boxcar averager. The

equipment is controlled and data is collected by LabView.

Spectrum measurements are done using a Nicolet fourier transform infrared spectrometer (FTIR). The divergent laser beam is collimated by an off-axis parabolic mirror and directed into the FTIR, which houses a Michelson interferometer with a sweeping mirror on one arm of the interferometer. The time dependent interference pattern is collected by the FTIR using the Ge:Ga detector as the mirror is swept and the data is Fourier transformed to obtain the spectral information. Spectrum measurements are also done in pulsed mode, so the Ge:Ga detector is fed into a lock-in amplifier and the lock-in amplifier's output is fed into the FTIR. This setup is illustrated in Figure 4.3.

4.3 FL series devices

Of the four new wafers, two were four-well resonant-phonon designs and two were three-well resonant-phonon designs. The four-well resonant-phonon designs are based on the FL series of THz QCL devices first described by Williams [49]. The author of this work was not involved in the design selection; the designs were adapted by previous researchers in this lab from designs that have been demonstrated in this and other labs.

4.3.1 Module design

A qualitative understanding of some key active region design parameters is important for proper interpretation of fabrication and testing results. The fundamental operation principles of a four-well resonant-phonon QCL designs were described in Chapter 1. Here, I will review the design of a specific FL design.

Figure 4.1 shows the conduction band diagram, oscillator strengths, anticrossings, and scattering times of an FL series module (FL178C-M7) at its designed bias of 55 mV/module. The FL178C module was designed, tested, and analyzed

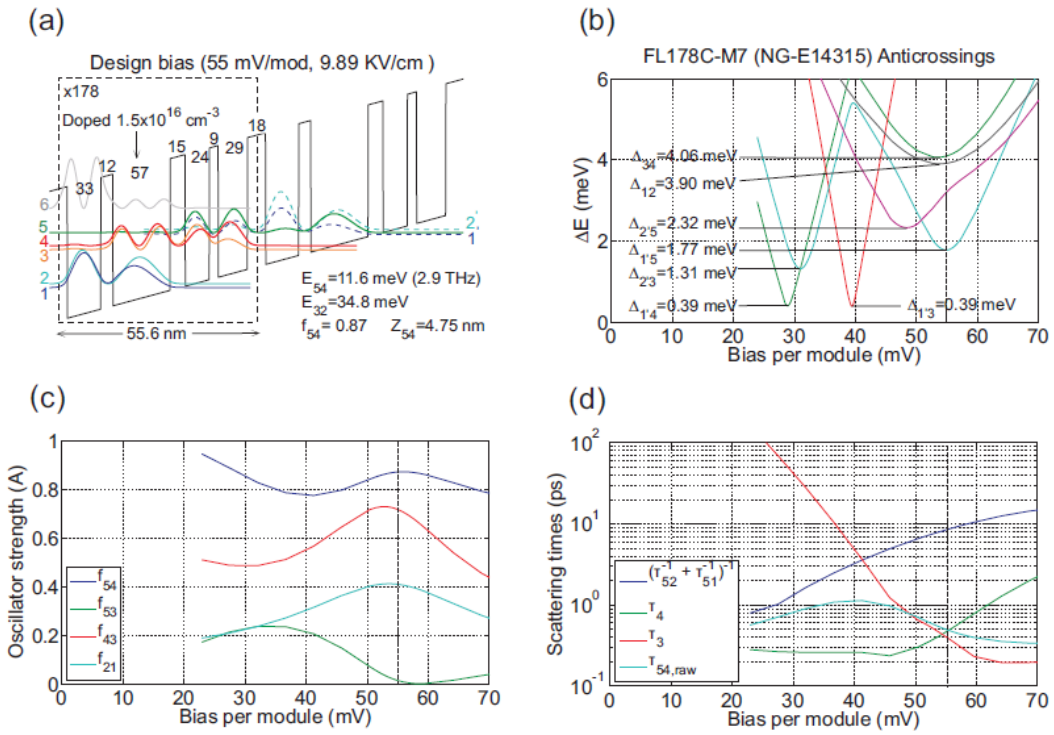

Figure 4.2: (a) Conduction band diagram and electron states for two modules of a four-well resonant-phonon QCL at lasing bias. (b) Anticrossing between states as a function of applied bias. At the designed bias, the anticrossings Δ_{34}, Δ_{12}, and $\Delta_{1'5}$ are all are all at a minimum for strong resonant tunneling. (c) Oscillator strength as a function bias. At design bias, the oscillator strength of the lasing transition ($5 \rightarrow 4$) is at a maximum. (d) Scattering times as a function of bias. At design bias, the scattering time out of the upper lasing state ($\tau_{54,raw}$) is longer than the scattering times of the depopulation and injection states. All figures and data taken from [50].

by Tavallaee [50]. The design uses 178 repeats of the specific FL module, yielding a 10 μm active region designed to lase at 2.9 THz.

At the designed bias, the $5 \rightarrow 4$ lasing transition is separated by E_{54}=11.6 meV (2.9 THz) with a maximum oscillator strength of f=0.87. The $3 \rightarrow 2$ transition is separated by E_{32}=34.8 meV, roughly in tune with the LO-phonon energy E_{LO}=36 meV. Radiative transitions from state 5 into state 4 are selected over state 5 into state 3 by the large $\frac{f_{54}}{f_{53}}$ ratio. The anticrossings Δ_{34}, Δ_{12}, and $\Delta_{1'5}$ are all brought into resonance for tunneling at design bias, and the subthreshold population inversion reaches $(\tau_{52}^{-1} + \tau_{51}^{-1})^{-1}/(\tau_4)$ $\approx$20. Subthreshold parasitic currents occur between the $2' \rightarrow 3$ and $1' \rightarrow 3$ states. At lasing bias, these channels should be suppressed, but can still be a source of leakage.

The two new growths tested by the author were designs FL86Q-M11-T (designed to lase at 2.5 THz) and FL93R-M4-T (designed to lase at 4.3 THz). Both designs are nearly identical to FL178C with exceptions that:

- They are only 5 μm thick (FL86Q and FL93R only use 86 and 93 modules respectively compared to the 178 modules used for FL178C).

- The well and barrier widths are modified to adjust the lasing frequency (FL93R has thinner wells for higher lasing frequency, so it fits more module repeats into the 5 μm active region than FL86Q).

- The new wafers a use highly Si doped (n=5x10^{16} cm^{-3}) 5 nm GaAs layer in the middle of the GaAs collection/injection wells rather than using lower doping ($\approx$1.2x10^{16} cm^{-3}) across the full $\approx$15 nm well. This doping technique was first demonstrated in [116] for improved control over the doping profile of a wafer and has been successfully adopted by several THz QCL research efforts (see Figure 4.7).

- The doping concentration of the top contact layer has been reduced from

5×10^{18} cm^{-3} to 1×10^{18} cm^{-3} and the thickness of the top contact layer has been reduced from 1000 $\mathring{A}$ to 600 $\mathring{A}$. The lower doping should increase contact resistance but decrease free-carrier losses. High temperature QCL operation with no contact layer at all was reported in [34].

4.3.2 FL86Q results

Figure 4.3 shows LIV and spectrum data collected for an etched facet metal-metal QCL and a two-section, metamaterial (unreleased) QCL fabricated from the FL86Q growth. Very weak lasing is observed from the metal-metal QCL and no lasing is observed from the metamaterial QCL device. Two negative differential regions (NDR) are observed on both curves. The second NDR region occurs when the bias becomes too high, causing the states to move out of resonance with tunneling and scattering processes, resulting in decreasing current flow as voltage is increased. This second NDR is typical of QCL IV curves and marks the end of the lasing region. The first NDR observed at the lasing threshold of the metal-metal QCL device, however, is unexpected. Typical QCL IV curves should show a slight decrease in differential conductance ($\frac{dI}{dV}$) as the states come into alignment and the population inversion builds, followed by a sharp spike in differential conductance at lasing threshold associated with the onset of stimulated emission that continues until the onset of NDR (see Figure 4.4). The IV in Figure 4.5, however, shows an early NDR at the threshold bias followed by a general increase in differential resistance until the onset of the second NDR is reached. This behavior suggests poor alignment of the intended states leading to low conduction and low power outputs.

For comparison, and to rule out the possibility of fabrication errors, an old 5 μm thick FL86Q wafer from this lab was processed in parallel with the new FL86Q (grown by Dr. Qi-Sheng at Northrop Grumman in 2009). This old FL86Q growth has the same conduction band structure as the new FL86Q growth, but the old

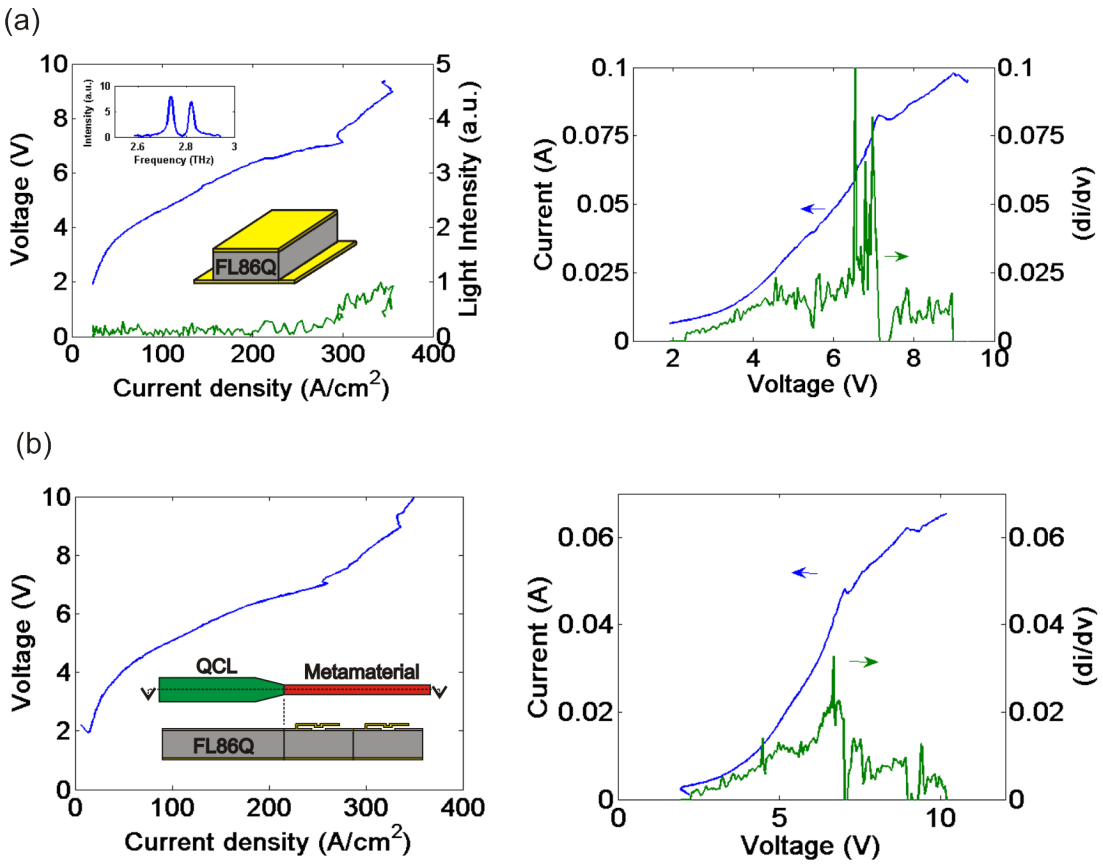

Figure 4.3: New FL86Q growth. LIV, spectrum, and differential conductance data from (a)metal-metal QCL device (550×50 μm etched facet), and (b)metamaterial QCL devices (50×220 μm QCL tapered to 20×250 μm metamaterial). Differential conductance is determined numerically from the IV data. The metal-metal QCL devices show a rough spike in conductance at lasing threshold, while the metamaterial devices don't show any spike and don't lase.

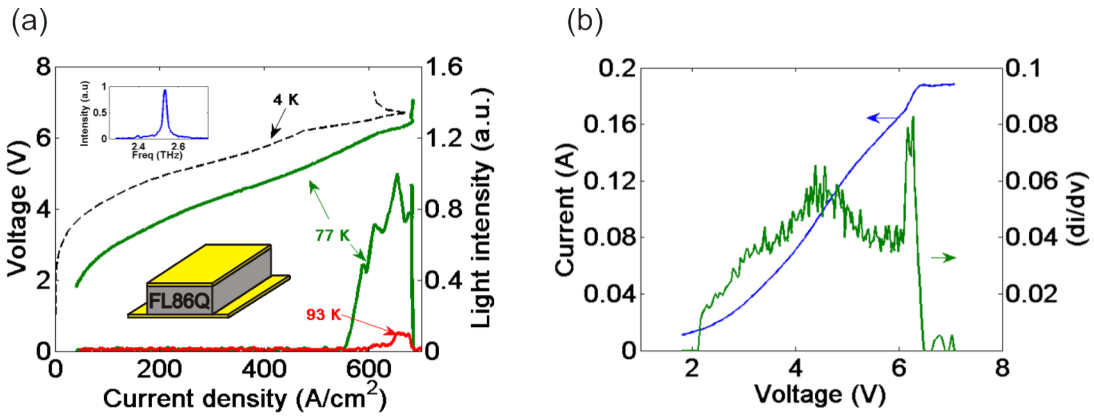

Figure 4.4: Old FL86Q growth. LIV and spectrum data from metal-metal QCL devices (550×50 μm etched facet). Differential conductance shows a characteristic spike at the lasing point with the onset of stimulated emission.

growth uses the same contact layer and active region doping as the FL178C design presented in section 4.3.1 (doping across entire collection/injection well and thicker, higher doped contact layers). This wafer has provided working QCL devices for several publications coming out of this lab [80, 81], but has very little remaining supply. Metal-metal QCL devices from this wafer lased in pulsed mode from heatsink temperatures of 4 K to 93 K and lased in continuous wave (CW) mode at 4 K. The lasing threshold IV is marked by a signature spike in conductance associated with the onset of stimulated emission. At 4 K, the threshold current density is a minimum of ≈475 A/cm^2 and at by 93 K, maximum temperature of operation, the threshold current density has increased to ≈600 A/cm^2. It should be noted that the threshold current densities for this growth are much larger than the threshold current densities in the new growth. This could be due to the larger contact resistance in the new growth due to lower contact layer doping or it could suggest lower doping concentrations in the active region of the new growths than expected. Metamaterial QCL devices have not yet been fabricated with the old FL86Q wafer due to the limited remaining supply.

4.3.3 FL91R results

Data from metal-metal QCL devices and metamaterial devices fabricated from the FL91R growth are presented in Figure 4.7. Neither of these devices lased. Their IV curves don't show a first NDR, but they don't show a spike in conductance either. Again, the current density is notably small.

4.4 OWI series devices

The three-well resonant-phonon designs are based on the OWI series of THz QCL devices published by Fathololoumi, *et al.* [34], which have shown the best temperature performance of any THz QCL to date. The conduction band structure of the Fathololoumi design is shown in Figure 4.7. The module radiates via the $2 \rightarrow 3$ transition and the $1 \rightarrow 3$ transitions. States 3 and 4 are anticrossed, and the $4 \rightarrow 1'$ transition is in resonance with LO-phonon scattering.

Specific designs tested here include OWI112-M6-QW, and OWI113F-T. Both designs are similar to that in Figure 4.7, with the well widths modified to radiate at 2.5 THz and 3.3 THz respectively. Again, the author of this work was not involved in the specifics of the design selection.

4.4.1 OWI112 results

The IV data for a metal-metal QCL made from design OWI112 is presented in Figure 4.8. The IV shows a brief spike in conductance before reaching NDR, but no lasing was measured. The devices did draw notably more current density than the 4-well designs. Metamaterial devices were not fabricated with this growth.

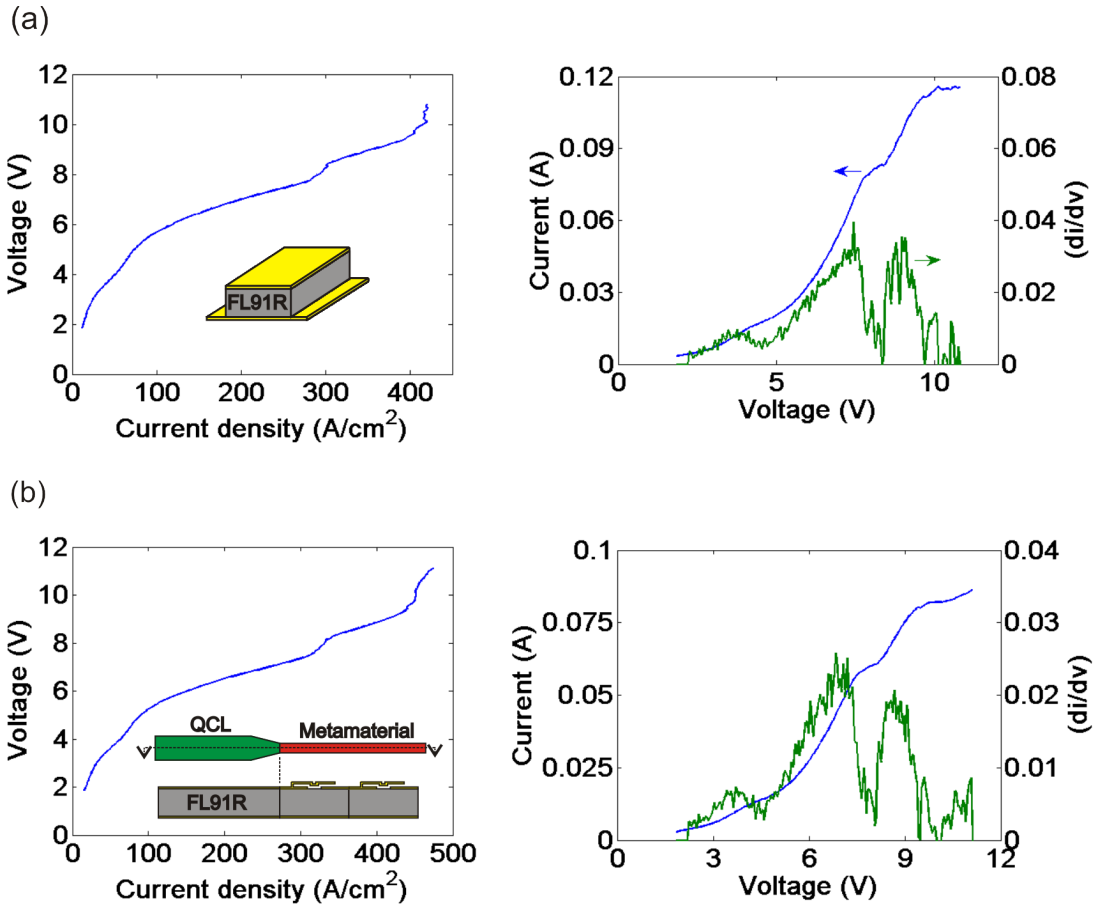

Figure 4.5: FL91R growth. LIV, spectrum, and differential conductance data from (a)metal-metal QCL device (550×50 μm etched facet), and (b)metamaterial QCL devices (50×220 μm QCL tapered to 20×250 μm metamaterial). Neither device shows lasing or a spike in differential conductance.

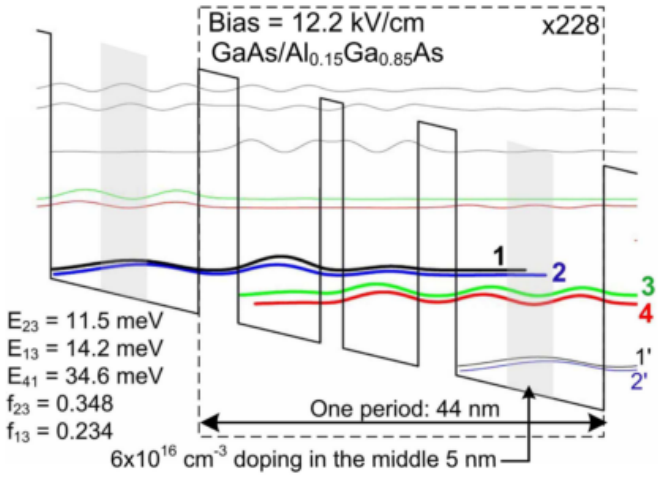

Figure 4.6: Conduction band diagram and electron states for Fathololoumi three--well resonant-phonon design. Lasing occurs through the 2 $\rightarrow$ 3 and 1 $\rightarrow$ 3 transitions. Figure taken from [34].

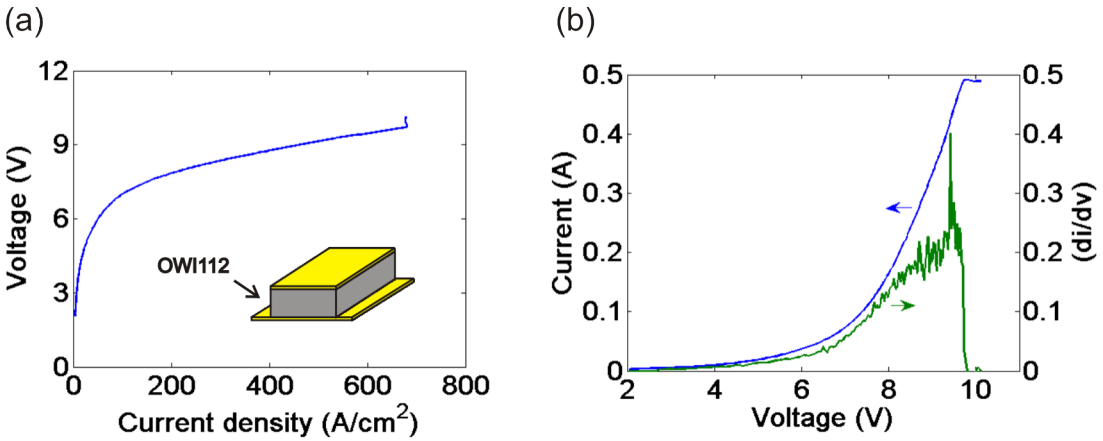

Figure 4.7: OWI112 growth. LIV, spectrum, and differential conductance data from a metal-metal QCL device (550×50 μm etched facet). A very brief, noisy spike is observed at high bias, but no lasing was measured.

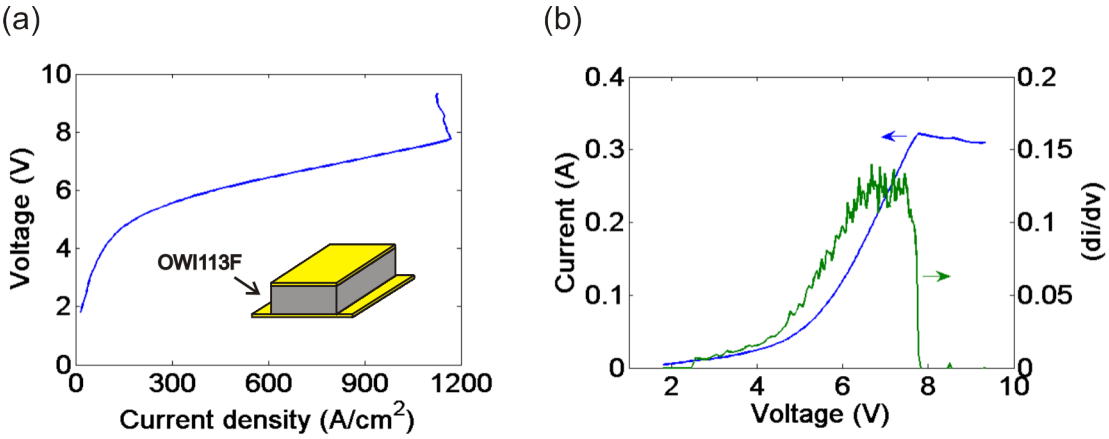

Figure 4.8: OWI113F growth. LIV, spectrum, and differential conductance data from a metal-metal QCL device (550×50 μm etched facet). No signs of lasing, and no spike in conductance.

4.4.2 OWI113F results

The IV data for a metal-metal QCL made from design OWI113F is presented in Figure 4.9. The device did not lase or show any spike in differential conductance. Similar to OWI112, the OWI113 device also drew notably more current density than either of the 4-well designs. Metamaterial QCL devices were fabricated using OWI113F, but they did not lase or show any additional characteristics in their IV curves.

4.4.3 Fathololoumi growth results

Lastly, to rule out problems with the fabrication process, the author processed metal-metal QCL devices using a piece of growth provided through collaboration with Dr. Fathololoumi. The growth was originally done by the National Research Council of Canada for the work published in [?] and uses the OWI design shown in Figure 4.6. IV and spectrum data is presented in Figure 4.9. Device lasing was measured in pulsed mode from heatsink temperatures of 77 K to 175 K with

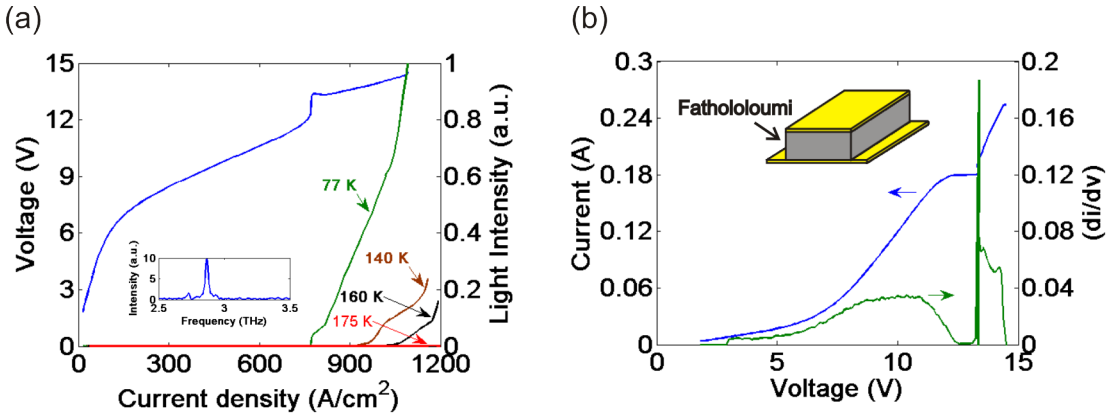

Figure 4.9: Fathololoumi *et al*. growth (wafer number V774) [34]. LIV, spectrum, and differential conductance data from metal-metal QCL devices (550×50 μm etched facet). Lasing is observed up to 175 K.

threshold current density varying from ≈770 A/cm^2 to 1000 A/cm^2. These are similar results to those originally observed and published by Fathololoumi, *et al*.

4.5 Summary and conclusions

Testing results for four new QCL growth have been presented along with results from old growths of the similar designs. Very weak lasing was observed from metal-metal QCL devices using one new growth (FL86Q), while lasing from metal-metal waveguides from the other three growths was not observed. Metamaterial QCL devices, were fabricated with the new growths and did not lase either. Metal-metal QCL devices fabricated from the old growths did lase, suggesting that there is either a problem with the new growths, or a problem with fabrication of QCL devices using the new growths. It's noted that the new growths have two $Al_{0.55}Ga_{0.45}As$ etchstop layers sandwiching a 100 nm GaAs layer (see Figure 3.1). This results in additional etch steps in processing the new growths (steps 7 and 8 in section 3.2) compared to the old growths which only used a single

$Al_{0.55}Ga_{0.45}As$ etchstop layer on top of the doped contact layer. If the additional etchstop layers on the new growths are not properly removed, there could be large contact resistances resulting in the small current densities drawn by the new growths.

Given the observed issues with processing the new wafer growths, no conclusive comments can made on the success or failure of metamaterial based QCL devices, though visible issues with the fabrication process were discussed in Chapter 3. As a next step, metamaterial QCL devices will be fabricated using what remains of the old growths that have lased while we're in the process of obtaining new wafers from our collaboration with Sandia National Labs.

CHAPTER 5

Conclusions and future work

The purpose of the work was to study and design tunable THz transmission line metamaterials using MEMS cantilevers and apply such designs to the development of a tunable THz quatum cascade laser. Two tuning approaches have been investigated using transmission line theory and FEM simulations: self-actuation of cantilevers using the THz power in the metamaterial waveguide, and separate actuation using additional electrodes. Self-actuated designs are easier to fabricate, but show significantly less tuning (≈1-2% tuning of self actuated devices compared to upwards of ≈30% tuning of separately actuated structure) and the THz power required for actuation may be difficult to achieve in typical THz QCL devices. Additionally, both fundamental TM_{00} mode designs and higher order TM_{01} designs were investigated. TM_{00} and TM_{01} designs show similar tuning capabilities, but TM_{00} designs cannot be electrically biased and thus require the development of a two section laser where the metamaterial is fed by a standard metal-metal THz QCL. Such two section resonant cavities shows even less tuning and require more THz power to tune. Furthermore, the inability to bias the top metalization of the TM_{00} designs could cause cantilever pull-in to occur earlier, substantially decrease the actuation range and tuning capabilities. TM_{01} designs, on the other hand, can be electrically biased, allowing for the development of purely metamaterial QCL designs that show significantly more tuning and have lower losses.

Fabrication procedures for both self-actuated and separately biased structures

have been proposed. An attempt has been made to fabricate two-section, 12 μm period, self-actuated THz QCL devices. None of these devices have worked. SEM images of fabricated devices have revealed discontinuities in the cantilevers, making them unable to stand after removing the sacrificial layer. However, regardless of the quality of the cantilevers, fabrication of standard metal-metal waveguide THz QCL devices reveals that most of the QCL growths used do not lase, which is likely related to problems during their growth at Sandia National Laboratories (not grown by the author). This is unusual as THz QCL devices have been demonstrated time and time again in the past 10-15 years, have been demonstrated previously in this lab, and were demonstrated in this work using pieces of old growths that are in very limited supply. The failure of the growths should be considered unrelated to the potential success of the designs presented in this work.

While we're in the process of obtaining growths that lase, work needs to be done on the development of more structurally sound MEMS. Recipe modifications in the deposition of the sacrificial oxide layer need to be investigated, and it may be necessary to consider a different sacrificial oxide layer all together (such as photoresist). Lastly, different techniques for depositing the cantilever metal need to be investigated including evaporation using a carousel planetary wafer holder and sputtering.

References

[1] P. Siegel, "Terahertz technology," *IEEE Transactions on Microwave Theory and Techniques,* vol. 50, pp. 910-928, 2002.

[2] J. Wiltse, "History of millimeter and submillimeter waves," *IEEE Transactions on Microwave THeory and Technology,* vol. 32, pp. 1118-1127, 1984.

[3] G. Chattopadhyay, "Technology, capabilities, and performance of low power terahertz sources," *IEEE Transactions on Terahertz Science and Technology,* vol. 1, pp. 33-53, 2011.

[4] F. C. De Lucia, "Spectroscopy in the Terahertz Spectral Region," *Sensing with terahertz radiation* pp. 39-115. Springer, Berlin, 2003.

[5] B. Deng, C. Domier, D. Lee, N. Luhmann, E. Mazzucato, "THz techniques in plasma diagnostics," *Microwave Symposium Digest, 2002 IEEE MTT-S International,* vol. 3, pp. 1587-1590, 2002.

[6] H. Hubers, S. Pavlov, H. Richter, A. Semenov, L. Mahler, A. Tredicucci, H. Beere, D. Ritchie, "High-resolution gas phase spectroscopy with a distributed feedback terahertz quantum cascade laser," *Applied Physics Letters,* vol. 89, 061115, 2006.

[7] T. Phillips and J. Keene, "Submillimeter astronomy (heterodyne spectroscopy)," *Proceedings of the IEEE,* vol. 80, pp. 1662-1678, 1992.

[8] Herschel's instruments. [Online]. European Space Agency, available: http://herschel.cf.ac.uk/mission/instruments.

[9] H. Picketta "THz spectroscopy of the atmosphere," Jet Propulsion Laboratory, May 1998.

[10] The stratospheric terahertz observatory. [Online]. Available: http://soral.as.arizona.edu/STO/Welcome.html.

[11] Stratospheric observatory for infrared astronomy. [Online]. Available: http://www.sofia.usra.edu/.

[12] D. Leisawitz, W. Danchi, M. DiPirro, L. Feinberg, D. Gezari, M. Hagopian, W. Langer, J. Mather, S. Moseley, M. Shao, R. Silverberg, J. Staguhn, M. Swain, H. Yorke, and X. Zhang, "Scientific motivation and technology requirements for the SPIRT and SPECS far-infrared/submillimeter space interferometers," *UV, Optical, and IR Space Telescopes and Instrumentation* pp. 36-46, 2000.

[13] D. Woolard, R. Brown, M. Pepper, and M. Kemp, "Terahertz frequency sensing and imaging: a time of reckoning and future applications?" *Proceeding of the IEEE,* vol. 93, pp. 1722-1743, 2005.

[14] W. Chan, J. Deibel, D. Mittleman, "Imaging with terahertz radiation," *Reports on Progress in Physics,* vol. 70, pp. 1325-1379, 2007.

[15] Optical frequency combs, terahertz systems, femptosecond fiber lasers. [Online]. MenloSystems. Available: http://www.menlosystems.com/products/.

[16] Saf-T-Check ADS. [Online]. Advanced Photonex, Inc. Available: http://advancedphotonix.com/thzsolutions/products/saf-t-chek/.

[17] Micro-Z. [Online]. Zomega. Available: http://dl.z-thz.com/brochures/microz1401lr.pdf.

[18] J. Damaro, V. Tamosiunas, G. Fasching, J. Kroll, K. Uterrainer, M. Beck, M. Giovannini, J. Faist, C. Kremser, and P. Debbage, "Imaging with a terahertz quantum cascade laser," *Optics Express* vol. 12, pp. 1879-1884, 2004.

[19] A. Lee, and Q. Hu, "Real-time, continuous-wave terahertz imaging by use of a microbolometer focal-plane array," *Optics Letters* vol. 30, no. 19, pp. 2563, 2005.

[20] M. Tonouchi, "Cutting-edge terahertz technology," *Nature Photonics* vol. 1, pp. 97-105.

[21] H. Ward, E. Schlecht, G. Chattopadhyay, A. Maestrini, J. Gill, F. Maiwald, H. Javadi, and I. Mehdi, "Capability of THz sources based on Schottky diode frequency multiplier chains," *2004 IEEE MTT-S International Microwave Symposium Digest,* vol. 3, pp. 1587-1590, 2004.

[22] C. Berry, M. Hashemi, S. Preu, H. Lu, A. Gossard, and M. Jarrahi, "Plasmonics enhanced photomixing for generating quasi-continuous-wave frequency-tunable terahertz radiation," *Optics Letters,* vol. 39, pp. 4522-4524, 2014.

[23] W. Shi, Y. Ding, N. Fernelius, K. Vodopyanow, "Efficient, tunable, and coherent 0.18-5.27 THz source based on GaSe crystal," *Optics Letters,* vol. 27, pp. 1454, 2002.

[24] K. Kawase, J. Shikata, K. Imai, and H. Ito, "Transform-limited, narrow-linewidth, terahertz-wave parametric generator," *Applied Physics Letters,* vol. 78, pp. 2819, 2001.

[25] M. Belkin, F. Capasso, A. Belyanin, D. Sivco, A. Cho, D. oakley, C. Vineis, and G. Turner, "Terahertz quantum-cascade-laser source based on intracavity difference-frequency generation," *Nature Photonics,* vol. 1, pp. 288-292, 2007.

[26] Q. Lu, N. Bandyopadhyay, S. Silvken, Y. Bai, and M. Razeghi, "Continuous operation of a monolithic semiconductor terahertz source at room temperature," *Applied Physics Letters,* vol. 104, no. 22, pp. 221105, 2014.

[27] Y. Jiang, K. Vijayraghavan, S. Jung, F. Demmerie, G. Boehm, M. Amann, and M. Belkin, "External cavity terahertz quantum cascade laser sources based on intra-cavity frequency mixing with 1.2-5.9 THz tuning range," *Journal of Optics,* vol. 16, no. 9, pp. 094002, 2014.

[28] R. Kohler, A. Tredicucci, F. Beltram, H. Beere, E. Linfield, A. Davies, D. Ritchie, R. Iotti, and F. Rossi, "Terahertz semiconductor-heterostructure laser," *Nature,* vol. 417, pp. 156-159, 2002.

[29] B. Williams, H. Callebaut, S. Kumar, and Q. Hu, "3.4-THz quantum cascade laser based on longitudinal-optical-phonon scattering for depopulation," *Applied Physics Letters,* vol. 82, pp. 1015, 2003.

[30] M. Rochat, L. Ajili, H. Willenberg, J. Faist, H. Beere, G. Davies, E. Linfield, D. Ritchie, "Low-threshold terahertz quantum-cascade lasers," *Applied Physics Letters,* vol. 81, pp. 1381, 2002.

[31] B. Williams, S. Kumar, Q. Hu, and J. Reno, "High-power terahertz quantum-cascade lasers," *Electronics Letters,* vol. 42, pp. 89, 2006.

[32] L. Li, L. Chen, J. Zhu, J. Freeman, P. Dean, A. Valavanis, A. Davies, and E. Linfield, "Terahertz quantum cascade lasers with ¿1 W output powers," *Electronics Letters,* vol. 50, no. 4, pp. 309-311, 2014.

[33] M. Wienold, B. Roben, L. Schrottke, R. Sharma, A. Tahraoui, K. Biermann, and H. T. Grahn, "High-temperature, continuous-wave operation of terahertz quantum-cascade lasers with metal-metal waveguides and third-order distributed feedback," *Optics Express,* vol. 22, pp. 3334-3348, 2014.

[34] S. Fathololoumi, E. Dupont, C. W. I. Chan, Z. R. Wasilewski, S. R. Laframboise, D. Ban, A. Matyas, C. Jirauschek, Q. Hu, and H. C. Liu, "Terahertz quantum cascade lasers operating up to 200 K with optimized oscillator strength and improved injection tunneling," *Optics express,* vol. 20, pp. 3866-3876, 2012.

[35] M. Amanti, M. Fischer, G. Scalari, M. Beck, and J. Faist, "Low-divergence of single-mode terahertz quantum cascade laser," *Nature Photonics,* vol. 3, pp. 586-590, 2009.

[36] A. Tavallaee, P. Hon, Q. Chen, and T. Itoh, "Active terahertz quantum-cascade composite right/left-handed metamaterial," *Applied Physics Letters,* vol. 102, pp. 021103, 2013.

[37] Ricor products comparison table. [Online]. Ricor Cryogenic Vacuum Systems, available: http://www.ricor.com/products/comparison-table/.

[38] E. Zibik, T. Grange, B. Carpenter, N. Porter, R. Fereira, G. Bastard, D. Stehr, S. Winnerl, M. Helm, H. Liu, M. Skolnick, and L. Wilson, "Long lifetimes of quantum-dot intersublevel transitions in the terahertz range," *Nature Materials* vol. 8, no. 10, pp. 803-807, 2009.

[39] Y. Ren, J. N. Hovenier, R. Higgins, J. R. Gao, T. M. Klapwijk, S. C. Shi, A. Bell, B. Klein, B. S. Williams, S. Kumar, Q. Hu, and J. Reno, "Terahertz heterodyne spectrometer using a quantum cascade laser," *Applied Physics Letters,* vol. 97, pp. 161105, 2010.

[40] J. Kloostermann, D. Hayton, Y. Ren, T. Kao, J. Hovenier, J. Gao, T. Klapwijk, Q. Hu, C. Walker, J. Reno, "Hot electrom bolometer heterodyne receiver with a 4.7-THz quantum cascade laser as a local oscillator," *Apllied Physics Letters* vol. 102, pp. 011123, 2013.

[41] A. Lee, B. Williams, S. Kumar, Q. Hu, and J. Reno, "Real-time imaging using a 4.3-THz quantum cascade laser and a 320×240 microbolometer focal-plane array," *Laser and Electro-Optics, and Quantum Electroncs and Laser Science Conference,* vol. 18, pp. 1415-1417, 2006.

[42] J. Xu, J. Hensley, D. Fenner, R. Green, L. Mahler, A. Tredicucci, M. Allen, F. Beltram, H. Beere, and D. Ritchie, "Tunable terahertz quantum cascade lasers with an external cavity," *Applied Physics Letters,* vol. 91, no. 12, pp. 121104, 2007.

[43] A. Lee, B. Williams, S. Kumar, Q. Hu, and J. Reno, "Tunable terahertz quantum cascade lasers with external gratings," *Optics Letters,* vol. 35, no. 7, pp. 910-912, 2010.

[44] Y. Yao, T. Tsai, X. Wang, G. Wysocki, and C. Gmachl, "Broadband quantum cascade laser based on strongly-coupled transitions with an external cavity tuning range over 340 cm^{-1}," *CLEO:2012 - Laser Applications to Photonic Apllications* pp. 1-2, 2012.

[45] Q. Qin, B. Williams, S. Kumar, J. Reno, and Q. Hu, "Tuning a terahertz wire laser," *Nature Photonics,* vol. 3, no. 12, pp. 732-737, 2009.

[46] Q. Qin, J. Reno, and Q. Hu, "MEMS-based tunable terahertz wire-laser over 330 GHz," *Optics letters,* vol. 36, pp. 692-694.

[47] N. Han, A. Geofroy, D. Burghoff, C. Chan, A. Lee, J. Reno, and Q. Hu "Broadband all-electronically tunable MEMS terahertz quantum cascade laser," *Optics Letters,* vol. 39, no. 12, pp. 3480-3, 2014.

[48] J. Water, "An overview of the EOS MLS experiment," Jet Propulsion Laboratory, 1999.

[49] B. S. Williams, "Terahertz quantum-cascade lasers," Ph.D. dissertation, Dept. of Electrical Engineering and Computer Science, MIT, Cambridge, MA, 2003.

[50] A. Tavallaee, "Terahertz quantum-cascade transmission-line metamaterials," Ph.D. dissertation, Dept. of Electrical Engineering, UCLA, Los Angeles, CA, 2012.

[51] S. Kumar, "Development of terahertz quantum-cascade lasers," Ph.D. dissertation, Dept. of Electrical Engineering and Computer Science, MIT, Cambridge, MA, 2007.

[52] C. Deutsch, M. Krall, M. Brandstetter, H. Detz, A. Andrews, P. Klang, W. Schrenk, G. Strasser, and K. Unterrainer, "High performance InGaAs/GaAsSb terahertz quantum cascade lasers operating up to 142 K," *Applied Physics Letters,* vol. 101, no. 21, pp. 211117, 2012.

[53] K. Fujita, M. Yamanishi, S. Furuta, K. Tanaka, T. Edamura, T. Kubis, and G. Klimeck, "Indirectly pumped 3.7 THz InGaAs/InAlAs quantum-cascade lasers grown by metal-organic vapor-phase epitaxy," *Optics Express,* vol. 20, no. 18, pp. 20647-58, 2012.

[54] S. Kohen, B. Williams, and Q. Hu, "Electromagnetic modeling of terahertz quantum cascade laser waveguides and resonators," *Journal of Applied Physics,* vol. 97, no. 5, pp. 053106, 2005.

[55] N. W. Ashcroft and N. D. Mermin, *Solid State Physics,* Saunders college, 1976.

[56] S. Ramakrishna, "Physics of negative refractive index materials," *Reports on Progress in Physics,* vol. 68, no. 2, pp. 449-521, 2005.

[57] Y. Liu and X. Zhang, "Metamaterials: a new frontier of science and technology," *Chemical Society Reviews,* vol. 40, pp. 2494-2507, 2011.

[58] V. Veselago, "The electrodynamics of substances with simultaneously negative values of ϵ and μ," *Soviet Physics Uspekhi,* vol. 10, no. 4, pp. 509-514, 1968.

[59] D. Smith, W. Padilla, D. Vier, S. Nemat-Nasser, and S. Schultz, "Composite medium with simultaneously negative permeability and permittivity," *Physical Review Letters,* vol. 84, no. 18, pp. 4184-4187.

[60] R. Shelby, D. Smith, and S. Schultz, "Experimental verification of negative index of refraction," *Science,* vol. 292, pp. 77-79, 2001.

[61] J. Pendry, A. Holden, W. Stewart, and I. Youngs, "Extremely Low Frequency Plasmons in Metallic Mesostructures," *Physical Review Letters,* vol. 76, no. 35, pp. 4773-4776, 1996.

[62] J. Pendry, A. Holden, W. Stewart, "Magnetism from conductors and enhanced nonlinear phenomena," *IEEE Transactions on Microwave Theory and Techniques,* vol. 47, pp. 2075-2084, 1999.

[63] H. Tao, W. Padilla, X. Zhang, and R. Averitt, "Recent progress in electromagnetic metamaterial devices for terahertz applications," *IEEE Journal of Selected Topics in Quantum Electronics* vol. 17, pp. 92-101, 2011.

[64] N. Liu, H. Guo, L. Fu, S. Kaiser, H. Schweizer, and H. Giessen, "Three-dimensional photonic metamaterials at optical frequencies," *Nature materials,* vol. 7, pp. 31-37, 2008.

[65] J. Ou, E. Plum, J. Zhang, and N. Zheludev, "An electromechanically reconfigurable plasmonic metamaterial operating in the near-infrared," *Nature Nanotechnology* vol. 8, pp. 252-255, 2013.

[66] N. Zheludev and Y. Kivshar, "From metamaterials to metadevices," *Nature materials,* vol. 11, no. 11, pp. 917-924, 2012.

[67] H. Tao, A. Strikwerda, K. Fan, W. Padilla, X. Zhang, and R. Averitt, "Reconfigurable terahertz metamaterials," *Physical Review Letters,* vol. 103, no. 14, pp. 147401, 2009.

[68] W. Zhu, A. Liu, T. Bourouina, D. Tsai, J. Teng, X. Zhang, G. Lo, D. Kwong, and N. Zheludev, "Microelectromechanical Maltese-cross metamaterial with tunable terahertz anisotropy," *Nature Communications,* vol. 3, pp. 1274, 2012.

[69] M. Unlu, M. R. Hashemi, C. W. Berry, S. Li, S.-H. Yang, and M. Jarrahi, "Switchable scattering meta-surfaces for broadband terahertz modulation," *Nature Scientific Reports,* vol. 4, 5708, July 2014.

[70] H. Chen, W. Padilla, M. Cich, A. Azad, R. Averitt, and A. Taylor, "A metamaterial sold-state terahertz phase modulator," *Nature Photonics* vol. 3, no. 3, pp. 148-151, 2009.

[71] R. Yan, B. Sensale-Rodriguez, L. Liu, D. Jena, and H. Xing, "A new class of electrically tunable metamaterial terahertz modulators," *Optics express,* vol. 20, no. 27, pp. 28664-71, 2012.

[72] D. Dietze, A. Benz, G. Strasser, K. Unterrainer, and J. Darmo, "Terahertz meta-atoms coupled to a quantum well intersubband transition," *Optics Express,* vol. 19, no. 14, pp. 13700-6, 2011.

[73] D. Smith, J. Pendry, and M. Wiltshire, "Metamaterials and negative refractive index," *Science,* vol. 305, pp. 788-792, 2004.

[74] C. Caloz and T. Itoh, "Application of the transmission line theory of left-handed (LH) materials to the realization of a microstrip "LH line"," *IEEE Antennas and Propagation Society International Symposium,* vol. 2, pp. 412-415, 2002.

[75] A. Oliner, "A planar negative-refractive-index medium without resonant elements," *IEEE MTT-S International Microwave Symposium Digest,* vol. 1, pp. 191-194, 2003.

[76] A. Iyer and G. Elftheriades, "Negative refractive index metamaterials supporting 2-D waves," *2002 IEEE MTT-S International Microwave Symposium Digest,* vol. 2, pp. 1067-1070.

[77] C. Caloz, A. Sanada, and T. Itoh, "A novel composite right-/left-handed coupled-line directional coupler with arbitrary coupling level and broad bandwidth," *IEEE Transactions on Microwave Theory and Techniques* vol. 52, no. 3, pp. 980-992, 2004.

[78] A. Genc and R. Baktur, "Dual- and triple-band Wilikinson power dividers based on composite right- and left-handed transmission lines," *IEEE Transactions on Components, Packaging, and Manufacturing Technology,* vol. 1, no. 3, pp. 327-334, 2011.

[79] K. Staszek, J. Sorocki, P. Kaminski, K. Wineza, and S. Gruszezynski, "A broadband 3 dB tandem coupler utilizing right/left handed transmission line sections," *IEEE Microwave and Wireless Components Letters,* vol. 24, no. 4, pp. 236-238, 2014.

[80] A. A. Tavallaee, B. S. Williams, P. W. C. Hon, T. Itoh, and Q. S. Chen, "Terahertz quantum-cascade laser with active leaky-wave antenna," *Appl. Phys. Lett.,* vol. 99, no. 14, p. 141115, 2011.

[81] A. A. Tavallaee, P. W. C. Hon, Q.-S. Chen, T. Itoh, and B. S. Williams, "Active terahertz quantum-cascade composite right/left-handed metamaterial," *Appl. Phys. Lett.* vol. 102 021103, Jan. 2013.

[82] Z. Liu, P. Hon, A. Tavallaee, T. Itoh, and B. Williams, "Terahertz composite right-left handed transmission-line metamaterial waveguides," *Applied Physics Letters,* vol. 100, no. 7, pp. 071101, 2012.

[83] S. Sanders, "Wavelength-agile lasers," *Optics and Photonics News,* vol. 16, no. 5, pp. 36-41, 2005.

[84] D. Brown, M. Flynn, L. O'Faolain, and T. Kroauss, "Low tuning current semiconductor coupled-cavity lasers incorporating Bragg reflectors," *IEEE Photonics Technology Letters,* vol. 17, no. 11, pp. 2262-2264, 2005.

[85] S. Kumar, B. Williams, Q. Qin, A. Lee, and Q. Hu, "Surface-emitting distributed feedback terahertz quantum-cascade lasers in metal-metal waveguides," *Optics Express,* vol. 15, no. 1, pp. 113-128.

[86] H. Zhang, L. Dunbar, G. Salari, R. Houdre, and J. Faist, "Terahertz phontonic crystal quantum cascade lasers," *Optics Express,* vol. 15, no. 25, pp. 16818-27, 2007.

[87] H. Nasim, Y. Jamil, "Recent advancements in spectroscopy using tunable diode lasers," *Laser Physics Letters* vol.10, no. 4, pp. 043001, 2013.

[88] Y. Sun, M. Sy, Y. Wang, A. Ahuja, Y. Zhang, E. Pickwell-macpherson, "A promising diagnostic method: Terahertz pulsed imaging and spectroscopy," *World Journal of Radiology* vol. 3, pp. 55-65, 2011.

[89] B. Williams. "Terahertz quantum-cascade lasers," *Nature Photonics,* vol. 1, pp 517-525, Sept. 2007.

[90] C. Caloz and T. Itoh, *Electromagnetic metamatials: transmission line theory and microwave applications.* Wiley-IEEE Press, 2005.

[91] W. Menzel "A new travelling wave antenna in microstrip," in *Microwave Conference, 8th European,* pp. 302-306, Sept. 1978.

[92] C. Caloz and T. Itoh, "Application of the transmission line theory of left-handed (LH) materials to the realization of a microstrip LH transmission line," *Proc. IEEE-APS USNC/URSI National Radio Science Meeting,* vol. 2, pp. 517-525, Jun. 2002.

[93] C. Caloz and T. Itoh, "Transmission line approach of left-handed (LH) materials and microstrip implementation of an artificial LH transmission line," *IEEE Transactions on Antennas and Propagation,* vol. 52, no. 5, pp. 1159-1166, 2004.

[94] A. Iyer and G. Eleftheriades, "Negative refractive index metamaterials supporting 2-d waves," in *Microwave Symposium Digest, 2002 IEEE MTT-S International,* vol. 2, pp. 1067-1070, 2002.

[95] C. Caloz and T. Itoh, "Application of the transmission line theory of left-handed (LH) materials to the realization of microstrip "LH line", in *Antennas and Propagation Society International Symposium, 2002. IEEE,* vol. 2, pp. 412-415, 2002.

[96] A.A. Oliner, "A periodic-structure negative-refractive-index medium without resonant elements," pp. 41, 2002.

[97] B. S. Williams, P. Hon, A. Tavallaee, T. Itoh, and Q. Chen, "Teraherahertz QC-lasers and active metamaterial antennas," *Proc. SPIE,* vol 8031, 80310K (2011).

[98] P. W. C. Hon, Z. Liu, T. Itoh, and B. S. Williams, "Leaky and bound modes in terahertz metasurfaces made of transmission-line metamaterials," *Journal of Applied Physics,* vol. 113, 033105, Jan. 2013.

[99] H. C. Nathanson, W. E. Newell, R. A. Wickstrom, and J. R. Davis Jr, "The resonant gate transistor," *IEEE Trans. Electron Devices,* vol. 14, pp. 117-133, 1967.

[100] P.M Osterberg, S. Senturia, "MTEST: a test chip for MEMS material property measurement using electrostatically actuated test structures," *J. MEMS,* vol. 6, pp. 107-118, 1997.

[101] K. E. Petersen, "Dynamic michromechanics on Si: techniques and devices," *IEEE Trans. Electron Devices,* vol. 25, pp. 1241-1250, 1978.

[102] S. Pamidighantam, R. Puers, K. Baert, and H. Tilmans, "Pull-in voltage analysis of electrostatically actuated beam structures with fixed-fixed and fixed-free end conditions," *J. Micromechanics and Microengineering.* vol. 12, pp. 458-464, June 2002.

[103] S. Sakai, H. Tanimoto, K. Otsuka, T. Yamada, Y. Koda, E. Kita, and H. Mizubayashi, "Elastic behaviors of high density nanocrystalline gold prepared by gas deposition method," *Scripta Materialia,* vol. 45, no. 11, pp. 1313-1319, 2001.

[104] J. Noel, A. Bogozi, Y. Vlasov, and G. Larkins, "Cryogenic pull-down voltage of microelectromechanical switches," *Journal of Microelectromechanical Systems,* vol. 17, no. 2, pp. 351-355, 2008.

[105] H. Su, I. Llamas-Garra, M. Lancaster, M. Prest, J. Park, J. Kim, C. Back, and Y. Kim, "Performance of RF MEMS switches at low temperature," *Electronics Letters,* vol. 42, no. 21, pp. 1219, 2006.

[106] C. Goldsmith and D. Forehand, "Temperature variation of actuation voltage in capacitive MEMS switches," *IEEE Microwave and Wireless Components Letters,* vol. 15, no. 10, pp. 718-720, 2005.

[107] S. Gong, H. Shen, and N. Barker, "Study of broadband cryogenic DC-contact RF MEMS switches," *IEEE Transactions on Microwave Theory and Techniques,* vol. 57, no. 12, pp. 3442-3449, 2009.

[108] S. Chowdhury, M. Ahmadi, and W. C. Miller, "A closed-form model for the pull-in voltage of electrostatically actuated cantilever beams," *J. Micromechanics and Microengineering* vol. 15, pp. 756-763, Feb. 2005.

[109] X. Yang, Y. Liu, R. Oulton, X. Yin, and X. Zhang, "Optical forces in hybrid plasmonic waveguides," *Nano Letters,* vol 11, pp 321-328, Jan. 2011.

[110] M. L. Povinelli, M. Loncar, M. Ibanescu, E. Smythe, S. Johnson, F. Capasso, J. D. Joannopoulos, "Evanescent-wave bonding between optical waveguides," *Nano Letters,* vol 30, no 22, Nov. 2005.

[111] M. L. Povinelli, S. G. Johnson, M. Loncar, M. Ibanescu, E. Smythe, F. Capasso, J. D. Joannopoulos, "High-Q enhancement of attractive and repulsive optical forces between coupled whispering-gallery-mode resonators," *Optics Express,* vol 13, no 8286, 2005.

[112] A. Leitenstorfer, K. Nelson, K. Reimann, and K. Tanaka, "Focus on nonlinear terahertz studies," *New Journal of Physics,* vol. 16, no. 4, pp. 045016, 2014.

[113] D. Prober, "Superconduction terahertz mixer using a transition-edge microbolometer," *Apllied Physics Letters,* vol. 62, no. 17, pp. 2119, 1993.

[114] H. Hwang, N. Brandt, H. Farhat, A. Hsu, J. Kong, and K. Nelson, "Nonlinear THz conductivity dynamics in p-type CVD-grown graphene," *The Journal of Physical Chemistry. B,* vol. 117, no. 49, pp. 15819-24, 2013.

[115] H. Chen, W. Padilla, J. Zide, A. Gossard, A. Taylor, and R. Averitt, "Active terahertz metamaterial devices," *Nature,* vol. 444, no. 7119, pp. 597-600.

[116] H. Lium M. Wachter, D. Ban, Z. Wasilewski, M. Buchanan, G. Aers, J. Cao, S. Feng, B.S. Williams, and Q. Hu, "Effects of doping concentration on the performance of terahertz quantum-cascade lasers," *Applied Physics Letters,* vol. 87, no. 14, pp. 141102, 2005.

[117] A. Andrews, A. Benz, C. Deutsch, G. Fasching, K. Unterrainer, P. Klang, W. Schrenk, and G. Strasser, "Doping dependence of LO-phonon depletion scheme THz quantum-cascade lasers," *Materials Science and Engineering: B,* vol. 147, pp. 152-155, 2008.